# CMOS READOUT ELECTRONICS FOR MISMATCHED AND MODE-MATCHED MEMS GYROSCOPES

A THESIS SUBMITTED TO
THE GRADUATE SCHOOL OF NATURAL AND APPLIED SCIENCES
OF
MIDDLE EAST TECHNICAL UNIVERSITY

BY

FERHAT YEŞİL

IN PARTIAL FULFILLMENT OF THE REQUIREMENTS
FOR
THE DEGREE OF MASTER OF SCIENCE
IN
ELECTRICAL AND ELECTRONICS ENGINEERING

SEPTEMBER 2015

Approval of the thesis:

# CMOS READOUT ELECTRONICS FOR MISMATCHED AND MODE-MATCHED MEMS GYROSCOPES

submitted by **FERHAT YEŞİL** in partial fulfillment of the requirements for the degree of **Master of Science in Electrical and Electronics Engineering Department**, **Middle East Technical University** by,

Prof. Dr. Gülbin Dural Ünver ____________________
Dean, Graduate School of **Natural and Applied Sciences**

Prof. Dr. Gönül Turhan Sayan ____________________
Head of Department, **Electrical and Electronics Eng.**

Prof. Dr. Tayfun Akın ____________________
Supervisor, **Electrical and Electronics Eng. Dept., METU**

**Examining Committee Members**

Prof. Dr. Haluk Külah ____________________
Electrical and Electronics Eng. Dept., METU

Prof. Dr. Tayfun Akın ____________________
Electrical and Electronics Eng. Dept., METU

Assist. Prof. Dr. Kıvanç Azgın ____________________
Mechanical Eng. Dept., METU

Assist. Prof. Dr. Mehmet Ünlü ____________________
Electrical and Electronics Eng. Dept., YBU

Assist. Prof. Dr. Mahmud Yusuf Tanrıkulu ____________________
Electrical and Electronics Eng. Dept., ADANA STU

**Date:** ______________

**I hereby declare that all information in this document has been obtained and presented in accordance with academic rules and ethical conduct. I also declare that, as required by these rules and conduct, I have fully cited and referenced all referenced material and results that are not original to this work.**

Name, Surname: FERHAT YEŞİL

Signature:

# ABSTRACT

## CMOS READOUT ELECTRONICS FOR MIS-MATCHED AND MODE-MATCHED MEMS GYROSCOPES

Yeşil, Ferhat
M.S., Department of Electrical and Electronics Engineering
Supervisor: Prof. Dr. Tayfun Akın

September 2015, 99 pages

This thesis presents the CMOS readout electronics for both mismatched and mode-matched MEMS gyroscopes. A systematic design of MEMS gyroscope's control loop parameters, which is insensitive to sensor parameters and environmental conditions, is necessary for robust and high performance operation. Extra to the systematic design for high performance operation, some special techniques should be used to further increase the performance of the sensor. In this thesis, as a performance increasing technique, mode-matching method is applied to increase the signal to electronic noise ratio. This is achieved by injecting a perturbation signal to the quadrature cancellation loop, while keeping it decoupled from the angular rate control loop. This injected perturbation signal is used to detect the amount of frequency mismatch that is fed to the mode-match controller in order to tune the sense mode resonance frequency by using spring softening effect. This new controller is implemented in a CMOS ASIC together with the other sensor control loops, and it is verified to maintain matched-mode state under changing environmental conditions. The system reduces the overall output noise of the tested MEMS gyroscope by a factor of 6; truly reaching down to the thermo-mechanical noise floor of 0.23 (°/hr)/√Hz. This performance is obtained with 22mm x 22m packaging and 125mW power consumption.

Keywords: MEMS Gyroscope, Mode-Matching, CMOS Readout Circuit.

# ÖZ

## AYRIK MOD VE BİTİŞİK MOD MEMS DÖNÜÖLÇER İÇİN CMOS OKUMA ELEKTRONİĞİ

Yeşil, Ferhat
Yüksek Lisans, Elektrik ve Elektronik Mühendisliği Bölümü
Tez Yöneticisi: Prof. Dr. Tayfun Akın

Eylül 2015, 99 sayfa

Bu tez, ayrık mod ve bitişik mod MEMS dönüölçerler için CMOS okuma devrelerini sunmaktadır. MEMS dönüölçerlerin kontrol döngü parametrelerinin, sensör parametrelerinden ve çevre koşullarından etkilenmeden, sistematik şekilde tasarlanması, robast ve yüksek performans için gereklidir. Sistematik tasarıma ek olarak, sensörün performansını daha da artırmak için bazı ekstra teknikler kullanılmalıdır. Bu tezde, performans artırma tekniği olarak, sinyalin elektronik gürültüye olan oranını artıran mod birleştirme tekniği uygulanmıştır. Bu teknik açısal hız kontrol döngüsünden ayrık bir şekilde, ofset giderme devresine pertürbasyon sinyali eklenerek elde edilmiştir. Eklenen pertürbasyon sinyali frekans uyumsuzluk miktarını ölçmek için kullanılır. Bu bilgi mod birleştirme kontrolcüsüne verilerek algılama mod rezonans frekansı yay yumuşama etkisi kullanılarak ayarlanır. Bu yeni kontrolcü diğer sensör kontrol döngüleriyle beraber CMOS ASIC olarak gerçekleştirilmiştir, ve birleşik mod durumu değişen çevre koşullarında doğrulanmıştır. Bu sistem test edilmiş MEMS dönüölçerin çıkış gürültüsünü 6 kat düşürmüştür; termo-mekanik gürültü tabanı olan $0.23 (^\circ/hr)/\sqrt{Hz}$ ye ulaşılmıştır. Bu performans, 22mm x 22mm lik paketleme ve 125mW güç tüketimi ile elde edilmiştir.

Anahtar Kelimeler: MEMS dönüölçer, Mod Birleştirme, CMOS Okuma Devresi.

*To My Family*

# ACKNOWLEDGEMENTS

First of all, I would like thank to my thesis advisor Prof. Dr. Tayfun Akın for his guidance and encouragement during my graduate studies. It is a great opportunity for me to work in his inertial MEMS research group.

I also would like to thank to Dr. Said Emre Alper for sharing his technical and practical knowledge and experiences in MEMS gyroscope technology, and more importantly his friendly attitude.

I would like to express my gratitude to M. Mert Torunbalcı, the master of process, and Hasan Doğan Gavcar, the master of the acceleration stopper, for their efforts to fabricate reliable and perfect gyroscopes by highly dominating their profession fields. I also would like to thank Gülşah Demirhan, the master of the automatic laser cutter, for her study to prepare the gyroscopes with professional and good looking labels.

I would like to express my gratitude to Ulaş Aykutlu , Yunus Terzioğlu, Talha Köse, and Onur Yalçın for their helps in the manufacturing of the MEMS gyroscopes and valuable supports for CMOS readout electronics developments. I am very grateful to METU-MEMS center staff for their helps during the gyroscope fabrication, especially Orhan Şevket Akar and Evren Erdil. Special thanks to Selçuk Keskin, Ozan Ertürk, Ramazan Çetin, Başak Kebapçı, Serdar Tez, Osman Aydın, İlker Cömert, and Serkan Yazıcı for their friendship. Moreover, I would like to thank all members of the METU-MEMS Center for providing a nice research and fabrication environment.

I am very grateful to my parents for their endless support, love and encouragement throughout my whole life. I also appreciate my wife, Lamia, for her love.

## TABLE OF CONTENTS

# LIST OF FIGURES

FIGURES

# LIST OF TABLES

TABLES

# CHAPTER 1

# INTRODUCTION

The progress in the sensitivity of micro-electro-mechanical systems (MEMS) enables the use of state-of-art inertial sensors in high-end industrial applications ranging from automotive to military. The requirements of these applications can be satisfied by adding special control loops in MEMS gyroscopes, and improving their signal-to-noise ratio (SNR). The SNR of a MEMS gyroscope is known to be maximized by matching the resonance frequencies of the drive and sense modes [1]. However, fabrication tolerances put a limit to how close these frequencies can be reliably produced, which does not meet matched-mode condition especially for high-Q sensors that require a frequency mismatch less than a fraction of Hz [2]. Post-fabrication and one-time tuning methods [3],[4],[5],[6] cannot meet this requirement due to their inability to track temperature and aging dependent variations. There are attempts to satisfy the continuity of mode-matching by using perturbation-based-extremum-seeking [7] or out-of-band pilot tones [8], but here the perturbation signal is not fully decoupled from the angular rate control loop, therefore, its frequency should be higher than 10 times the angular rate control loop bandwidth, conceding a significant loss in the mechanical gain of the sensor. An alternative automatic mode-matching system is reported by adding an AC signal to the quadrature control loop and tracking the phase relations between this and the drive signal [9]. However, this system has only been demonstrated on a very low-Q (~50) MEMS gyroscope, possibly due to the controller design limits.

This study combines the method in [9] with a disturbance rejection based closed-loop controller [10] that achieves an automatic mode-matching system for a high-Q (~9300) MEMS gyroscope. The proposed system is experimentally verified to reduce the angle random walk (ARW) of the gyroscope by a factor of 6, reaching down to the thermo-mechanical noise limit of $0.23\ (^\circ/\mathrm{hr})/\mathrm{Hz}^{1/2}$. Moreover, the bandwidth of the angular rate control loop is kept higher than 100Hz by using a perturbation signal that is completely decoupled from the angular rate control loop.

In this study, all the other control loops are also implemented including drive mode, sense mode, and quadrature cancellation controllers with preamplifiers in single ASIC-CMOS readout electronics. This readout circuit is implemented with a vacuum packaged MEMS gyroscope in a 22mm x 22mm metal package which can be also operated with both mode-matched and mismatched conditions of vibratory MEMS gyroscopes.

The organization of this chapter is as follows; Section 1.1 presents micromachined vibratory gyroscope and performance specifications. Section 1.2 provides a brief overview of the micro-machined vibratory gyroscopes. Section 1.3 demonstrates MEMS gyroscopes studied in the scope of this thesis. Section 1.4 explains the research objectives and thesis organization.

## 1.1 Micromachined Vibratory Gyroscope and Performance Specifications

The fundamental operation principle of micromachined vibratory gyroscope is based on the Coriolis effect that is an inertial force described by French engineer Gustave-Gaspard Coriolis in 1835. Coriolis realized that an inertial force acting on bodies when the ordinary Newtonian laws of motion are to be used in a rotating frame of reference. Basically, counterclockwise rotation of the reference frame creates this force acting to the right of the direction of body motion as in Figure 1.1 or vice versa. Actually, the object does not deviate from the original path, but it looks like that due to the rotation of the coordinate system. The Coriolis Effect is related with the motion of the object and the motion of the rotating frame. The mathematical expression of this fictitious effect can be written as:

$$F_C = -2 \cdot m \cdot \vec{\Omega} \times \vec{\dot{x}} \qquad 1.1$$

where m denotes the mass of the moving object, $\vec{\dot{x}}$ and $\vec{\Omega}$ are the velocity of the object and the rotation rate of the frame.

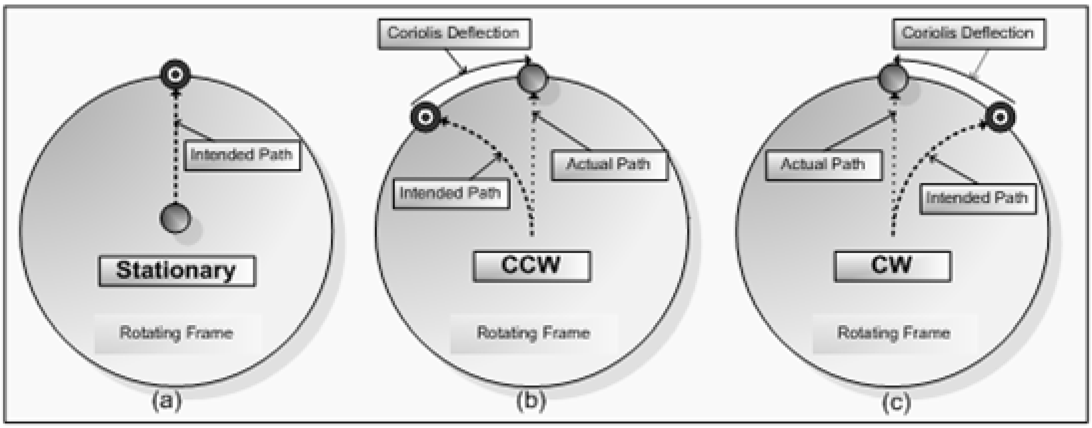

Figure 1.1: Coriolis Effect on the moving object in a rotating coordinate system. (a) Moving mass can follow the intended path when the rotating frame is stationary so there is no Coriolis deflection. (b) However, counter clock wise rotation of the rotating frame leads this force acting to the right of the direction of body motion. (c) The other clock wise rotation of the rotating frame leads this force acting to the left of the direction of body motion.

Figure 1.1 shows the simplest model for describing a single-proof-mass micromachined gyroscope system. The MEMS vibratory gyroscope is basically comprised of a continuously rotating or vibrating element mounted on the gyro frame. Other than that, a sensing element on this frame monitors the orthogonal motion of the rotating or vibrating frame of three suspended frames which are drive frame, sense frame and proof mass. The operation of the gyroscope starts with the sustained vibration along the drive axis of the gyro frame by means of electrostatic, piezoelectric, electromagnetic or electro-thermal actuation mechanism [11]. When the gyro frame is rotated perpendicular to the plane of motion of the rotating or vibrating element, detected by the sense element can detect the orthogonal motion of the rotating or vibrating element as a fictitious acceleration term called Coriolis acceleration proportional to the angular velocity of the gyro frame. This vibration can be detected by using capacitive, optical, piezoresistive, or piezoelectric sensing mechanisms [1].

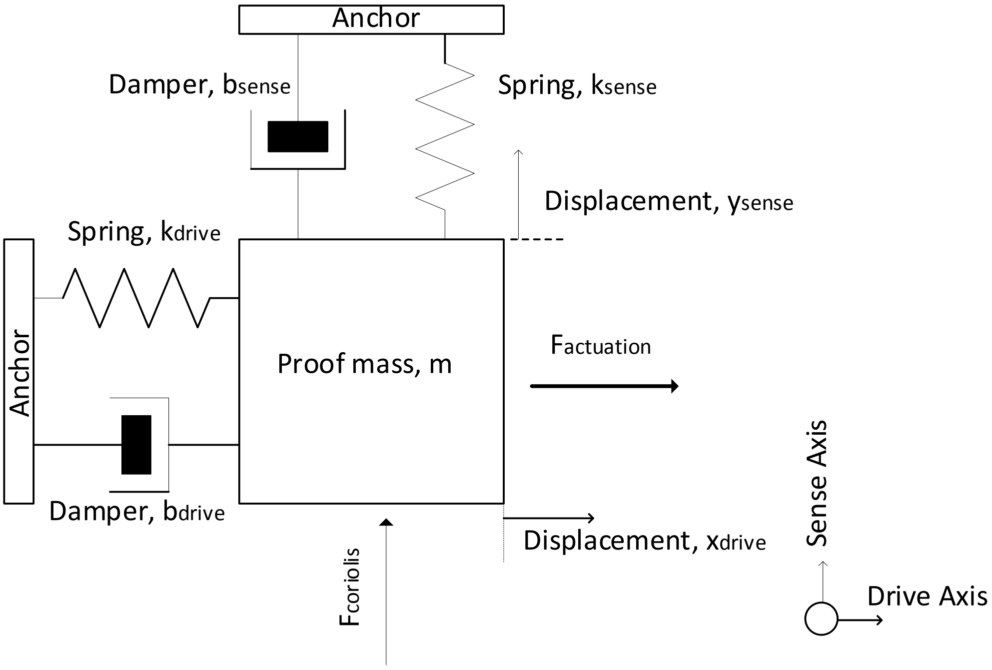

Figure 1.2: The simplest model for describing a single-proof-mass micromachined vibrating gyroscope system.

Different performance specifications are used to identify the micromachined vibratory gyroscopes [12]. Some of the important ones are as follows:

- **Full Scale Range:** Peak to peak measurement range of the sensor per each orthogonal axis. The unit of measure is degrees per second.
- **Zero Rate Bias:** Zero rotation rate output deviation from expected zero rotation rate output value for each sensing axis. The unit of measure is degrees per second.
- **Zero Rate Bias Temperature Coefficient:** Zero rate output deviation from expected zero rate output value due to temperature change from 25C for each sensing axis. The unit of measure is degrees per second per degree Celsius.
- **Sensitivity:** The change in rotation rate input corresponding to 1 LSB change in output. The unit of measure is degree per second per least significant bit.
- **Root Allan Variance Parameters:** Root Allan Variance as computed per IEEE STD 647, 2006. An example of Root Allan Variance Plot can be seen in Figure 1.3.

- **Quantization Noise:** The random variation in the digitized output signal due to sampling and quantizing a continuous signal with a finite word length conversion.
- **Angle Random Walk:** The angular build up with time that is due to the white noise in the angular rate.
- **Bias Instability:** The random variation in bias as computed over specified finite sample time and averaging time intervals.
- **Rate Random Walk:** The drift rate error buildup with time that is due to white noise in angular acceleration.

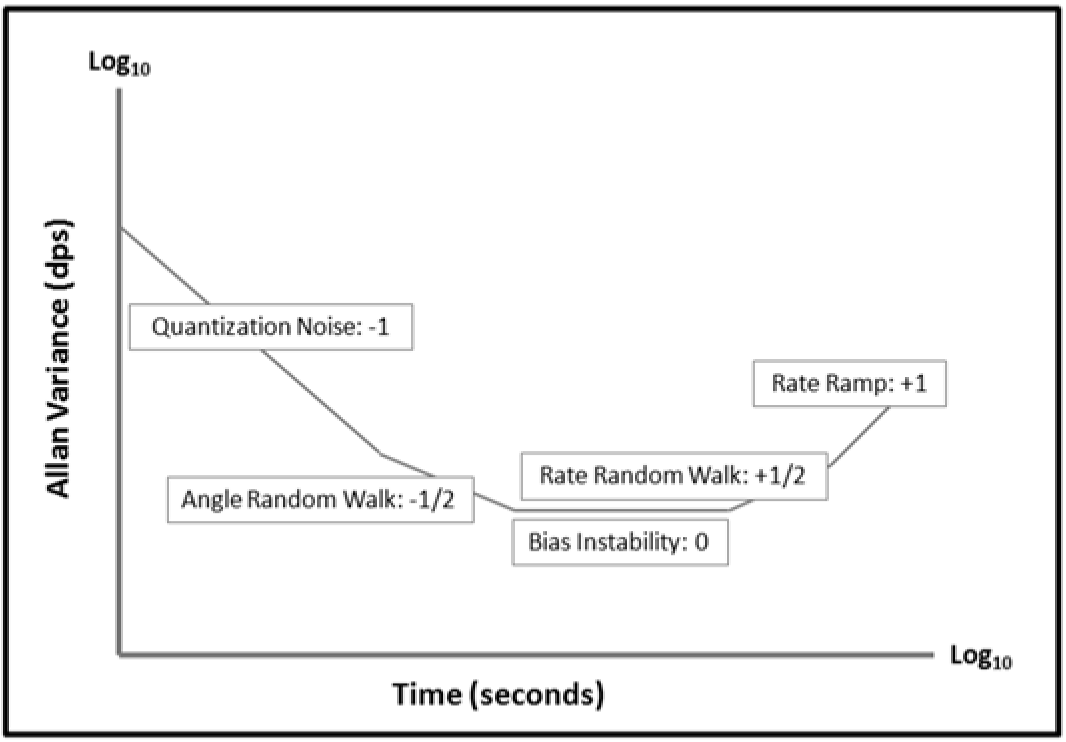

Figure 1.3: An example of Root Allan Variance Plot [12].

- **Noise:** The smallest measureable change in rotation rate expressed as RMS and calculated as the standard deviation of a minimum of 10000 sample points under vibration isolation and zero rotation input. The unit of measure is RMS.
- **Current Consumption:** Measured current consumption. The unit of measure is mili-ampere.

- **Bandwidth:** The frequency response characteristics of the gyroscope under varying angular rate. There are two different methods to identify the bandwidth performance these are -3dB and 90° phase shift points in the frequency response characteristics.
- **Cross-Axis Sensitivity:** Ratio of the measured rotation rate for an axis to the input rotation rate along each axis orthogonal to the measured axis. The unit of measure is percent.
- **Linear Acceleration Sensitivity:** Error in rotation rate measurement due to the existence of linear acceleration along any axis. The unit of measure is degrees per second per g.
- **Integral Non-Linearity:** Maximum deviation of measured output from the best fit straight line. The unit of measure is %FSR.

There are different performance grade gyroscopes regarding these performance grades; rate-grade, tactical-grade, navigation-grade. Performance requirements of these three grades are described in Table 1.1.

Table 1.1: Performance requirements for three types of gyroscopes [13].

| **Parameter** | **Rate Grade** | **Tactical Grade** | **Inertial Grade** |
|---|---|---|---|
| **Angle Random Walk, $^0/\sqrt{hr}$** | >0.5 | 0.5-0.05 | <0.001 |
| **Bias Instability, $^0$/hr** | 10-1000 | 0.1-10 | <0.01 |
| **Scale Factor Linearity, %** | 0.1-1 | 0.01-0.1 | <0.001 |
| **Measurement Range, $^0$/sec** | 50-10000 | >500 | >400 |
| **Bandwidth, Hz** | >70 | ~100 | ~100 |

Micromachined vibratory gyroscopes have contributed greatly today's market due to their small size, light weight, low cost, promising high precision and easy integration. After MEMS technology proved its success in vibratory gyroscopes, micromachined vibratory gyroscopes were widely applied in many fields, including automotive applications for detection rollover and stabilization; consumer electronic applications for video-camera stabilization, smart phones, virtual reality, and inertial mice for computers; robotics applications for high precision and fast machining; a wide range of military applications etc [1].

## 1.2 Overview of the Micromachined Vibratory Gyroscopes

The first micromachined gyroscope study was started with quartz gyroscopes in the early 1980's, but quartz based processes is not suitable for semiconductor fabrication technology. This difficulty was solved by The Charles Stark Draper Laboratory in 1991 by developing a gyroscope can be manufactured by using semiconductor fabrication techniques, having a double gimbals structure with a vertical bar, and a resolution of 4°/sec in 1 Hz measurement bandwidth [14]. In following years, different gyroscope types emerged such as micromachined vibrating gyroscope, piezoelectric vibrating gyroscope, thermal convective gyroscope, magnetic levitated gyroscope, electrostatic levitated gyroscope, MOMES gyroscope, and atom gyroscope [15]. These gyroscope types were manufactured using different kinds of fabrication techniques include bulk micromachining, wafer bonding, surface micromachining, electroplating, Lithographie Galvanoformung Abformung (LIGA) and combined surface-bulk [15].

The mostly studied gyroscope type was micromachined vibrating gyroscope (MVG) over the past years. The main focus area in this category was the tuning fork vibratory gyroscope (TFG) having different detection and excitation electrodes. Georgia Institute of Technology reported a high Q in-plane solid-mass single-crystal silicon TFG having sensitivity of 1.25mV/deg/s in a bandwidth of 12Hz [15]. The recent trend in MEMS is miniaturization of the complete system, combining control of the drive mode, sense mode, quadrature cancellation, and mode matching in a digital processor [16] [17][18].

Significant contributions made at METU to the MEMS gyroscope literature. A fully decoupled tuning fork gyroscope having a superior performance, meeting tactical grade specifications is designed by Alper [19]. A fully decoupled, tuning fork gyroscope with a quadrature cancellation capability is implemented and tested by Tatar[20]. This gyroscope reached to almost navigation level performances. The studied MEMS gyroscope is vacuum packaged by Torunbalci [21][22]. Acceleration sensitivity of tuning fork gyroscope is cancelled by Gavcar [23]. CMOS readouts and the first systematization and modeling studied are made by Eminoglu [24].

## 1.3 Gyroscopes Studied in This Thesis

In this thesis 2 different MEMS gyroscopes are used to implement complete sensor with the CMOS readout circuit. The first one is a double mass fully decoupled MEMS gyroscope [19] having drive, sense, and quadrature cancellation systems. This gyroscope is named as MG1 and it is used only in mismatched condition due to separate sense resonance frequencies in the sense mode. After that, the drawbacks of the separate resonance frequencies of the sense mode, another single mass fully decoupled MEMS gyroscope having drive, sense, quadrature cancellation, and mode-matching systems is designed to be used in both mode-matched and mismatched conditions. This gyroscope is named as MG3, and it is used in both mismatched and mode-matched conditions with the CMOS readout circuit.

## 1.4 Research Objectives and Thesis Organization

The fundamental object of this thesis study is to design the control loops of the tuning fork MEMS gyroscope systematically, to improve the performance by developing a mode-matching technique, and to implement the systematized control loops and developed mode-matching technique in a CMOS ASIC. The definite goals of this research can be listed in the following way:

1. Systematization of the drive mode controller. The controller performance is critical for tactical and navigation grade applications. The drive mode controller should be robust to the environmental conditions and different sensor parameters. Moreover, circuit imperfections should be considered while designing the controller.
2. Sense mode and quadrature cancellation controllers design. The transfer functions of these control loops are needed to be carefully anlyzed and then controllers should be designed by considering performance and bandwidth simultaneously. To create a generalized controller design procedures, controller design parameters should be systematized for mode-matched and mismatched conditions.

3. Mode-match controller design. A mode-matching system should be developed that should be decoupled from rate sensing loop, and it must maintain the mode-matched condition with changing environmental conditions, while MEMS gyroscope is operating. Extra to that, in the literature, mode-matched MEMS gyroscopes generally have low rate bandwidth, this problem should be solved by implementing a closed loop rate sensing and mode matching system these do not limit each other's bandwidth.
4. Performance analysis. The main performance metrics of MEMS gyroscopes of ARW and bias should carefully be analyzed in detail to understand the performance limiting parameters.
5. Implementation and Tests: The systematized control loops and developed mode-matching technique should be implemented in a CMOS ASIC. After that, the fabricated CMOS readout circuit should be implemented with vacuum packaged MEMS gyroscope in a 22mm x 22mm metal package to make the complete system nearly as a product. The manufactured complete system should be tested to verify the operation of the control loops and expected performances.

The organization of the thesis and the contents of the following chapters are as follows:

Chapter 2 mathematical expression of the fictitious Coriolis Force derived in detail. After the derivation, micromachined tuning fork MEMS gyroscope is modeled in detail and then implemented in SPICE environment. Moreover, the developed new mode-matching system is introduced.

Chapter 3 presents the systematized preamplifier and control electronics design for drive mode, sense mode, quadrature cancellation, and mode-matching loops. The detailed design procedures are explained. The simulations of the control loop are conducted in SPICE environment to include circuit imperfections effects on the transient performances of the control loops. The mode-matching technique is also presented in this chapter. Moreover, performance analysis of mismatched and mode-matched MEMS gyroscope is conducted in detail.

Chapter 4 gives the test results of the mode-matched and mismatched tuning fork MEMS gyroscope implemented with the CMOS readout circuit including drive mode, sense mode, quadrature cancellation, and mode-matching control loops with preamplifiers. Then, the experimental data is provided to show the performance increase of the MEMS gyroscope with mode-matched condition compared to mismatched condition.

Finally, Chapter 5 summarizes this thesis study and highlights the achievements of this work. Future research topics are also suggested.

# CHAPTER 2

# VIBRATORY GYROSCOPE THEORY AND MODELLING

The topic of this thesis includes the use of the micromachined vibratory rate gyroscope (MVG). This chapter introduces the theory behind the MVG, and describes the mechanical model of the gyroscopes studied in this thesis in SPICE environment. Section 2.1 explains the mathematical expression of the Coriolis force created on the MVG. Section 2.2 and Section 2.3 give the detailed analysis of the drive and the sense dynamics respectively. Section 2.5 explains the electronegative spring softening effect used to tune the resonance frequency of the sense mode. Section 2.6 provides information about the mode-match mechanism. Finally, Section 2.7 summarizes this chapter.

## 2.1 Mathematical Expression of the Fictitious Coriolis Force

Mathematical derivation of this fictitious force requires use of non-inertial reference frames. A mass having a position vector $x_A(t)$ defined in inertial frame A as in Figure 2.1. A non-inertial frame is defined relative to frame A as $X_{AB}(t)$ and the mass is defined in this frame as $x_B(t)$. The forces on this mass created with respect to frame B will be derived.

The position of the mass in frame B is as follows:

$$\mathrm{x_B} = \sum_{j=1}^{3} x_j \, \mathrm{u}_j \qquad 2.1$$

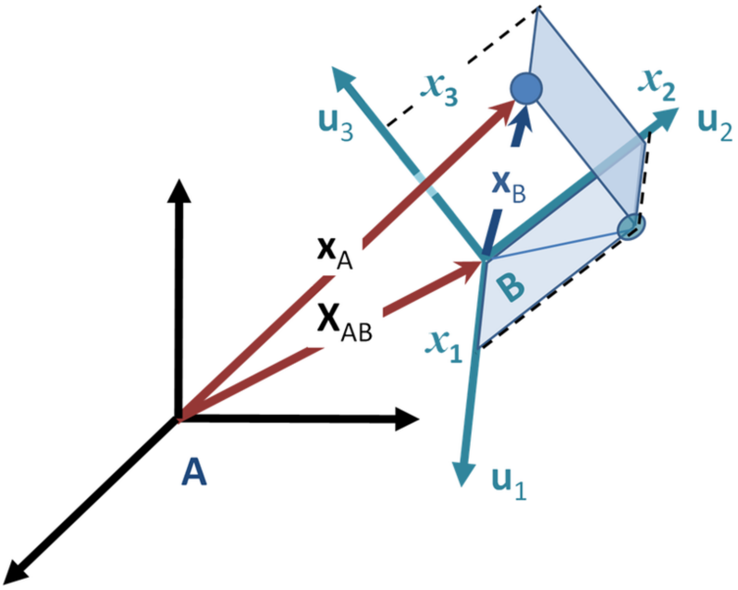

Figure 2.1: An object located at $x_A$ in inertial frame A is located at location $x_B$ in accelerating frame B. The origin of frame B is located at $X_{AB}$ in frame A. The orientation of frame B is determined by the unit vectors along its coordinate directions, $u_j$ with j = 1, 2, 3. Using these axes, the coordinates of the object according to frame B are $x_B$ = ( x1, x2,x3 ) [25].

The position of the mass in frame A is as follows:

$$x_A = X_{AB} + \sum_{j=1}^{3} x_j u_j \tag{2.2}$$

The velocity of the mass can be found by taking derivative of $x_A$ in frame A:

$$\frac{dx_A}{dt} = \frac{dX_{AB}}{dt} + \sum_{j=1}^{3} \frac{dx_j}{dt} u_j + \sum_{j=1}^{3} x_j \frac{du_j}{dt} \tag{2.3}$$

To find the acceleration of the mass can be expressed as the time derivative of Equation 2.3 as follows:

$$\frac{d^2x_A}{dt^2} = a_{AB} + a_B + 2\sum_{j=1}^{3} v_j \frac{du_j}{dt} + \sum_{j=1}^{3} x_j \frac{d^2u_j}{dt^2} \tag{2.4}$$

The first term in Equation 2.4 represents the acceleration of frame B in frame A. The second term is the actual acceleration of the mass in frame B. An observer in frame B sees the mass having extra 3 acceleration terms related to the movement of the frame B coordinate axes. These fictitious acceleration terms occurs because observers in frame B do not recognize the non-inertial nature of frame B. The term $a_{AB}$ created due to the acceleration of the origin of frame B and the other two terms are related to rotation of frame B.

To get the forces on this mass, we should multiply the acceleration terms with mass:

$$\mathrm{F_A} = \mathrm{F_B} + m\mathrm{a_{AB}} + 2m\sum_{j=1}^{3} v_j \frac{d\mathrm{u}_j}{dt} + m\sum_{j=1}^{3} x_j \frac{d^2\mathrm{u}_j}{dt^2} \tag{2.5}$$

Finally, we can express the fictitious force as in Equation 2.6.

$$\mathrm{F_{fictitious}} = -\,m\mathrm{a_{AB}} - 2m\sum_{j=1}^{3} v_j \frac{d\mathrm{u}_j}{dt} - m\sum_{j=1}^{3} x_j \frac{d^2\mathrm{u}_j}{dt^2} \tag{2.6}$$

After that, the problem can be solved in frame B by treating the $\mathrm{F_{fictitious}}$ as an additional force.

Furthermore, when we define the frame B as a rotating coordinate system as in the MVG, we need to obtain the apparent time rate of change of vectors. The rotation of frame B is represented by a vector $\Omega$ with magnitude given by

$$|\Omega| = \frac{d\theta}{dt} = \omega(t) \tag{2.7}$$

The time derivative of any of the three unit vectors describing frame B is

$$\frac{d\mathrm{u}_j(t)}{dt} = \Omega \times \mathrm{u}_j(t) \tag{2.8}$$

and

$$\frac{d^2\mathrm{u}_j}{dt^2} = \frac{d\Omega}{dt} \times \mathrm{u}_j + \Omega \times [\Omega \times \mathrm{u}_j(t)] \tag{2.9}$$

When we remove translational acceleration by setting $a_{AB} = 0$, we can express $a_A$ as follows:

$$a_A = a_B + 2\Omega \times v_B + \frac{d\Omega}{dt} \times x_B + \Omega \times (\Omega \times x_B) \qquad 2.10$$

Finally, we can mathematically express the fictitious force including the Coriolis force, the centrifugal force, and the Euler force respectively as follows:

$$F_{fictitious} = -2m\Omega \times v_B - m\Omega \times (\Omega \times x_B) - m\frac{d\Omega}{dt} \times x_B \qquad 2.11$$

At this point, the Coriolis force should be separated from the other terms. The effect of centrifugal force can be cancelled with some mechanisms, and the Euler force is assumed zero due to not having time-varying rate of rotation. As a conclusion, we obtained the most important principle of the MVG to detect the rate of rotation in a non-inertial frame.

## 2.2 Drive Mode Dynamics

The proof mass should be driven into a sustained oscillation along the drive axis for the generation of the velocity term of the Coriolis force $v_B$ as in Equation 2.11. This velocity term highly important for stable scale factor and zero rate output due to gain mismatches. A stable $v_B$ can be obtained by modeling the drive mode dynamics well. Firstly, spring-mass-damper system is modeled in Figure 2.2 and derived from Equation 2.12 to Equation 2.14.

The force applied on the mechanical system is defined by the system parameters and displacement as follows:

$$F(s) = (m.s^2 + b.s + k).X \qquad 2.12$$

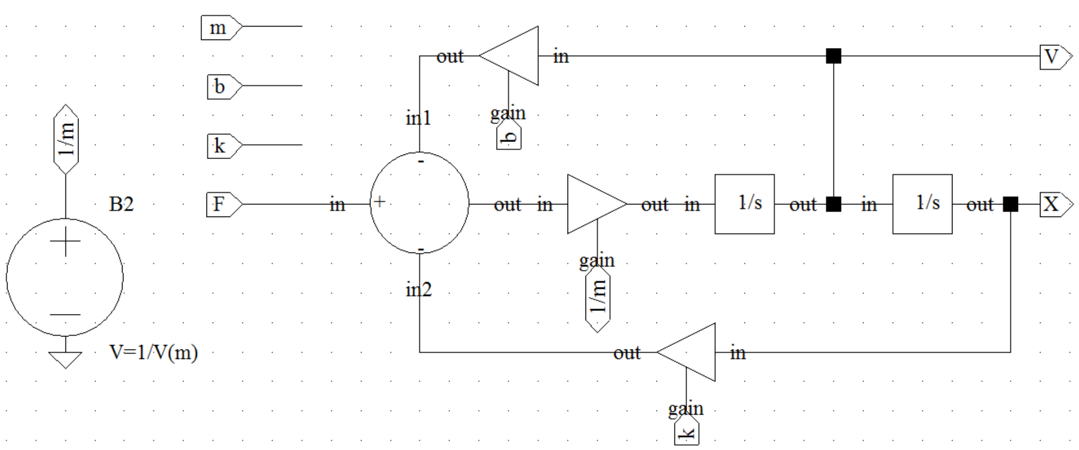

Figure 2.2: The SPICE implementation of the spring-mass-damper system

According to the above formula displacement and velocity can be expressed as in Equation 2.13 and Equation 2.14.

$$\frac{X(s).s}{F(s)} = \frac{s}{m.s^2 + b.s + k} \tag{2.13}$$

$$\frac{V(s)}{F(s)} = \frac{s}{m.s^2 + b.s + k} \tag{2.14}$$

To model the all the mechanical transfer function of the drive mode, voltage to force and velocity to current conversion mechanisms should be expressed and derived.

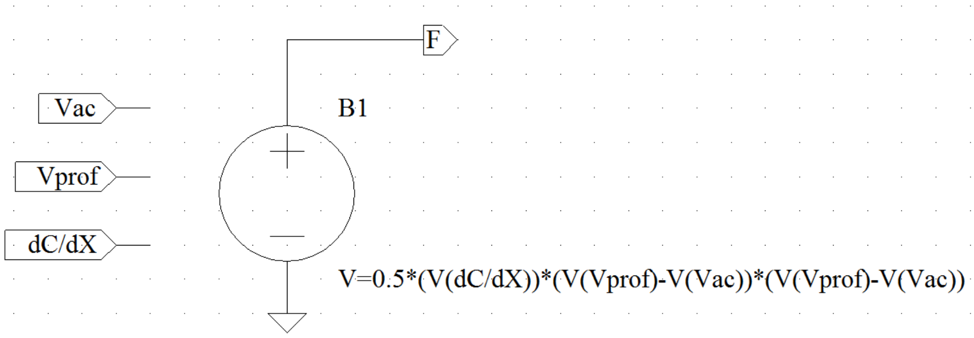

Figure 2.3: The voltage to force conversion implemented in SPICE environment.

The voltage to force conversion is realized by using varying overlap capacitors. The mathematical derivation of this system is derived from Equation 2.15 to Equation 2.17, and implemented in SPICE environment as in Figure 2.3.

The derivation of this system starts with the energy equation of a capacitor as in Equation 2.15, and continues with the derivation of it to obtain the generated force by the applied potential as in Equation 2.16. However, this force is not linear with the applied potential. To overcome this problem the applied potential has extra predefined DC proof-mass potential. This potential provides linear force at the applied AC potential frequency as in Equation 2.17 proportional with $\mathrm{Vprof.Vac}$.

$$\mathrm{E} = \frac{1}{2}\mathrm{C}.\mathrm{V}^2 \tag{2.15}$$

$$\frac{\partial \mathrm{E}}{\partial \mathrm{x}} = \mathrm{F} = \frac{1}{2}.\frac{\partial \mathrm{C}}{\partial \mathrm{x}}.\mathrm{V}^2 \tag{2.16}$$

$$\mathrm{F} = \frac{1}{2}\frac{\partial \mathrm{C}}{\partial \mathrm{x}}(\mathrm{Vprof} - \mathrm{Vac})^2 = \frac{1}{2}\frac{\partial \mathrm{C}}{\partial \mathrm{x}}((\mathrm{Vprof})^2 + (\mathrm{Vac})^2 - 2\ \mathrm{Vprof\ Vac}) \tag{2.17}$$

Another part of the drive mechanism is velocity to current conversion. The velocity of the mass is converted to current by using varying overlap capacitors. The derivation of this conversion starts with Equation 2.18. The time derivative of this equation with respect to changing capacitance is expressed as in Equation 2.19. However, in a gyroscope $\frac{\partial C}{\partial x}$ is mainly used parameter, because of that, $\frac{\partial C}{\partial t}$ is defined by $\frac{\partial C}{\partial x}.\frac{\partial x}{\partial t}$ as in Equation 2.20.

$$Q = CV \tag{2.18}$$

$$I = \frac{\partial C}{\partial t}.V \tag{2.19}$$

$$I = \frac{\partial C}{\partial x}.\frac{\partial x}{\partial t}.V \tag{2.20}$$

Finally, whole transfer function of the drive mechanism can be written as in Equation 2.21 the combinations of Equation 2.14, Equation 2.17, and Equation 2.20.

$$\frac{I(s)}{Vac(s)} = -(\frac{\partial C}{\partial x}Vprof)^2 \frac{s}{m.s^2 + b.s + k} \qquad 2.21$$

The other generally used parameters for these systems are resonance frequency and quality factor labeled as ω and Q respectively. These parameters can be expressed as mechanical system parameters as in Equation 2.22 and Equation 2.23.

$$\omega_D = \sqrt{\frac{k}{m}} \qquad 2.22$$

$$Q_D = \frac{\sqrt{k.m}}{b} \qquad 2.23$$

The transfer function of the voltage to current can be modified by using above equations to construct a more clear transfer function as in Equation 2.24.

$$\frac{I(s)}{Vac(s)} = -(\frac{\partial C}{\partial x}Vprof)^2 \frac{s}{m.(s^2 + \frac{\omega_D}{Q_D}.s + \omega_D{}^2)} \qquad 2.24$$

$\frac{I(s)}{Vac(s)}$ transfer function can be expressed as in Equation 2.25 with $\omega_D$, $Q_D$, and mechanical parameters, when the operating frequency is chosen as $\omega_D$.

$$\frac{I(j\omega_D)}{Vac(j\omega_D)} = -(\frac{\partial C}{\partial x}Vprof)^2 \frac{Q_D}{m.\omega_D} \qquad 2.25$$

The final equation states that $\frac{I}{Vac}$ is directly proportional with $Q_D$ at mechanical resonance frequency. This also implies that displacement of the system is at the highest level when the applied potential providing lowest possible excitation potential for a defined displacement amount. Moreover, the lowest excitation potential couple to other systems electrically and mechanically at the lowest level.

## 2.3 Sense Mode Dynamics

Sense mode dynamics are highly similar with drive mode dynamics. However, the actuation and sense electrodes are different than the drive electrodes. Instead, varying gap capacitive electrodes are used for actuation and sense. When constructing the sense mode dynamics based on the fictitious force, the only element subject to the fictitious force is the proof mass due to fully decoupled gyroscope architecture. So, the sense mode dynamics can be expressed as

$$\begin{aligned} \mathrm{F_{fictitious}} &= -2m_{PM}\Omega_\mathrm{z} \times \mathrm{v_D} - m_\mathrm{PM}\Omega_\mathrm{z} \times (\Omega_\mathrm{z} \times \mathrm{x_D}) - m_{PM}\frac{d\Omega_\mathrm{z}}{d\mathrm{t}} \times \mathrm{x_D} \\ &= m_S\ddot{y}(t) + b_S\dot{y}(t) + k_S y(t) \end{aligned} \qquad 2.26$$

In Equation 2.26, $m_{PM}$ and $m_S$ denote the proof mass and the total sense mass including the proof mass and the mass of the sense electrodes respectively.

The $\mathrm{F_{fictitious}}$ can be assumed as the sum of Coriolis force and the Euler force because, the effect of centrifugal force can be cancelled with some mechanisms. The Equation 2.26 can be written as in Equation 2.27 with these modifications.

$$-2m_{PM}\Omega_\mathrm{z} \times \mathrm{v_D} - m_{PM}\frac{d\Omega_\mathrm{z}}{d\mathrm{t}} \times \mathrm{x_D} = m_S\ddot{y}(t) + b_S\dot{y}(t) + k_S y(t) \qquad 2.27$$

Let assume a time-varying angular rate input and a time-varying displacement of drive mode in the following form:

$$\mathrm{x_D(t) = X_D\cos(w_D t)} \qquad 2.28$$

$$\Omega_\mathrm{z}(\mathrm{t}) = \Omega_\mathrm{z}\cos(\mathrm{w_z t}) \qquad 2.29$$

When we plug Equation 2.28 and Equation 2.29 into Equation 2.27, the fictitious based sense dynamics becomes as in Equation 2.30.

$$m_{PM}\Omega_z X_D\left\{\left(w_D+\frac{w_z}{2}\right)\sin(w_D+w_z)t+\left(w_D-\frac{w_z}{2}\right)\sin(w_D-w_z)t\right\}$$ 2.30

$$= m_S\ddot{y}(t)+b_S\dot{y}(t)+k_S y(t)$$

Equation 2.30 shows that the Coriolis force acting along the sense mode of the gyroscope has two components equally separated from the drive-mode resonance frequency, $w_D$, in the frequency domain. The amplitudes of these components can be written as

$$Y(w_D+w_z)=\frac{\frac{m_{PM}}{m_S}X_D\Omega_z\left(w_D+\frac{w_z}{2}\right)}{(w_S^2-(w_D+w_z)^2)+j\frac{w_S}{Q_S}(w_D+w_z)}$$ 2.31

$$Y(w_D-w_z)=\frac{\frac{m_{PM}}{m_S}X_D\Omega_z\left(w_D-\frac{w_z}{2}\right)}{(w_S^2-(w_D-w_z)^2)+j\frac{w_S}{Q_S}(w_D-w_z)}$$ 2.32

The sense mode of the gyroscope has two different operations, regarding the separation between the mechanical resonance frequencies of the drive mode and sense mode. If we assume that the frequency of the rate input is at zero, the amplitude of the displacement at sense mode can be expressed as:

$$Y(w_D-w_z)+Y(w_D+w_z)=\frac{X_D\Omega_z}{(\Delta w)+j\frac{w_S}{Q_S}}\frac{m_{PM}}{m_S}$$ 2.33

The other operation of the gyroscope is that the mechanical resonance frequencies of the drive mode and sense mode are very close each other, named as mode-matched operation. When we assume that the frequency of the rate input is zero, the amplitude of the displacement at sense mode can be expressed as

$$Y(w_D-w_z)+Y(w_D+w_z)=\frac{X_D\Omega_z}{j\frac{w_S}{Q_S}}\frac{m_{PM}}{m_S}$$ 2.34

Matching the resonance frequencies of the drive and sense modes of the gyroscope amplifies the sense mode deflection by the mechanical quality factor of the sense mode when compared Equation 2.33 with Equation 2.34. This is the idea behind maximizing the sensitivity of a vibratory gyroscope to improve the performance of the gyroscopes with electronic noise limited case, since the mechanical quality factors can be as high as few thousands at vacuum for micro-machined resonators.

There should be a quantitative definition for the matched and mismatched operations of a micromachined gyroscope. The matched operation can be defined as a condition of the gyroscope having the separation between the drive and the sense mode resonance frequencies being smaller than 1/10 of the response bandwidth. Similarly, the mode frequencies can be considered as mismatched for the separation between them being 10 times larger than the response bandwidth. For these operations, Equation 2.34 and Equation 2.33 can be used respectively.

Moreover, whole sense mode mechanical transfer function of the voltage to current conversion should be defined by adding voltage to force and velocity to current conversion.

Firstly, $\frac{\partial \mathrm{C}}{\partial \mathrm{y}}$ should be calculated by assigning the directions for true sign calculation as in Figure 2.4. The derivation of $\frac{\partial \mathrm{C}}{\partial \mathrm{y}}$ starts with the definition of $Cp$ and $Cn$ as in Equation 2.35and Equation 2.36 according to geometry and some constants, then the derivation of them gives the results as in Equation 2.37 and Equation 2.38.

$$\mathrm{Cp} = \frac{\mathcal{E}.\mathrm{h}.\mathrm{l}}{(\mathrm{g}+\mathrm{Y})} \qquad 2.35$$

$$\mathrm{Cn} = \frac{\mathcal{E}.\mathrm{h}.\mathrm{l}}{(\mathrm{g}-\mathrm{Y})} \qquad 2.36$$

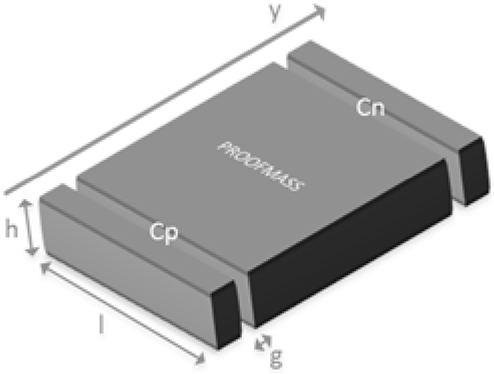

Figure 2.4 Varying gap capacitors of the sense frame.

$$dCp_{dY} = -\frac{\mathcal{E}.h.l}{(g+Y)^2} \quad 2.37$$

$$dCn_{dY} = \frac{\mathcal{E}.h.l}{(g-Y)^2} \quad 2.38$$

The force generated at positive and negative force feedback electrodes can be expressed as in Equation 2.39 and Equation 2.40 respectively with defined force directions shown at Figure 2.5.

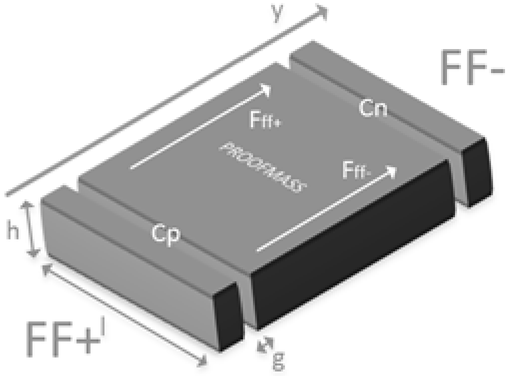

Figure 2.5: Generated forces on the sense frame.

$$\mathrm{FF}+=\frac{1}{2}.\frac{\partial \mathrm{Cp}}{\partial \mathrm{Y}}.(\mathrm{Vprof}-\mathrm{Vff}+)^2$$

$$=\frac{1}{2}.\frac{\partial \mathrm{Cp}}{\partial \mathrm{Y}}.\left((\mathrm{Vprof}^2+\mathrm{Vff}+^2)-2.\mathrm{Vprof.Vff}+\right) \qquad 2.39$$

$$FF-=\frac{1}{2}.\frac{\partial Cn}{\partial Y}.(Vprof-\mathrm{Vff}-)^2$$

$$=\frac{1}{2}.\frac{\partial Cn}{\partial Y}.((Vprof^2+\mathrm{Vff}-^2)-2.Vprof.\mathrm{Vff}-) \qquad 2.40$$

The current generated at positive and negative sense pick electrodes can be expressed as in Equation 2.41 and Equation 2.42 respectively with defined current directions shown at Figure 2.6. The generated current at these nodes are at the resonance frequency of the drive mode due to Coriolis coupling.

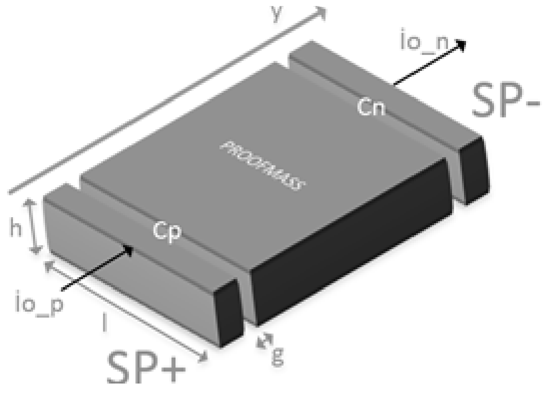

Figure 2.6: Generated currents on the sense frame.

$$io_p=-\frac{\partial Cp}{\partial Y}.V_y.(Vprof-SPp) \qquad 2.41$$

$$io\_n=\frac{\partial Cn}{\partial Y}.V_y.(Vprof-SPn) \qquad 2.42$$

## 2.4 Electronegative Spring Softening

This section will focus on a concept of electronegative spring softening. In a micromachined gyroscope, there are two important spring constants involved. One of them characterizes the drive mode mechanical resonance frequency, and the other one characterizes the sense mode mechanical resonance frequency. When these springs are manufactured with a standard micromachining technology, the advantages of perfect matching cannot be obtained due to tolerances. However, the mode-matching can be realized by using electrostatic negative spring constant occurred at varying gap capacitive electrodes at sense peak electrodes. Firstly we will look at the force generated at sense pick electrodes and then we will analyze electronegative spring effect. There are two forces effective on the gyroscope frame. The main force is the mechanical force generated by mechanical springs, and the other force is the electrostatic forces. These forces can be expressed as in Equation 2.43 and Equation 2.44 respectively.

$$F_{mech} = -k_{mech}.(y - y_0) \qquad 2.43$$

$$F_{elec} = -\frac{1}{2}.\frac{A.\mathcal{E}}{y^2}.V^2 \qquad 2.44$$

The force equations can be linearized at the steady position, because the mechanical frame does not move its own steady position due to force feedback. The linearization can be made as in Equation 2.45 and Equation 2.46.

$$F_{mech} = \frac{dF_{mech}}{dy}.y = -k_{mech}.y \qquad 2.45$$

$$F_{elec} = \frac{dF_{elec}}{dy}.y = \frac{1}{2}.\frac{A.\mathcal{E}}{{y_0}^3}.y.V^2 \qquad 2.46$$

The combination of these two forces can be expressed as in Equation 2.41. The $k_{eff}$ in the Equation 2.41 can be altered according to applied external voltages according to Equation 2.42.

$$F_{mech} + F_{elec} = -k_{mech}.y + \frac{1}{2}.\frac{A.\mathcal{E}}{{y_0}^3}.y.V^2 = -k_{eff}.y \qquad 2.47$$

$$k_{eff} = -k_{mech} + \frac{1}{2}.\frac{A.\mathcal{E}}{{y_0}^3}.V^2 \qquad 2.48$$

The spring softening effect can only be used to decrease the effective resonance frequency of the mechanical system by varying the applied DC potential on the varying gap electrodes as in Equation 2.49. Moreover, there are some other method that can be used to harden the effective spring constant by using the 90° phase shifted version of the output signal of the electrodes in the feedback loop to create extra force as a positive spring effect.

$$\omega_s = \sqrt{\frac{k_{eff}}{m}} = \sqrt{\frac{k_{mech} - \frac{1}{2}.\frac{A.\mathcal{E}}{{y_0}^3}.V^2}{m}} \qquad 2.49$$

## 2.5 Quadrature Error and Cancellation Electrodes

Quadrature error is produced by the coupling of the drive displacement onto the sense frame. This coupling occurs due to poor fabrication tolerances, but the good thing about this error source is that quadrature error signal is the 90° phase shifted version of the Coriolis signal. The main cancellation method of this error is phase sensitive demodulation, but phase errors and the chance in the phase error due to environmental conditions lead lower performance MEMS gyroscope. Extra to modulation technique, some other methods were also developed. The most effective method is the electrostatic quadrature suppression technique. The implementation structure of this suppression technique with some electrodes can be seen at Figure 2.7.

The proof mass in Figure 2.7 moves in the x direction for an amount of X. This movement creates a force on the proof mass in y direction can be expressed as in Equation 2.50.

$$F_y = \frac{1}{2}.\frac{dC}{dy}.V^2 \qquad 2.50$$

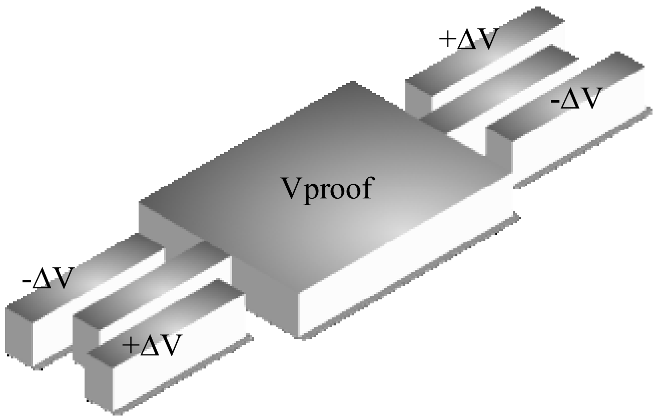

Figure 2.7: Electrostatic quadrature suppression electrode structure.

The four capacitors in the Figure 2.7 create a force in phase with the quadrature error to be used as a cancellation force.

$$\begin{aligned} F_y &= F_{quad\_cancel} \\ &= \frac{1}{2}.\frac{\varepsilon.(L-X).h}{(y_0-y)^2}.(V_{DC}+\Delta\mathrm{V})^2 \\ &-\frac{1}{2}.\frac{\varepsilon.(L-X).h}{(y_0+y)^2}.(V_{DC}-\Delta\mathrm{V})^2 \\ &+\frac{1}{2}.\frac{\varepsilon.(L+X).h}{(y_0-y)^2}.(V_{DC}-\Delta\mathrm{V})^2 \\ &-\frac{1}{2}.\frac{\varepsilon.(L+X).h}{(y_0+y)^2}.(V_{DC}+\Delta\mathrm{V})^2 \end{aligned} \qquad 2.51$$

The above quadrature cancellation force equation can be modified for small displacement in y direction as in Equation 2.52.

$$F_y = F_{quad\_cancel} = -\frac{4.\mathcal{E}.V_{DC}.\Delta\mathrm{V}.X.h}{{y_0}^2} \qquad 2.52$$

The Equation 2.52 is an AC force due to sinusoidal displacement of X. As a conclusion, this AC force generated by applying only DC voltage.

## 2.6 Mode-Match Mechanism

The progress in micro-electro-mechanical systems (MEMS) vibratory rate gyroscopes found a place in tactical-grade applications, where low weight and small size are essential. However, the performance of the MEMS gyroscopes nearly reached the performance requirements of the navigation grade applications. These requirements generally be satisfied by adding special control loops in MEMS gyroscopes providing increase in the signal-to-noise ratio (SNR) of a MEMS gyroscope. SNR of a MEMS gyroscope is known to be maximized by matching the resonance frequencies of the drive and sense modes. Gyroscope system has electronic noise extra to mechanical Brownian noise. Generally, high performance, high Q-factor gyroscope systems are limited by higher electronic noise compared to mechanical noise. The mentioned mode-matching of the drive and sense modes increases the mechanical output signal and provides increase in the signal to electronic noise ratio, so the performance of the electronic noise limited gyroscope system is improved to satisfy the navigation grade requirements.

In a micromachined vibratory gyroscope system, rate information is obtained by the coupling of the drive motion to the sense mass by the Coriolis effect. The coupled force is in phase with the drive motion, but the transfer of this force to sense pick signal is dependent on the resonance frequencies of the drive and sense modes. When the resonance frequency of the sense mode is higher than the resonance frequency of the drive mode, sense pick signal is the 90° phase shifted version of the drive pick signal. At this condition, rate information can be obtained by modulating the sense pick with phase shifted version of the drive pick signal. However, the modulation procedure is different for the mode-matched condition due to change in the transfer function of the mechanical gyroscope system. At mode matched case, the sense pick signal is modulated by the drive pick signal to get the rate information. The noise in this rate is lower than the mentioned mismatched condition due to increase in the signal to noise ratio thank to mode-matching.

However, the realization of the mode-matching is not an easy, because fabrication tolerances put a limit to how close these frequencies can be reliably produced, which does not meet matched-mode condition especially for high-Q sensors that require a frequency mismatch less than a fraction of a Hz [2]. Post-fabrication and one-time tuning methods [3],[4],[5],[6], cannot meet this requirement due to their inability to track temperature and aging dependent variations. There are attempts to satisfy the continuity of mode-matching by using perturbation-based-extremum-seeking [7] or out-of-band pilot tones [8], but here the perturbation signal is not fully decoupled from the angular rate control loop, therefore, its frequency should be higher than 10 times the angular rate control loop bandwidth, conceding a significant loss in the mechanical gain of the sensor in the mode-matching control loop. An alternative automatic mode-matching system is reported by adding an AC signal to the quadrature control loop and tracking the phase relations between this and the drive signal [9]. However, this system has only been demonstrated on a very low-Q (~50) MEMS gyroscope due to the controller design limits.

In this study, we combined method in [9] with a disturbance rejection based closed-loop controller [10] that achieves an automatic mode-matching system for a high-Q (~9300) MEMS gyroscope. This system is reported in [26]. The proposed system is experimentally verified to reduce the angle random walk (ARW) of the gyroscope by a factor of 6, reaching down to the thermo-mechanical noise limit of $0.23\ (^\circ/\mathrm{hr})/\mathrm{Hz}^{1/2}$. Moreover, the bandwidth of the angular rate control loop is kept higher than 100Hz by using a perturbation signal that is completely decoupled from the angular rate control loop.

## 2.7 Summary

This chapter presented detailed analysis of the fictitious Coriolis Force and the modeling of the MEMS gyroscope studied in this thesis. Moreover, the capacitive actuation and sensing mechanism for the MEMS gyroscope are explained. The electrostatic spring effect, the main motivation of the mode-matching, on the sense resonance frequency is explained in detail. Then, the quadrature cancellation mechanism is examined. Finally, the mode-match system and its advantage is introduced, and then the literature and the developed mode-matching system are presented.

# CHAPTER 3

# CONTROL ELECTRONICS FOR MEMS GYROSCOPES

This chapter presents the details of control electronics and controller design for mode-matched and mismatched micromachined vibratory gyroscopes studied in this thesis. Section 3.1 explains the front-end electronics used to convert the output currents of the gyroscope to the voltage. Section 3.2 explains the closed loop drive loop system and controller design method that does not require Q-factor information. Section 3.3 introduces the closed loop rate sensing mechanism. Section 3.4 provides the design of the closed loop quadrature cancellation controller electronics. Section 3.5 presents the acceleration sensing circuit and closed loop acceleration compensation electronics implemented in this thesis. Section 3.6 gives a brief summary of the chapter.

## 3.1 Front-End Electronics

The front-end electronics generally used to convert tiny electrical signal to a signal level to process them later with signal processing electronics. In gyroscope system, the information is supplied with tiny current signals and converted to a desired voltage level by a preamplifier. In the front-end, transimpedance amplifier (TIA) is used as a preamplifier due to insensitivity to parasitic capacitances and contact resistances. TIA is also provides very low input impedance inherently, and prevents any current loss to be process in the next processing electronics. The schematic of this preamplifier is shown at Figure 3.1.

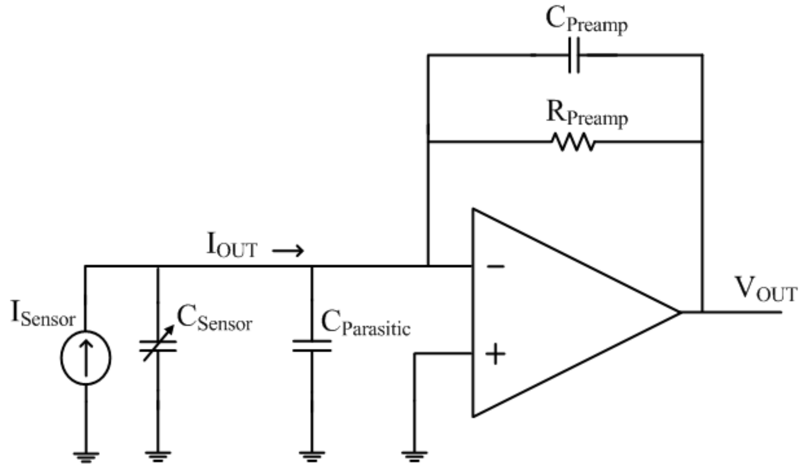

Figure 3.1: Schematic of the transimpedance amplifier implemented with an op-amp.

The transfer function of the transimpedance amplifier can be expressed as follows:

$$\left|\frac{V_o(s)}{I_o(s)}\right| = Z_{pre} = \frac{R_{pre}}{1 + sC_{pre}R_{pre}} \qquad 3.1$$

The TIA is named as resistive or capacitive according to value of $sC_{pre}R_{pre}$. When the $sC_{pre}R_{pre}$ is much greater than 1 at the operating frequency, the type of the preamplifier becomes capacitive preventing extra resistive noises. Because of that capacitive type TIA is generally used as sense preamplifier, but this type of preamplifier is not suitable for drive loop due to higher gain at DC. The higher gain at lower frequencies creates additive environmental noise for the rate signal, because the drive pick signal is used as modulating signal for sense pick signal, and out of the operation frequency($\omega_d$) signals in the drive pick signal fold into the rate signal. However, resistive TIA circuit requires careful trade-offs among noise gain, bandwidth, and stability [27]. Clearly stability in a TIA is essential for good, reliable performance. The undesired oscillations of the resistive type preamplifiers can be understood by plotting the open-loop gain and the feedback factor as in Figure 3.2.

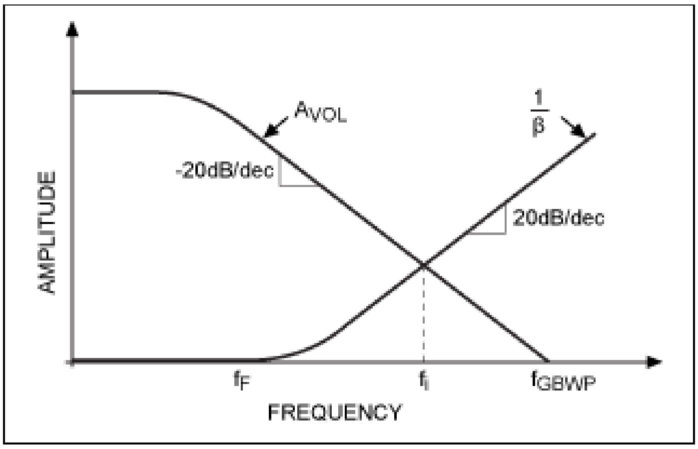

Figure 3.2: Open-loop gain, AVOL(jω), and the reciprocal of feedback factor, 1/β(jω), versus frequency. The rate of closure between the two curves determines the likelihood of oscillations/ringing [27].

Using the simplified equivalent circuit for the sensor, the feedback network is simply a one-pole RC filter comprised of the feedback resistance, $R_{preamp}$, and the total input capacitance, $C_{paracitic} + C_{sensor}$ . The feedback factor is given as:

$$\beta(s) = \frac{1}{1 + s.\mathrm{R_{preamp}}.(\mathrm{C_{paracitic}} + \mathrm{C_{sensor}})} \qquad 3.2$$

Barkhausen stability criterion state that oscillation can result, if the open-loop transfer function of resistive TIA circuit does not have sufficient phase margin for the intersection of the $A_{VOL}$(jω) response curve with the 1/β(jω) curve denotes a critical intercept fundamental for stability analysis.

The stability of the resistive preamplifier is generally accomplished by adding a bypass capacitor parallel with the $R_{preamp}$. The value of this compensation capacitor is important for optimal trade of between bandwidth and stability. The feedback factor changes by adding the capacitor as follows:

$$\beta(s) = \frac{1 + s.\mathrm{R_{preamp}}.\mathrm{C_{preamp}}}{1 + s.\mathrm{R_{preamp}}.(\mathrm{C_{paracitic}} + \mathrm{C_{sensor}} + \mathrm{C_{preamp}})} \qquad 3.3$$

The compensation capacitor $\mathrm{C_{preamp}}$ creates a zero in the feedback factor. The zero compensates for the phase shift introduced by the feedback network as in Figure 3.3. The goal of the compensation is to find the minimum value of the feedback compensation capacitor, $C_{preamp}$, needed to eliminate oscillation and minimize ringing. However, it is always a good idea to overcompensate the TIA circuit slightly. Over compensation is recommended to provide sufficient guardband to account for up to ±40% variation in an op amp's bandwidth over process corners and the tolerance of the passive components[27].

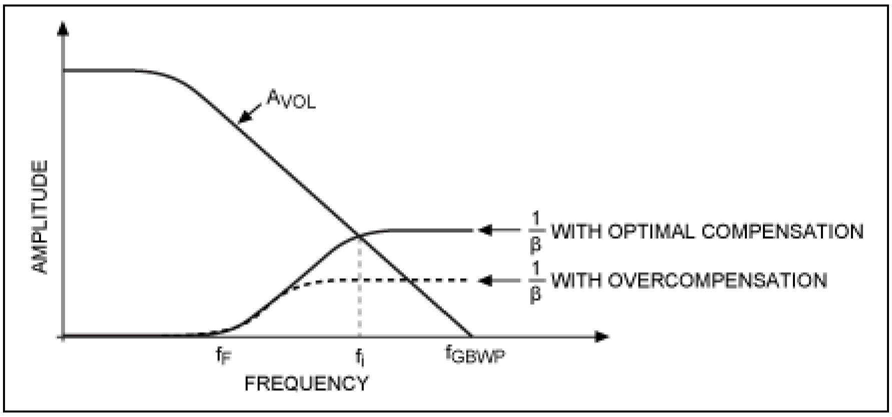

Figure 3.3: Phase response with the phase-compensation capacitor, $C_{preamp}$ [27].

A good design of resistive TIA requires 45° phase margin at the intercept of the $A_{VOL}(j\omega)$ and $1/\beta(j\omega)$ curves. Moreover, $f_{GBWP}$ of the opamp should be selected %60 of the value specified on the op amp's datasheet. Finally, the $C_{preamp}$ can be calculated by using Equation 3.4, while paying attention to mentioned rules.

$$C_{preamp} = \frac{1}{4.\pi.R_{preamp}.f_{GBWP}}.\left\{1+\sqrt{1+8.\pi.R_{preamp}.\left(C_{paracitic}+C_{sensor}\right).f_{GBWP}}\right\} \qquad 3.4$$

## 3.2 Drive Mode Control Electronics and Controller Design for MEMS Gyroscope

The rate data of the micromachined vibratory gyroscope is highly related with the displacement of the drive mass, because the effect of Coriolis force is created by this displacement. For high performance operation, the stabilities of the parameters become highly important especially the drive displacement. The important performance metrics like scale factor stability; noise and bias are affected by any change in the displacement. Because of that some methods were developed to sustain the stability of the drive displacement.

In this study, amplitude controlled positive feedback analog controller mechanism is used. The drive mass easily enters the self oscillation due to more than 10,000 Q-factor of the drive mode and ensuring the Barkhausen Stability Criterion. After that, The self oscillation amplitude is stabilized at the desired level with the closed loop controller.

The operation of the drive control mechanism starts with preamplifier stage as in Figure 3.4. Afterwards, the picked signal is rectified and low pass filtered to provide present amplitude of the oscillation to the controller, then this signal is compared with the desired set point voltage and the control signal is created by the controller. After that, the DC control signal is up converted to the resonance frequency of the drive mode and supplied to the drive motor electrodes as a square wave. This square wave is band pass filtered by the resonance characteristics of the drive mode and completed the loop by transferring the filtered signal to the preamplifier stage. At final, the self oscillation is realized at the resonance frequency of the drive mode with controlled oscillation amount.

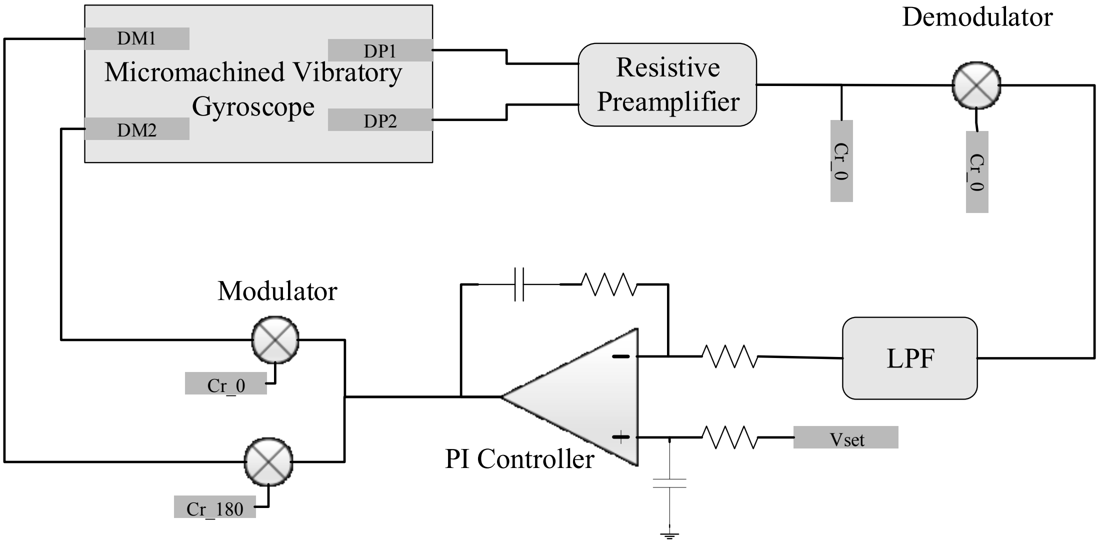

Figure 3.4: Block diagram of the closed loop drive mode controller.

There are important design parameters that should be considered to ensure the reliable, robust, and stable operation while designing the control electronics and loop parameters. The generally defined parameters for a control loop are settling time, phase margin, gain margin, damping factor, overshoot and steady-state error. There are also some other design rules for different system. The main two control systems are set-point tracking and disturbance rejection systems. In our system, we firstly reach to the set point and then reject the disturbances in operation. So, our control design strategy should focus on disturbance rejection. Disturbance rejection systems generally have lower phase margin about 45° to damp the disturbances effectively and the poles of the system should not be canceled by a zero, because a necessary and sufficient condition for controllability is that no single pole of the system is cancelled by a zero in all of the elements of the transfer-function. If such cancellation occurs, the system cannot be controlled in the direction of the cancelled mode [28]. This means that, any disturbance in the mechanical system is damped by only the damping of the mechanical system, because the effect of the pole is cancelled by the zero of electronics. The other important thing for the studied system is the very high Q-factor of the mechanical structure that can be modeled as almost an integrating system, because as a rule of thumb, when the closed loop bandwidth is more than 10 times of the controlled system, the system can be modeled as integrating process. This modeling has advantages over exact modeling, while designing robust controller independent from the Q-factor of the system without any performance loss. After deciding the design requirements and general system properties, design process can continue with the loop modeling.

The mechanical model of the drive mode includes voltage to force, force to velocity, and velocity to current. The transfer function of them can be written as in Equation 3.5, Equation 3.6, and Equation 3.7 respectively.

$$\frac{F(s)}{Vac(s)} = -\frac{\partial C}{\partial x}.Vprof \qquad 3.5$$

$$\frac{\mathrm{V(s)}}{\mathrm{F(s)}} = \frac{\mathrm{s}}{\mathrm{m.s^2 + b.s + k}} \qquad 3.6$$

$$\frac{I(s)}{\mathrm{V}(s)} = \frac{\partial C}{\partial x}.Vprof \qquad 3.7$$

The multiplication of the above equations with some changes gives the transconductance of the mechanical system as a voltage to current transfer function in Equation 3.6.

$$\frac{I(s)}{Vac(s)} = -(\frac{\partial C}{\partial x} Vprof)^2 \frac{s}{m.(s^2 + \frac{\omega_D}{Q_D}.s + \omega_D{}^2)} \tag{3.8}$$

As it can be seen from the Equation 3.8, the transfer function is second order and the control loop design for this transfer function is very complicated. In [24], the transfer function of the system modeled as first order system as in Equation 3.9.

$$\frac{\mathrm{I(s)}}{\mathrm{Vac(s)}} = -(\frac{\partial \mathrm{C}}{\partial \mathrm{x}} \mathrm{Vprof})^2 \frac{(\mathrm{Q_D}/\mathrm{w_D})}{\left(1 + \mathrm{s}\left(\frac{2\mathrm{Q_D}}{\mathrm{w_D}}\right)\right).\mathrm{m}} \tag{3.9}$$

The Equation developed in [24] made the design process easier, but it requires Q-factor of the each sensor while designing controller. In this study, the model of the mechanical structure is modeled as an integrator, because of the very low bandwidth of the structure compared to closed loop bandwidth. Finally, the modified drive mode model can be written as in Equation 3.10.

$$\frac{\mathrm{I(s)}}{\mathrm{Vac(s)}} = -(\frac{\partial \mathrm{C}}{\partial \mathrm{x}} \mathrm{Vprof})^2 \frac{1}{2.\mathrm{s}.\mathrm{m}} \tag{3.10}$$

The “Butterworth” type second order low pass filter with a multi-feedback topology is inserted in the drive control loop having the transfer function as in Equation 3.11. This type of low pass filter is chosen for its stability and easiness.

$$\mathrm{H_{LPF}(s)} = \frac{\mathrm{Vout(s)}}{\mathrm{Vin(s)}} = -\frac{\omega_c{}^2}{\mathrm{s}^2 + 2.\omega_c.\mathrm{s} + \omega_c{}^2} \tag{3.11}$$

The loop requires a difference amplifier to produce an error signal for the controller, but an op-amp type PI controller does not require any difference amplifier due to difference properties of input stage of an op-amp. The transfer function of this PI controller can be written as follow:

$$H_{PI}(s) = \frac{K_I(1 + sK_P/K_I)}{s} \tag{3.12}$$

This controller has also first order filter at the set point input. This filter is used as set-point weight and feedback noise reduction. If the PI controller implemented without the set-point filter, controller introduces a zero at s=-1/T$_i$ in the closed-loop transfer function from set-point signal to output signal. Because of that this filter is necessary for smooth and high frequency noise free operation

After these explanations, the controller design can be started. The first thing in the controller design is to create an open loop transfer function of the loop. The open loop transfer function of the loop can be described by the combination of drive mode, preamplifier, demodulator, modulator, LPF, and PI controller's transfer functions as in Equation 3.13.

$$H_{OL}(s) = (\frac{\partial C}{\partial x}Vprof)^2 \frac{1}{2.s.m} A_{pre} K_{Demod} H_{LPF}(s) \frac{K_I(1 + sK_P/K_I)}{s} K_{Mod} \tag{3.13}$$

The second thing while designing a controller is to decide the type of the controller strategy. In this case, the controller will be designed in disturbance rejection controller type. In this type phase margin was chosen as small as possible to effectively reject the disturbances while considering the robustness. In this design, phase margin was chosen as 45° and servo bandwidth of the control loop was selected as 20Hz, that is enough for this loop, because the settling time highly dominated by actuator saturation about 100msec for ramp-up time. Moreover, higher bandwidth systems insert higher noise to the system at its bandwidth, because of that bandwidth should be set as low as possible according to requirements.

After we decide the control parameters, the open loop transfer function can be written with parameters for easy controller design as in Equation 3.14.

$$H_{OL}(s) == c.\frac{1}{s}.\frac{1}{(1 + b.s)^2}.\frac{(1 + a.s)}{s} \tag{3.14}$$

Where, a, b, and c are $K_p/K_I$ of the PI controller, inverse of the LPF's cut-off frequency, and $(\frac{\partial C}{\partial x}Vprof)^2\frac{1}{2.m}A_{pre}K_{Demod}K_{LPF}K_IK_{Mod}$ respectively. The phase and gain characteristics of the $H_{OL}\,(s)$ can be written as follow:

$$\angle \mathrm{H_{OL}}\,(\omega) == -18\mathring{0} - 2.\arctan(\mathrm{b}.\omega) + \arctan\,(\mathrm{a}.\omega) \qquad 3.15$$

$$|\mathrm{H_{OL}}\,(\omega)| = \mathrm{c}.\frac{1}{\omega^2}.\frac{(1+(\mathrm{a}.\omega)^2)^{0.5}}{1+(\mathrm{b}.\omega)^2}. \qquad 3.16$$

The important design parameters of this controller are the desired closed loop bandwidth, a, and b. Moreover the relation between them defines the robustness of the controller. The robustness performance of this controller is chosen as when the loop gain changes ±50%, phase margin should not decrease under 45°. In order to provide this robustness, Phase margin should be placed, when the $\angle H_{OL}\,(\omega)$ is at maximum phase as in Figure 3.5. Extra to that, the zero of the PI controller is set 1/12.5 times of the low pass filter cut-off frequency. After that the open loop gain is set to 0 dB by changing the PI controller gain at the maximum phase as in Figure 3.5. The designed control loop parameters can be seen at Table 3.1.

Table 3.1: The design parameters of the Drive mode amplitude control loop satisfying robustness to loop gain and Q-factor changes.

| | |
|---|---|
| LPF cut-off frequency | 100Hz |
| Zero of the PI controller | 8Hz |
| Pole of the set-point filter | 6Hz |
| Phase Margin | 45° |
| Gain Margin | 18.8dB |
| Closed loop disturbance rejection bandwidth | 26Hz |
| Closed loop set-point bandwidth | 10Hz |
| Q-Factor range for 10kHz resonance frequency | More than 10,000 |

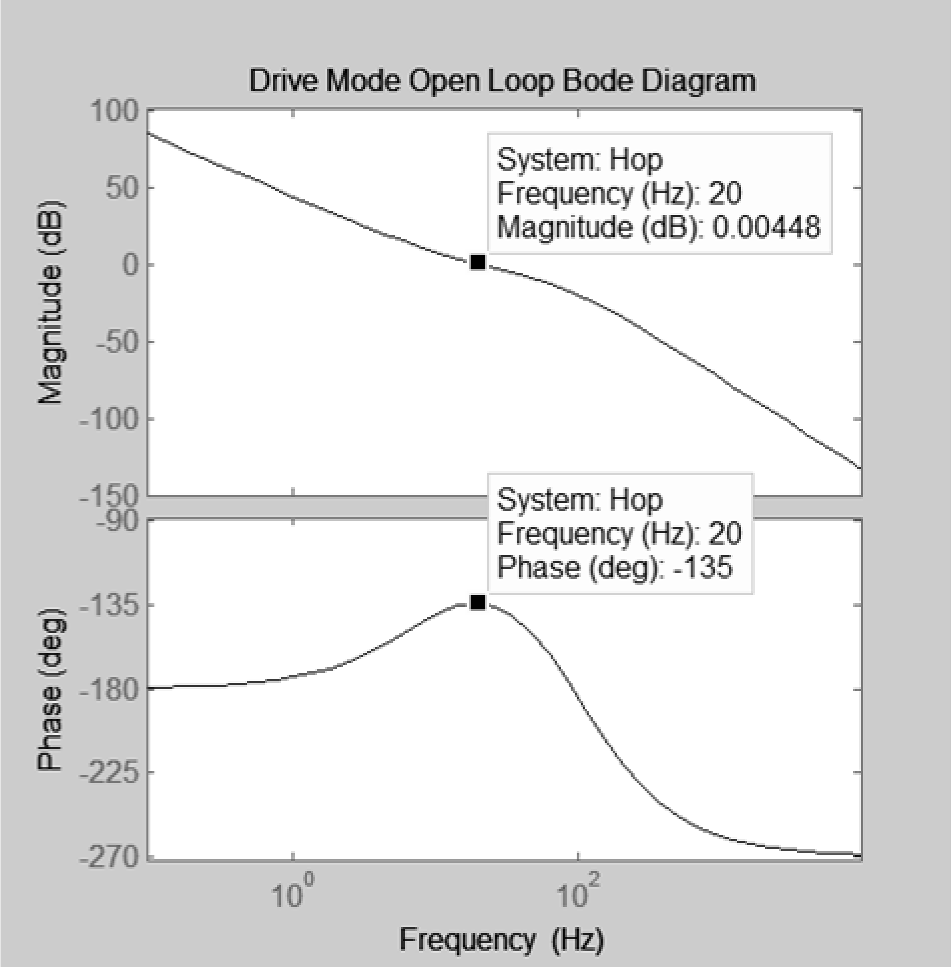

Figure 3.5: The open loop transfer function of the drive loop having 45° phase margin and18.8 dB gain margin.

The simulated closed loop transfer functions of the set-point response, the disturbance rejection response, and the disturbance to LPF output response can be seen at Figure 3.6, Figure 3.7, and Figure 3.8. Moreover, the step responses to the set-point and disturbance can be seen at Figure 3.9 and Figure 3.10, respectively.

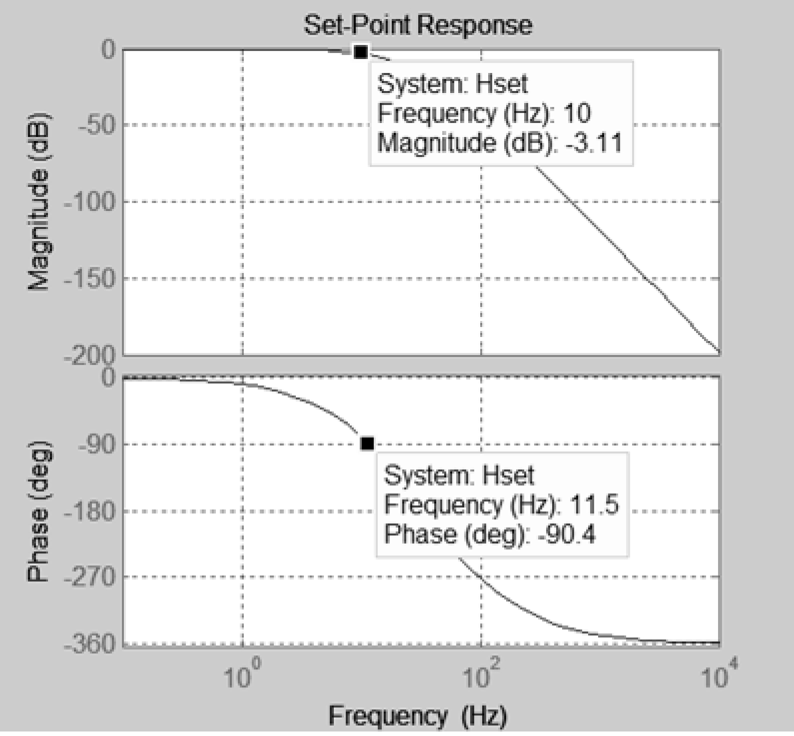

Figure 3.6: The closed loop set-point response of the drive mode control loop having 10Hz bandwidth and 11.5Hz 90° phase shift bandwidth.

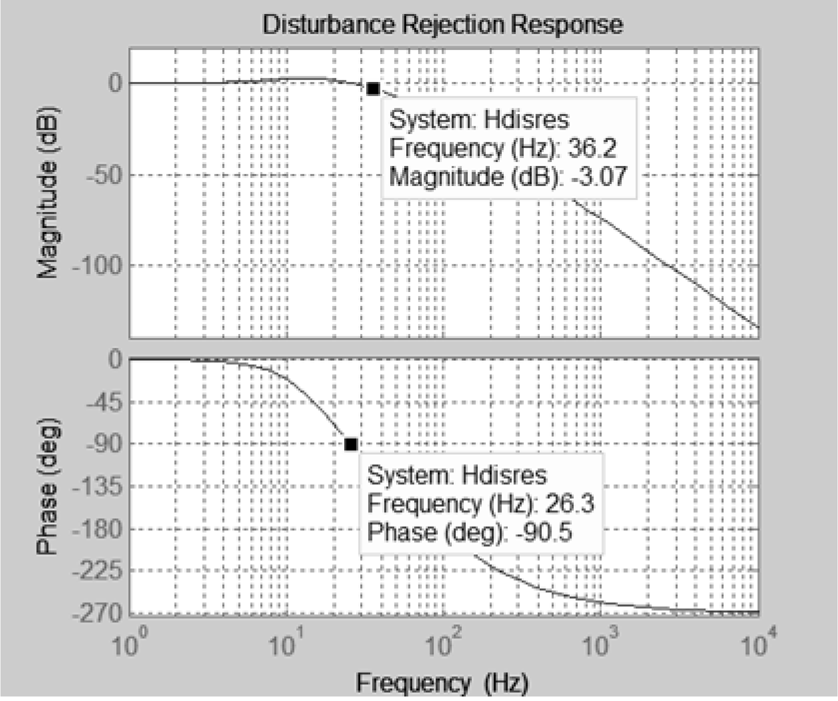

Figure 3.7: The closed loop disturbance rejection response of the drive mode control loop having 36Hz bandwidth and 26Hz 90° phase shift bandwidth.

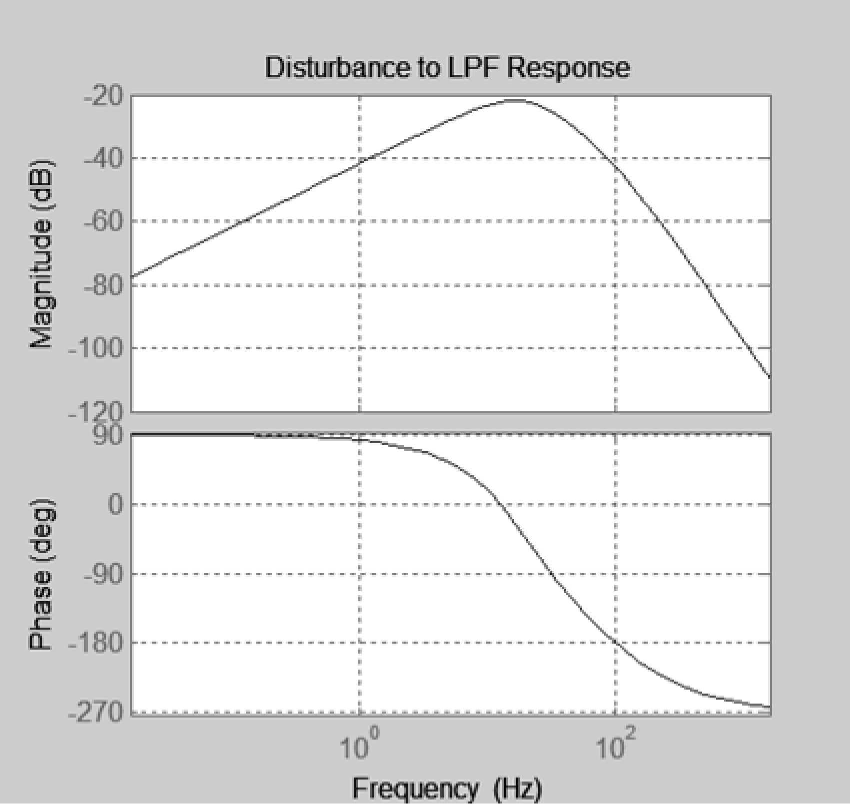

Figure 3.8: The disturbance to LPF output response showing the damping performance of the disturbance rejection loop.

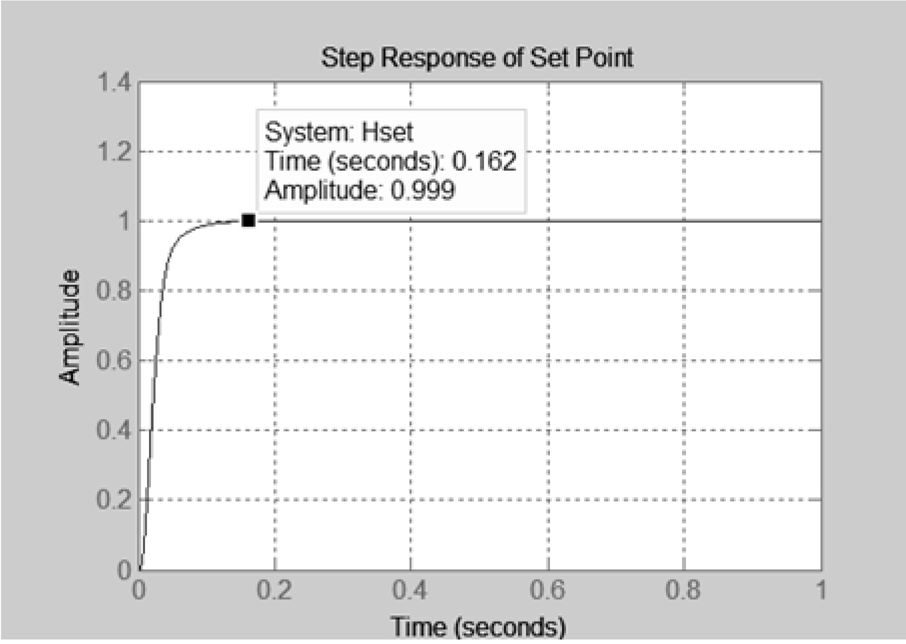

Figure 3.9: The set-point response of the set point applied to the drive PI controller and observed LPF output as a drive displacement. Settling in %0.1: 160msec.

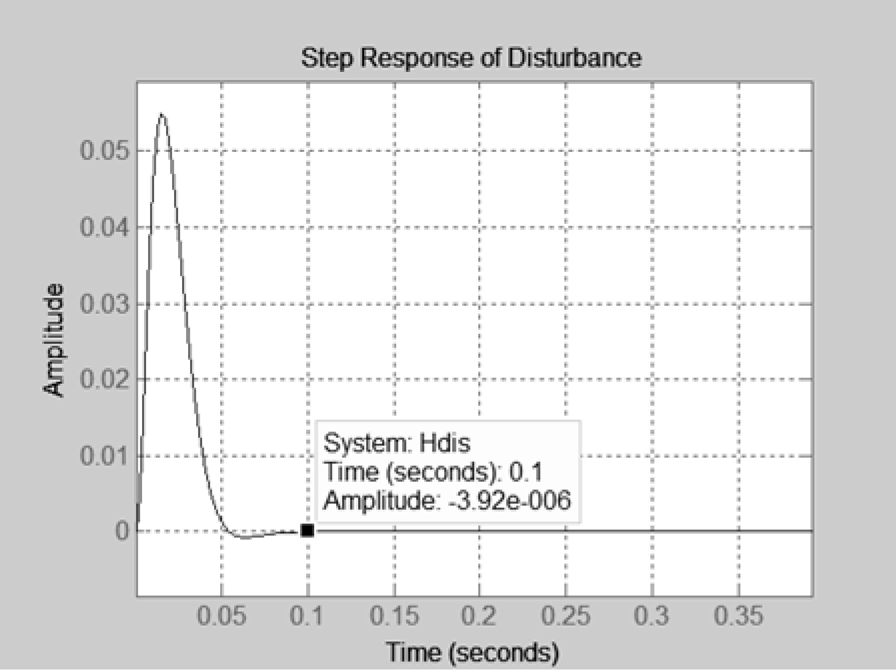

Figure 3.10: The set-point response of the disturbance applied to the drive motor electrodes and observed LPF output as a drive displacement. The disturbance rejection achieved in 100msec.

However, in the implemented circuit there are some non-idealities due to the boundaries defined by supply voltages. When the loop simulated with the mentioned non-idealities, the op-amp in the controller saturates and lead integrator wind-up. The wind-up problem behaves like an external disturbance. This disturbance is damped after the controller starts to operate in the linear region by loosing extra time to settle and higher overshoot than the simulated one in MATLAB. In order to effectively understand the non-idealities, a model of the drive mode and the circuits are implemented in LTSpice as in Figure 3.11 and Figure 3.12 respectively.

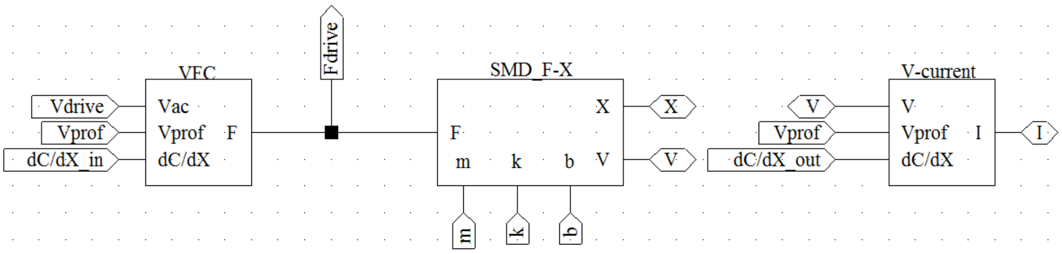

Figure 3.11: The modeled drive mode in LTSpice including all nonlinearities.

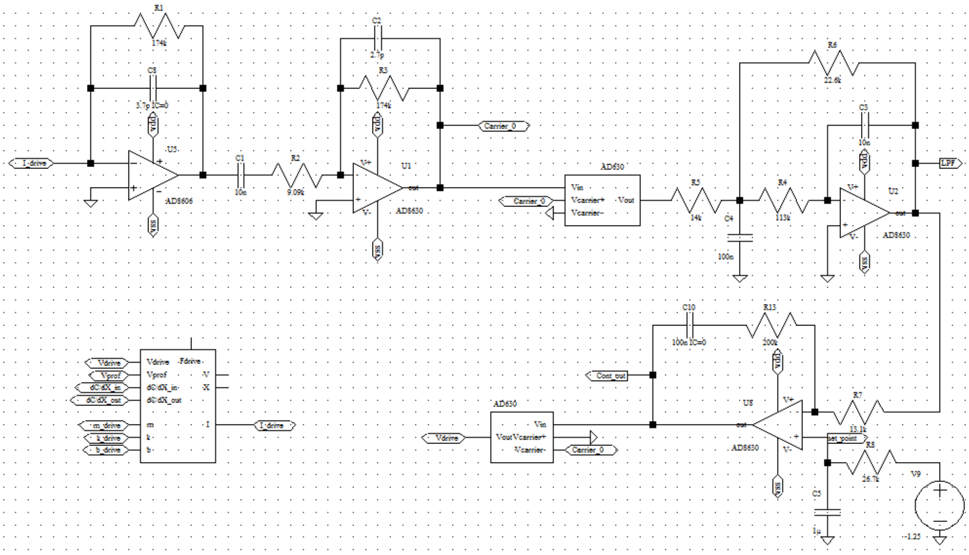

Figure 3.12: The drive control loop simulation environment implemented with LTSpice including all electrical and mechanical nonlinearities.

After, the spice implementation is constructed; the designed control parameters and the mechanical sensor parameters are set. The settling characteristic of the implemented system is simulated for 50,000 Q-factor and 10,000 Q-factor to prove the robustness of the controller to the Q-factor changes. The simulation results of these can be seen at Figure 3.13 and Figure 3.14 respectively.

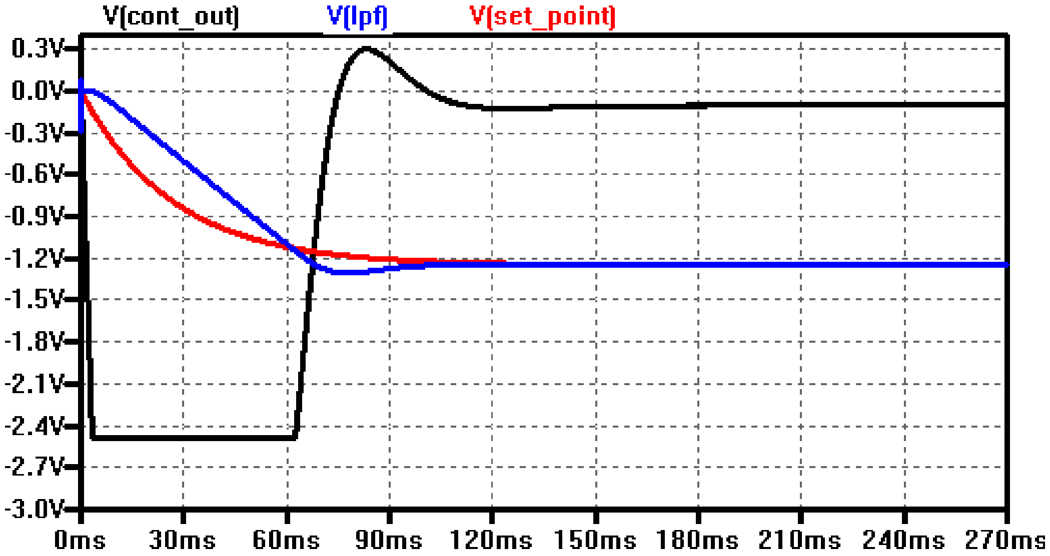

Figure 3.13: The settling characteristic of the designed drive control loop implemented in LTSpice. Q_Factor:50,000 , Settling in %0.1 error band: 163msec, Overshoot: %4. Black: PI controller output, Blue: Low pass filter output showing the displacement, Red: Set-point voltage applied with the set-point weighting function.

As it can be seen from the Figure 3.13, there is %4 overshoot in the system, but when the system is simulated in MATLAB as shown in Figure 3.9, there is no overshoot due to critically damped characteristics. The explanation of the overshoot in the SPICE simulation is due to integrator wind-up. The op-amp saturates and extra charging occurs in the capacitor over the PI controller and creates disturbance to the system and this disturbance cancelled by disturbance rejection loop that is not have set-point weighting. Therefore, overshoot occurs in the system within the acceptable level.

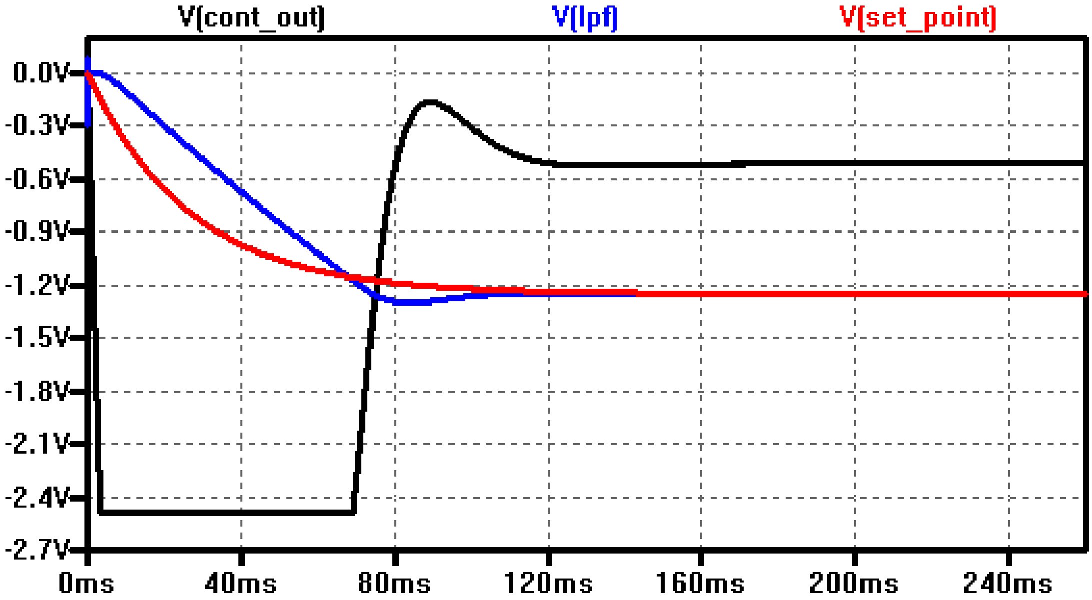

Figure 3.14: The settling characteristic of the designed drive control loop implemented in LTSpice. Q_Factor:10,000 , Settling in %0.1 error band: 165msec, Overshoot: %4. Black: PI controller output, Blue: Low pass filter output showing the displacement, Red: Set-point voltage applied with the set-point weighting function.

The Figure 3.13 and Figure 3.14 showed that when we model the drive mode as an integrating system excluding the Q-factor variations from sensor to sensor and design the controller according to an integrating sensor characteristic with mentioned controller design rules, the system controlled effectively and robustly for different Q-factors.

## 3.3 Sense Mode Control Electronics and Controller Design for MEMS Gyroscope

The closed loop rate sensing system is used to get the rate information by rebalancing the Coriolis acceleration induced force applied to the proof mass. Open loop implementation of the rate loop has some disadvantages due to high dependence to the mechanical transfer function, such as the system bandwidth and the scale factor highly changes form sensor to sensor and time to time. In order to solve the mentioned issues, closed loop rate sensing can be used effectively, because bandwidth and scale factor can be controlled by closed loop electronics more stable than open loop electronics.

The first thing in the control loop design is to model all the modules as possible. Because of that, mechanisms and electrodes are modeled. The mechanical model of the sense mode includes voltage to force, force to velocity, and velocity to current. The transfer function of them can be written as in Equation 3.17, Equation 3.18, and Equation 3.19 respectively.

$$\frac{\mathrm{F(s)}}{\mathrm{Vac_{FF}(s)}} = -\frac{\partial \mathrm{C_{FF}}}{\partial \mathrm{x}}.\mathrm{Vprof} \qquad 3.17$$

$$\frac{\mathrm{V(s)}}{\mathrm{F(s)}} = \frac{\mathrm{s}}{(\mathrm{m_{PM}} + \mathrm{m_S}).\mathrm{s}^2 + \mathrm{b.s} + \mathrm{k_S}} \qquad 3.18$$

$$\frac{\mathrm{I_{SP}(s)}}{\mathrm{V(s)}} = \frac{\partial \mathrm{C_{SP}}}{\partial \mathrm{x}}.\mathrm{Vprof} \qquad 3.19$$

The multiplication of the above equations with some changes gives the transconductance of the mechanical system as a voltage to current transfer function as in Equation 3.20.

$$\frac{I_{SP}(s)}{Vac_{FF}(s)} = -\frac{\partial C_{SP}}{\partial x}.\frac{\partial C_{FF}}{\partial x}.(Vprof)^2.\frac{s}{(m_{PM} + m_S).(s^2 + \frac{\omega_S}{Q_S}.s + \omega_S{}^2)} \qquad 3.20$$

As it can be seen from the Equation 3.20, the transfer function is second order and the control loop design for this transfer function is very complicated. In [24], the transfer function of the system modeled for matched and mismatched cases as in Equation 3.21 and Equation 3.22 respectively. The Equation 3.21 is also be modified with the method mentioned in the drive mode modeling as an integrating process.

$$\frac{I_{SP}(s)}{Vac_{FF}(s)} = -\frac{\partial C_{SP}}{\partial x} . \frac{\partial C_{FF}}{\partial x} . (Vprof)^2 \frac{1}{2.(m_{PM} + m_S).s} \qquad 3.21$$

$$\frac{I_{SP}(s)}{Vac_{FF}(s)} = -\frac{\partial C_{SP}}{\partial x} . \frac{\partial C_{FF}}{\partial x} . (Vprof)^2 \frac{\omega_S - \omega_D}{2.(m_{PM} + m_S).(s^2 + \frac{\omega_S}{Q_S}.s + (\omega_S - \omega_D)^2)} \qquad 3.22$$

The another module of this loop is a low pass filter(LPF) designed as a third order low pass filter with a multi-feedback topology having the transfer function as in Equation 3.23. This type of low pass filter is chosen for its stability and easiness.

$$H_{LPF}(s) = \frac{Vout(s)}{Vin(s)} = -\frac{\omega_c^3}{(s + \omega_c)^3} \qquad 3.23$$

The loop requires a difference amplifier to produce an error signal for the controller, but an op amp type PI and I controllers do not require any difference amplifier due to difference properties of inputs. The transfer function of the PI and I controllers can be written as follow:

$$H_{PI}(s) = \frac{K_I(1 + sK_P/K_I)}{s} \qquad 3.24$$

$$H_I(s) = \frac{K_I}{s} \qquad 3.25$$

### 3.3.1. Force-Feedback Loop Controller Design for Mode-Matched Condition

In this section, controller will be designed for the mode-matched case and then controller will designed for the mismatched case due to so different transfer functions of the different cases. In mode-matched case, the first thing is to create an open loop transfer function of the loop. The open loop transfer function of the loop can be described by the combination of sense mode in mode-matched condition, preamplifier, demodulator, modulator, LPF, and PI controller's transfer functions as in Equation 3.26. These modules are implemented in the CMOS readout circuit as in Figure 3.15.

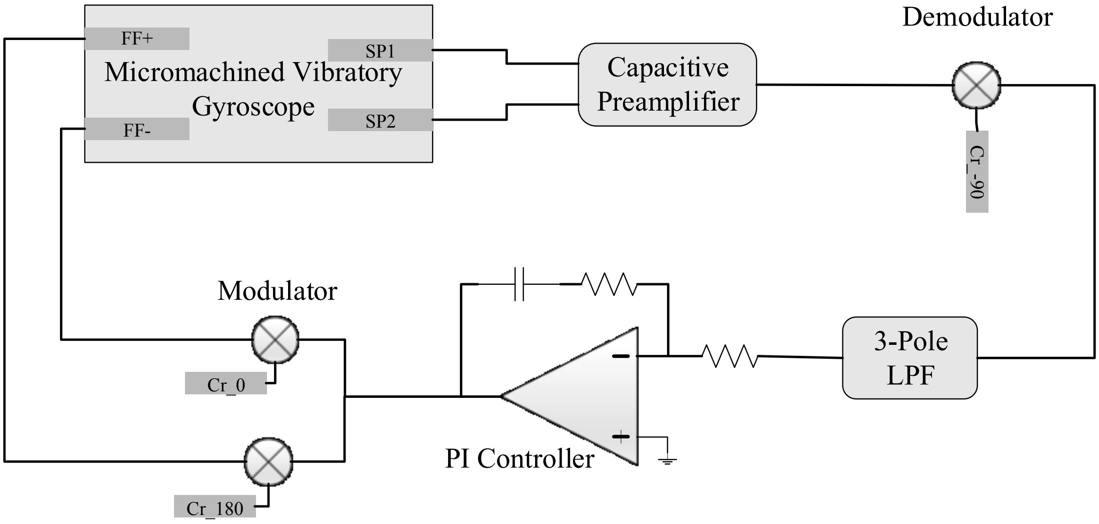

Figure 3.15: Block diagram of the closed loop force feedback controller for mode-match operation of the MEMS gyroscope.

$$H_{OL}(s) = \frac{\partial C_{SP}}{\partial x}.\frac{\partial C_{FF}}{\partial x}.(\mathrm{Vprof})^2 A_{pre} K_{Demod} \frac{1}{2.(m_{PM} + m_S).s}. \qquad 3.26$$

$$H_{LPF}(s) \frac{K_I(1 + sK_P/K_I)}{s} K_{Mod}$$

The second thing while designing a controller is to decide the type of the controller strategy. In the mode-matched condition, the controller will be designed in disturbance rejection controller type with a PI controller, because controller has no set-point change and only reject disturbances that is the Coriolis induced forces on the mass. In this type phase, margin was chosen as small as possible to effectively reject the disturbances. Phase margin was chosen as 45° and 90° phase shift bandwidth of the control loop was selected as 100Hz. The other bandwidth definition of -3dB bandwidth is also higher than that, but in the control loop design, phase response is more important than amplitude response.

The important design parameters of this controller are the desired closed loop bandwidth, zero of the PI controller, and cut-off frequency of 3-pole LPF. The relation between them also defines the robustness of the controller. The robustness performance of this controller is chosen as when the loop gain changes ±30%, phase margin should not decrease under 45°. In order to provide this robustness, Phase margin should be placed, when the $\angle H_{OL}(\omega)$ is at maximum phase as in Figure 3.16, when the zero of the PI controller is set 1/12.5 times of the low pass filter cut-off frequency. After that, the open loop gain is set to 0 dB at that frequency by changing the PI controller's gain. Finally, the designed control loop parameters can be seen at Table 3.2.

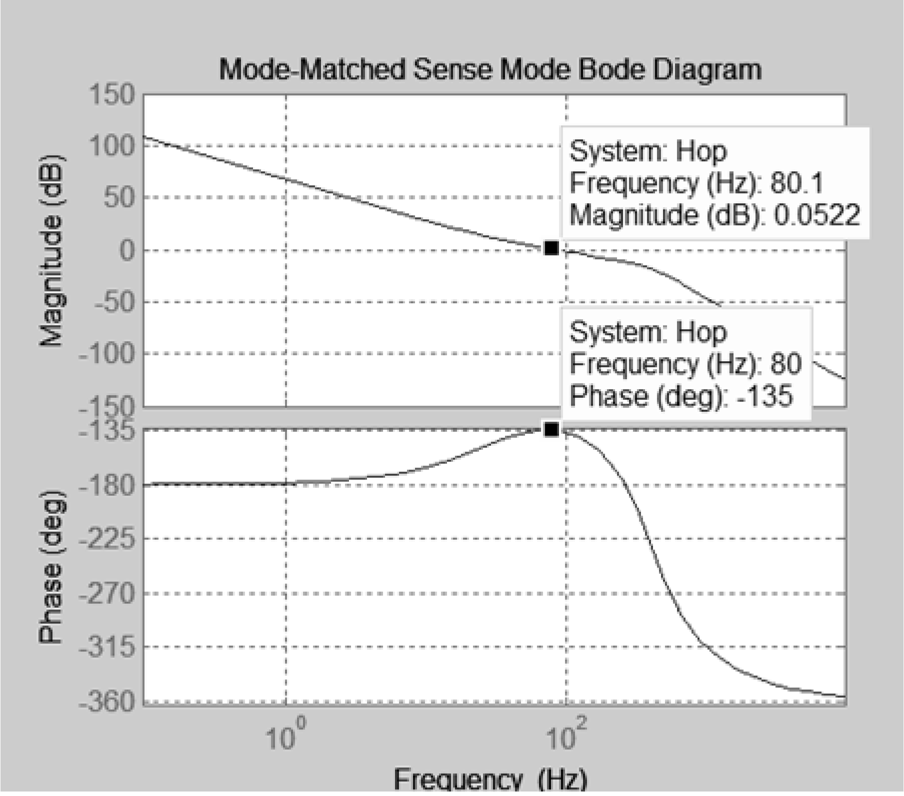

Figure 3.16: The open loop transfer function of the mode-matched sense loop having 45° phase margin and11.2 dB gain margin.

Table 3.2: The design parameters of the mode-matched sense mode rate rebalancing control loop satisfying robustness to loop gain and Q-factor changes.

| | |
|---|---|
| LPF cut-off frequency | 400Hz |
| Zero of the PI controller | 32Hz |
| Phase Margin | 45° |
| Gain Margin | 11.2dB |
| Closed loop disturbance rejection 90° phase shift bandwidth | 105Hz |
| Q-Factor range for 10kHz resonance frequency | More than 500 |

The simulated closed loop transfer functions of the disturbance rejection response, and the disturbance to LPF output response can be seen at Figure 3.17 and Figure 3.18.

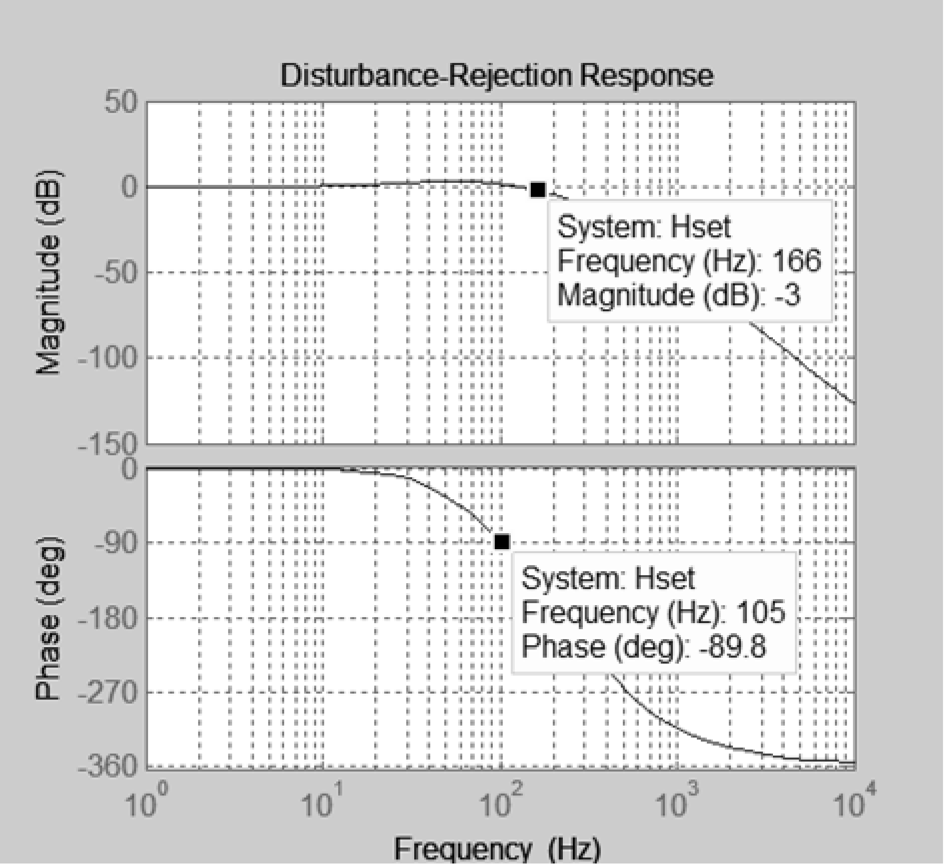

Figure 3.17: The closed loop disturbance(rate) rejection response of the sense mode control loop having 166 Hz bandwidth and 105 Hz 90° phase shift bandwidth.

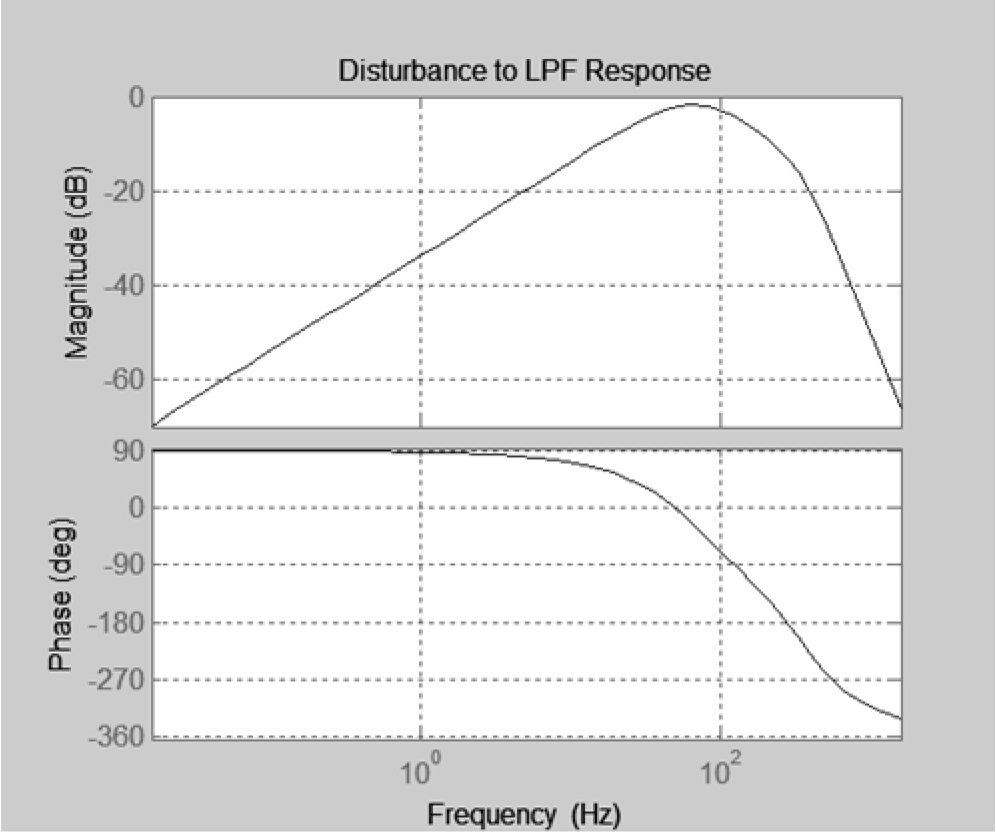

Figure 3.18: The disturbance to LPF output response showing the damping performance of the disturbance rejection loop.

The disturbance to LPF output response showing the damping performance of the rate rebalancing loop controller in the frequency band. The maximum value of this response should not exceed the 0dB, when it exceeds that value, the op-amps in the loop saturates at the full scale rate input.

Moreover, the step rate responses for rate applied from the MEMS structure and observed at the controller output and LPF output can be seen at Figure 3.19 and Figure 3.20 respectively. The Figure 19 is the most important response of the system showing MEMS gyroscope's response to the externally applied rate.

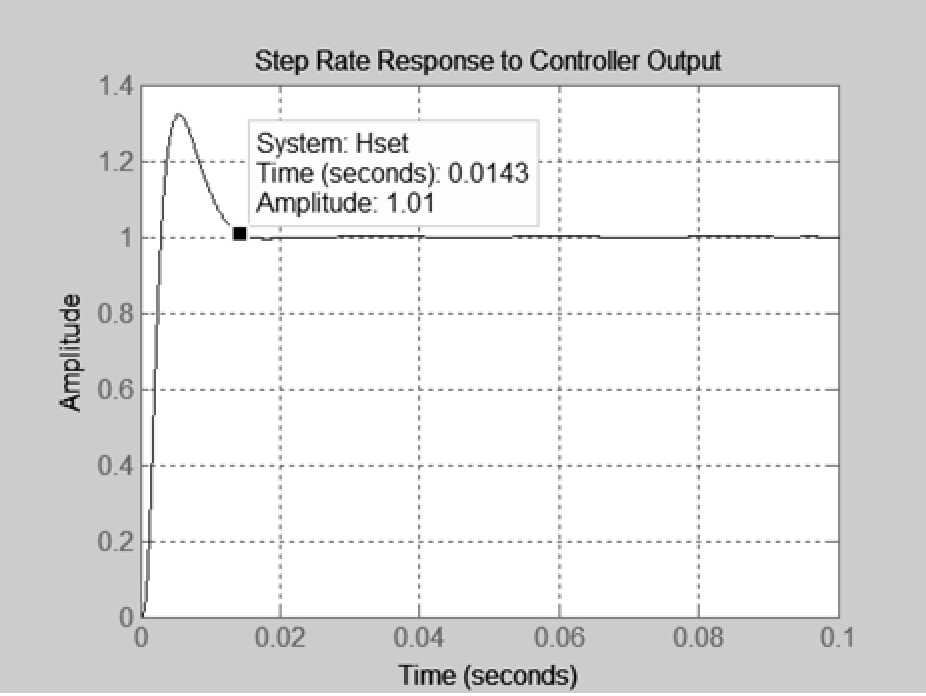

Figure 3.19: The step rate responses for rate applied to the MEMS structure and observed at the sense mode controller output. This response is used as rate information. Settling completed in %0.1 error band: 14.3msec.

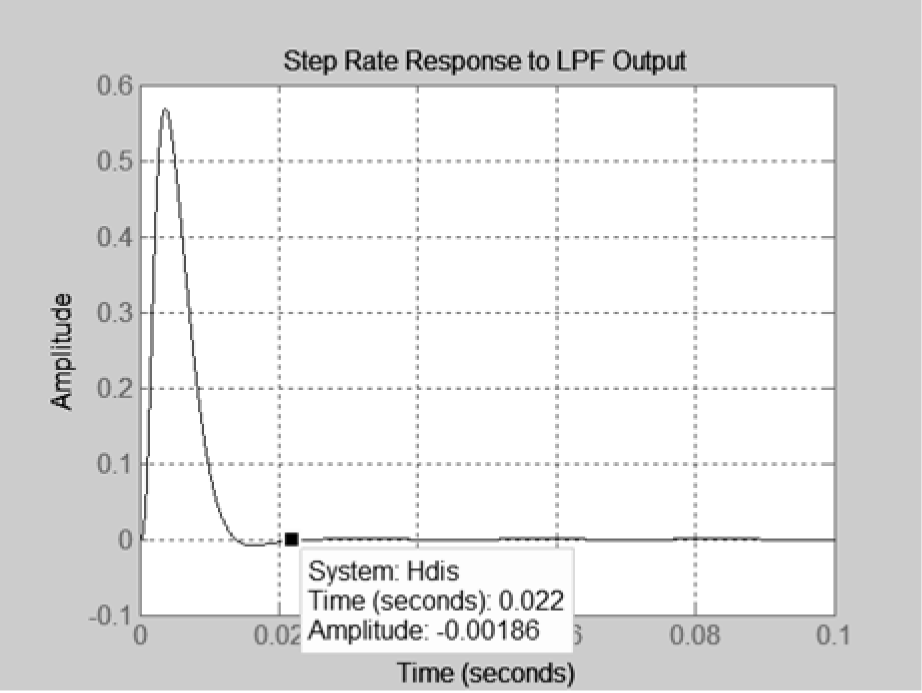

Figure 3.20: The step rate responses for rate applied to the MEMS structure and observed at the LPF output. This response is the measure of disturbance rejection performance. Rejection completed in %0.1 error band: 22msec.

Extra to MATLAB simulations, in order to effectively simulate the effects of non-idealities of the sense mode mechanics, simulation models are implemented in LTSpice as in Figure 3.21.

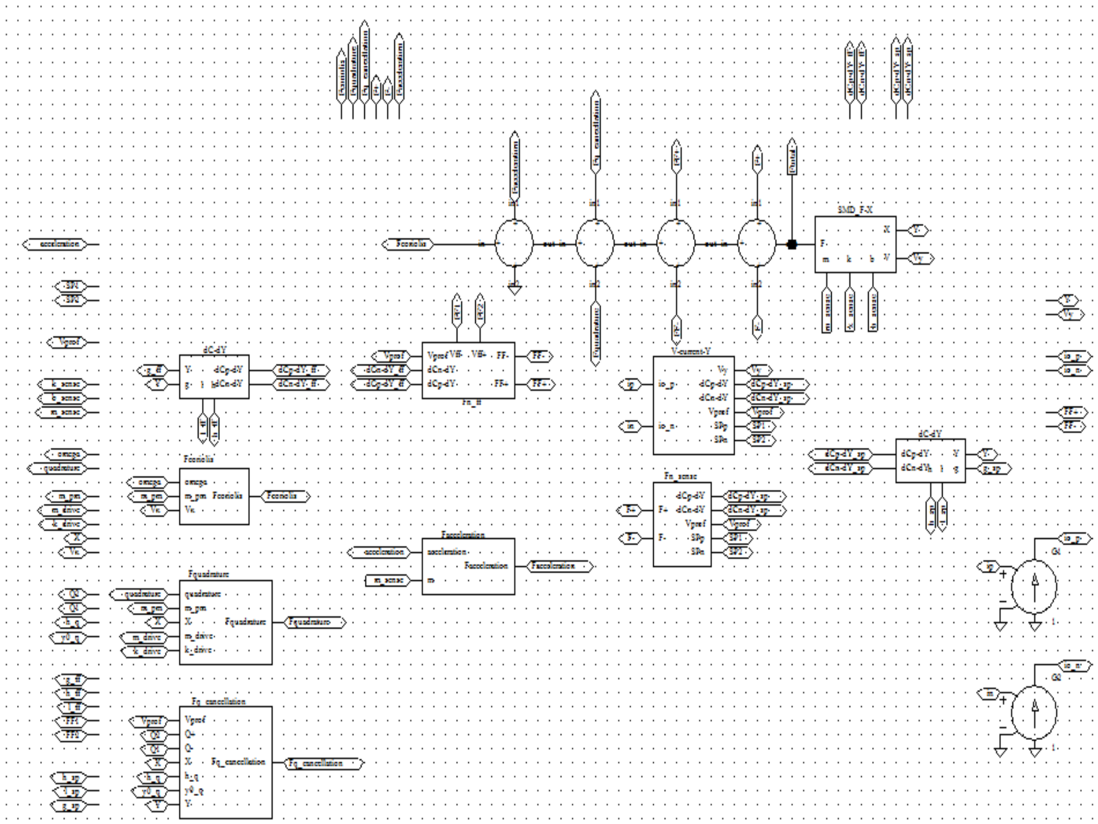

Figure 3.21: The modeled sense mode in LTSpice including all nonlinearities.

### 3.3.2. Force-Feedback Loop Controller Design for Mismatched Condition

In mismatched case, the first thing is to create an open loop transfer function of this loop. The open loop transfer function of the loop can be described by the combination of sense mode in mismatched condition, preamplifier, demodulator, modulator, LPF, and I controller's transfer functions as in Equation 3.27. These modules are implemented in the CMOS readout circuit as in Figure 3.22.

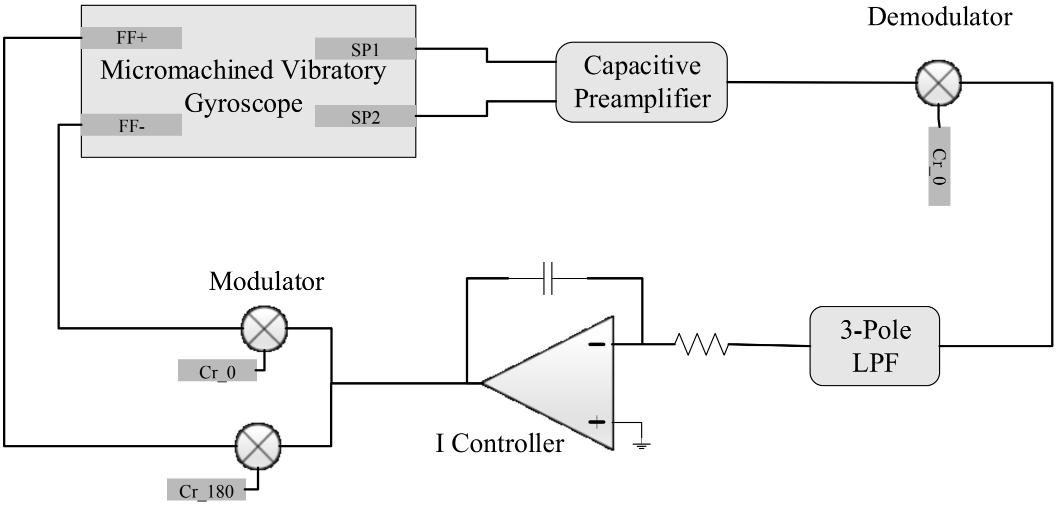

Figure 3.22: Block diagram of the closed loop force feedback controller for mismatch operation of the MEMS gyroscope.

$$H_{OL}(s) = \frac{\partial C_{SP}}{\partial x} . \frac{\partial C_{FF}}{\partial x} . (\mathrm{Vprof})^2 A_{pre} K_{Demod} H_{LPF}(s). \tag{3.27}$$

$$\frac{\omega_S - \omega_D}{2.(m_{PM} + m_S).(s^2 + \frac{\omega_S}{Q_S}.s + (\omega_S - \omega_D)^2)} \frac{K_I}{s} K_{Mod}$$

The second thing while designing a controller is to decide the type of the controller strategy. In the mismatched condition, the controller will be designed in disturbance rejection controller type with an I controller, because controller has no set-point change and only reject disturbances these are the Coriolis induced forces on the mass. In this type phase margin was chosen as small as possible to effectively reject the disturbances. Phase margin was chosen as 55°, and 90° phase shift bandwidth of the control loop was selected as 100Hz. The other bandwidth definition of -3dB bandwidth is also higher than that, but in control loop design, phase response is more important than amplitude response.

The important design parameters of this controller are the desired closed loop bandwidth, gain of I controller, and cut-off frequency of 3-pole LPF. The relation between them also defines the robustness of the controller. The robustness performance of this controller is chosen as when the loop gain changes ±30%, phase margin should not decrease under 55°. In order to provide this robustness, 3-pole LPF is used to obtain more than 150° phase shift at the resonance frequency difference of the two modes, not to make the system unstable due to sharp phase change at this frequency. The design parameters of this loop for 100Hz 90° phase shift bandwidth are 260Hz 3-pole LPF and 330Hz resonance frequency difference. After that, the open loop gain is set to 0 dB at 70Hz by changing the I controller's gain as in Figure 3.23. Moreover, all stability margins can be seen at Figure 3.24. Finally, the designed control loop parameters can be seen at Table 3.3.

Table 3.3: The design parameters of the mismatched sense mode rate rebalancing control loop satisfying robustness to loop gain and Q-factor changes.

| | |
|---|---|
| LPF cut-off frequency | 260Hz |
| Resonance Frequency Difference | 330Hz |
| Phase Margin | 58° |
| Gain Margin | 6.0dB |
| Closed loop disturbance rejection 90° phase shift bandwidth | 102Hz |
| Q-Factor range for 10kHz resonance frequency | Lower than 10000 |

The simulated closed loop transfer functions of the disturbance rejection response measuring rate, and the disturbance to LPF output response can be seen at Figure 3.25 and Figure 3.26. The closed loop bandwidth of the MEMS gyroscope is decided by analyzing this disturbance rejection response, because MEMS gyroscopes operating in rate mode with rate rebalancing loop.

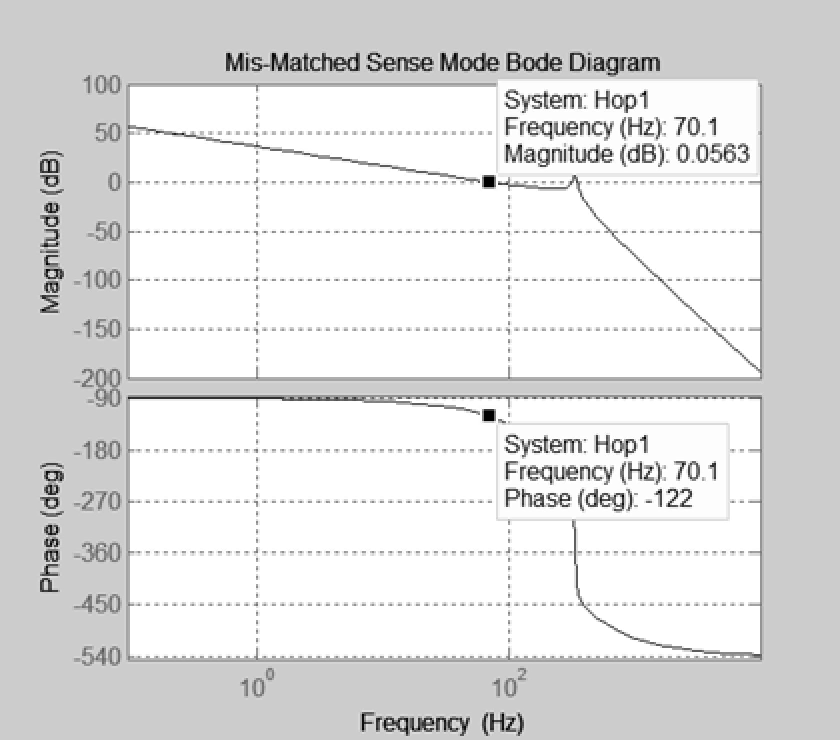

Figure 3.23: The open loop transfer function of the mismatched sense loop having 58° phase margin and 6.0dB gain margin.

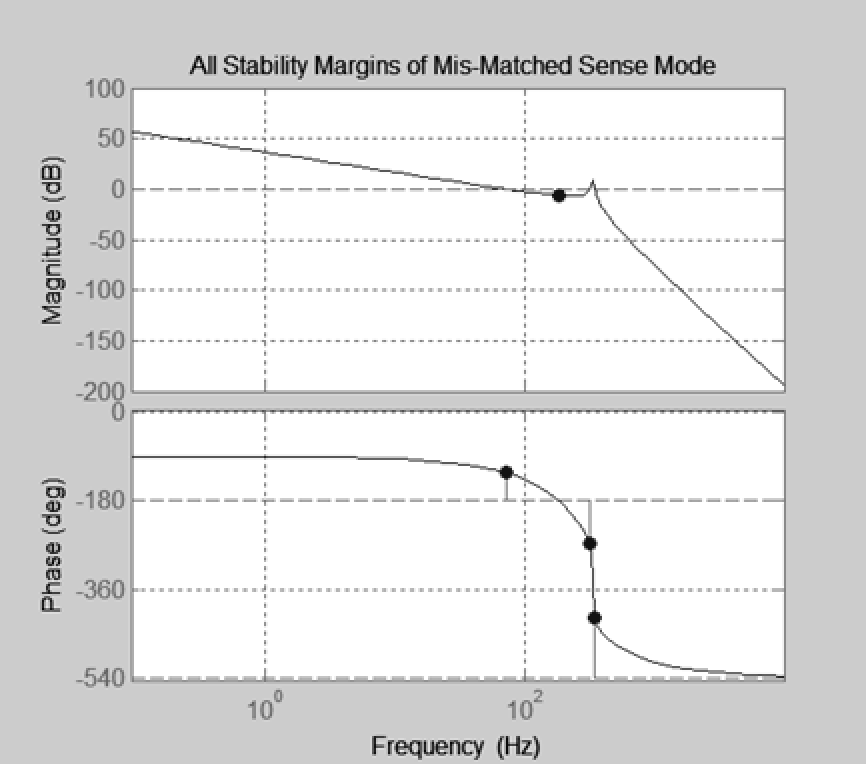

Figure 3.24: The open loop transfer function of the mismatched sense loop showing the all stability margins at -180° and -540°.

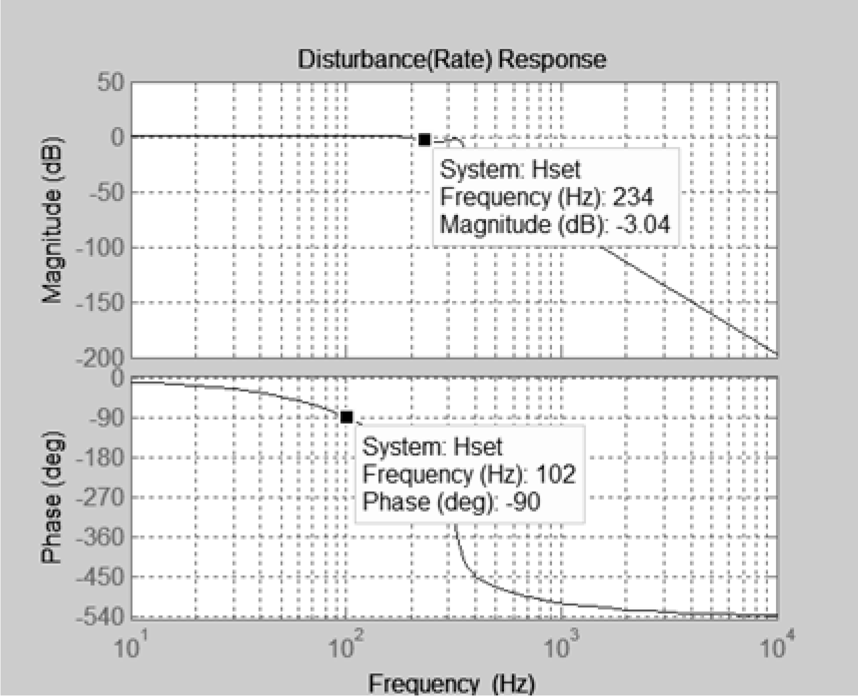

Figure 3.25: The closed loop disturbance(rate) rejection response of the mismatched sense mode control loop having 234 Hz -3dB bandwidth and 102 Hz 90° phase shift bandwidth.

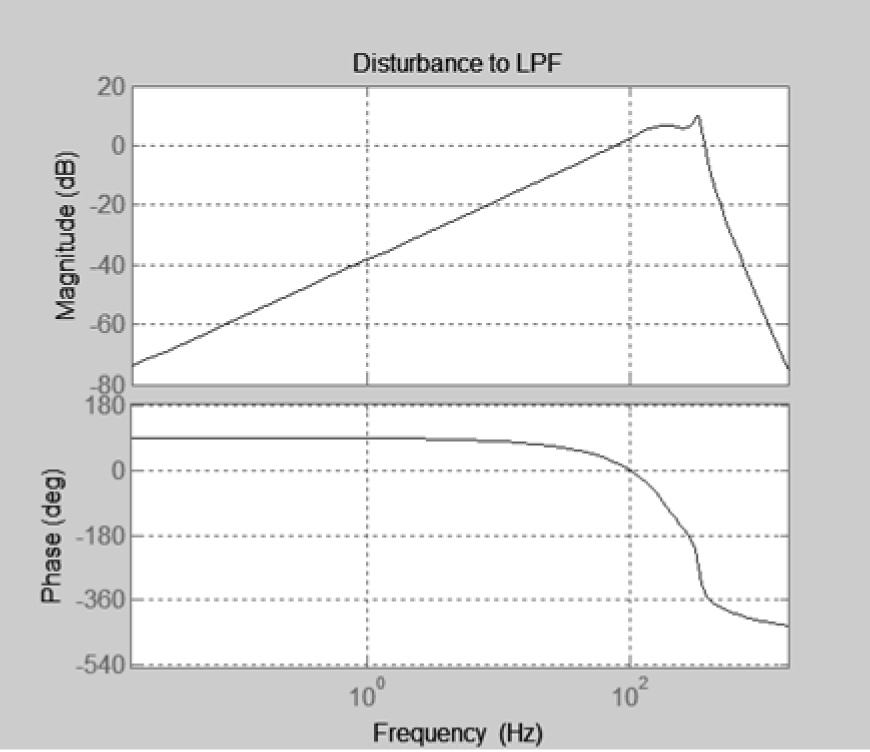

Figure 3.26: The disturbance to LPF output response showing the damping performance of the disturbance rejection loop.

The disturbance to LPF output response showing the damping performance of the rate rebalancing loop controller in the frequency band. The maximum value of this response should not exceed the 0dB, when it exceeds that value, the op-amps in the loop saturates at the full scale rate input at the highest frequency.

Moreover, the step rate responses applied from MEMS structure to controller output and LPF output can be seen at Figure 3.27 and Figure 3.28 respectively. The Figure 3.27 is the most important response of the system showing MEMS gyroscope's response to the externally applied rate.

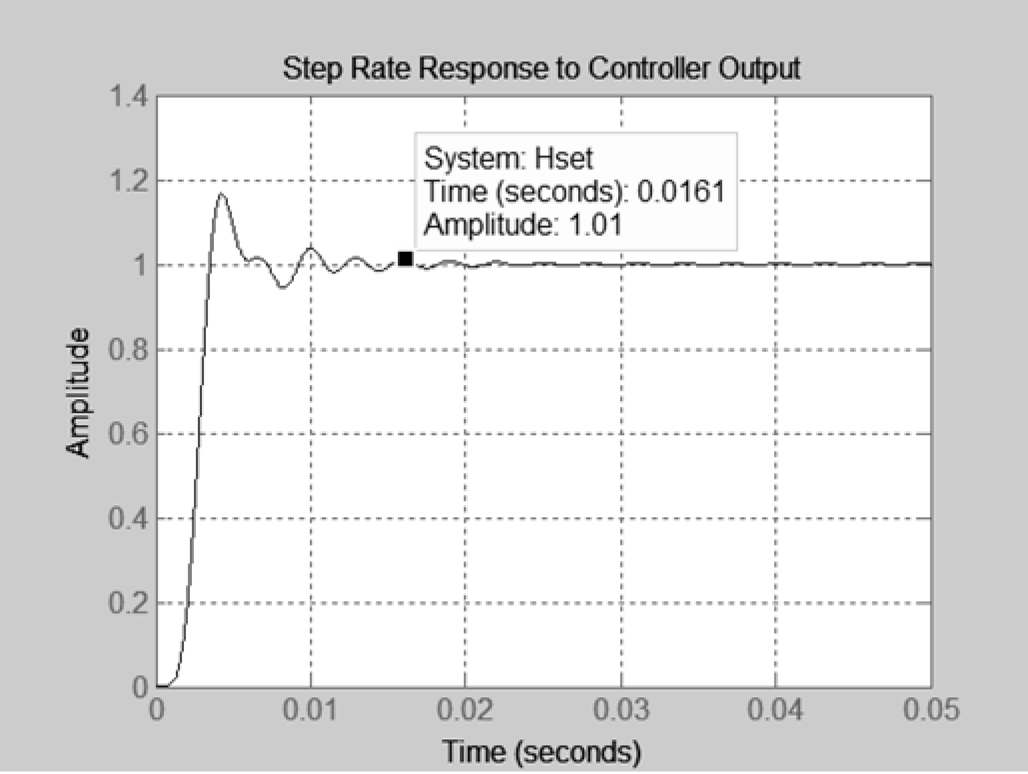

Figure 3.27: The step rate responses applied from MEMS structure to the sense mode controller output. This response is used as a rate information. Settling in %1: 16.1msec.

Extra to MATLAB simulations, in order to effectively simulate the effects of non-idealities of the sense mode mechanics, simulation models are implemented in LTSpice as in Figure 3.29.

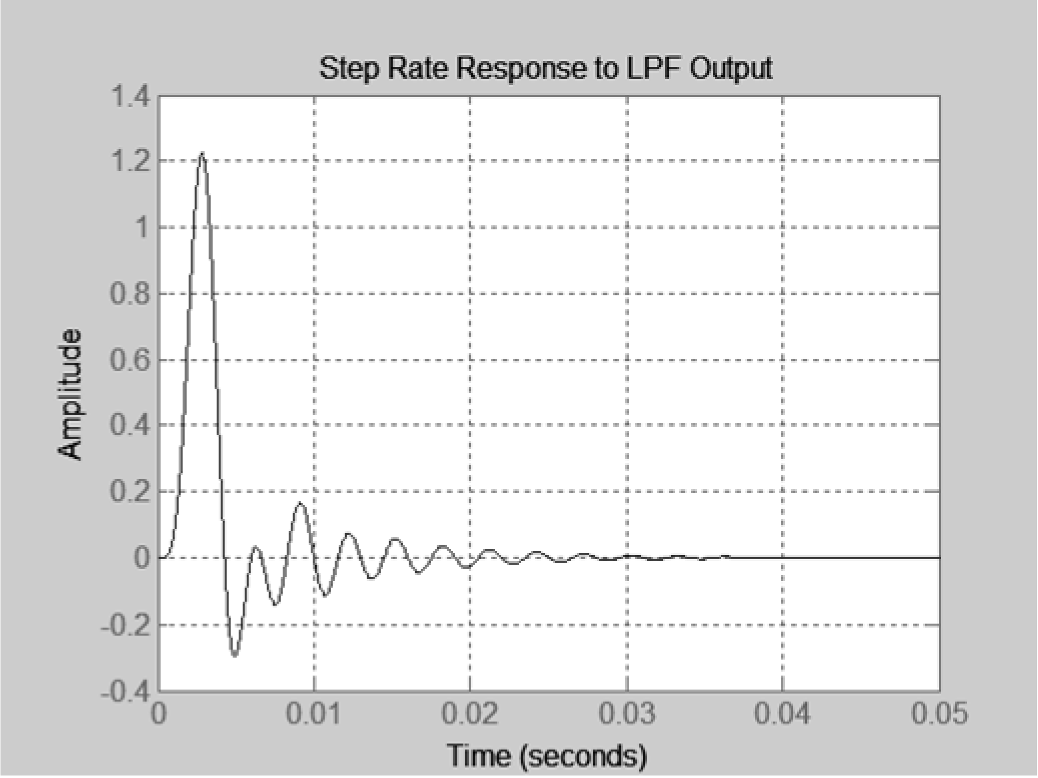

Figure 3.28: The step rate responses applied from MEMS structure to the LPF output. This response is the measure of disturbance rejection performance.

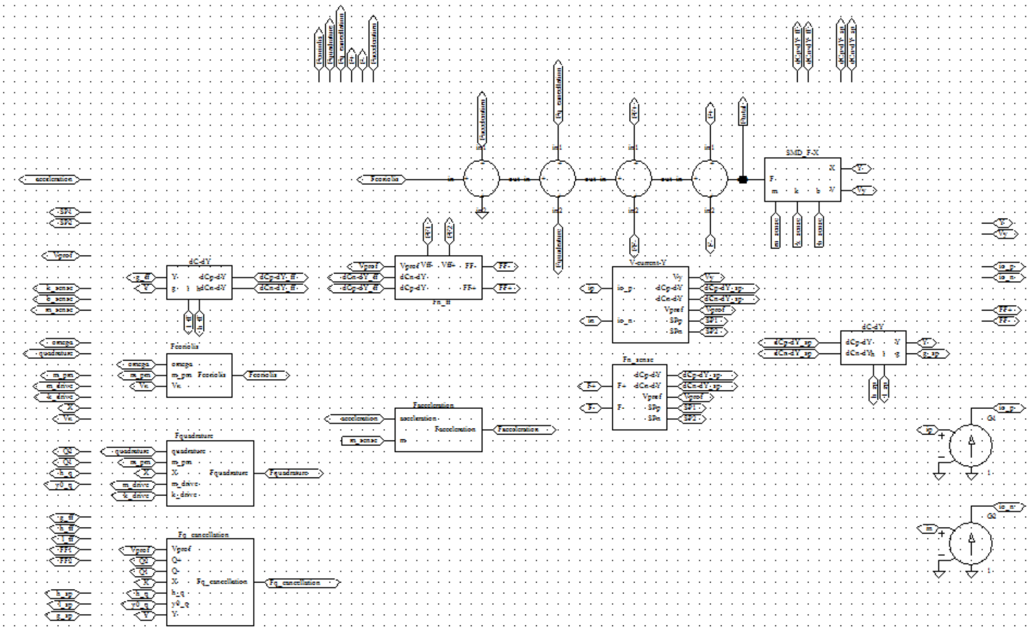

Figure 3.29: The modeled sense mode in LTSpice including all nonlinearities.

## 3.4 Quadrature Cancellation Mode Control Electronics and Controller Design for MEMS Gyroscope

The closed loop quadrature cancellation system is used to cancel the quadrature error while the system operating by creating a force in phase with quadrature error on the sense frame with a DC voltage. This DC voltage is modulated by special mechanical electrodes.

The first thing in the control loop design is to model all the modules as possible. Because of that, mechanisms and electrodes of the quadrature cancellation are modeled. The mechanical model of the quadrature cancellation includes voltage to force, force to velocity, and velocity to current. The transfer function of them can be written as in Equation 3.28, Equation 3.29, and Equation 3.30 respectively. These modules are implemented in the CMOS readout circuit as in Figure 3.30 and Figure 3.31 for mode-matched and mismatched operations respectively. The only difference in these two implementations are their demodulation phases to get the quadrature signal for both operations.

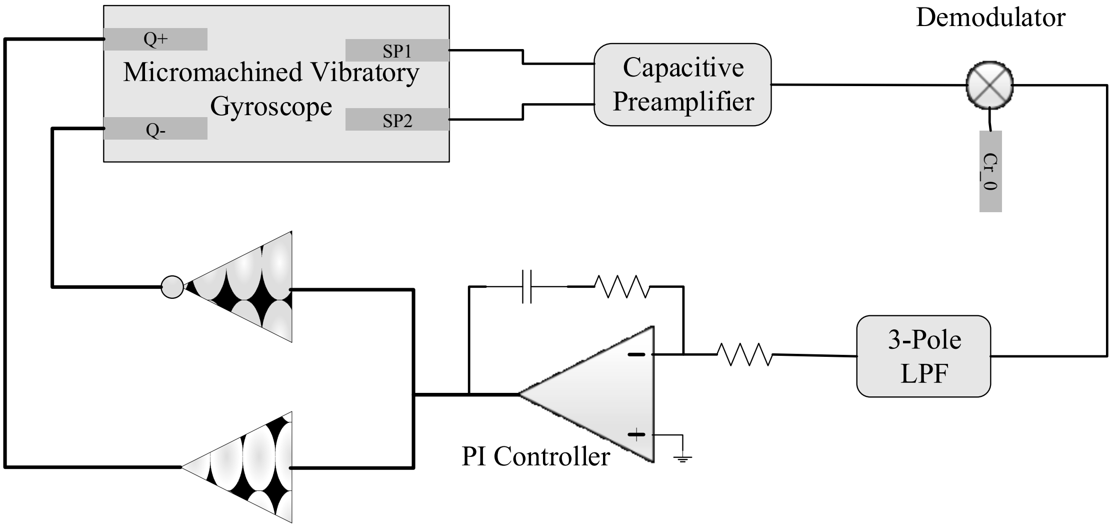

Figure 3.30: Block diagram of the closed loop quadrature controller for mode-match operation of the MEMS Gyroscope.

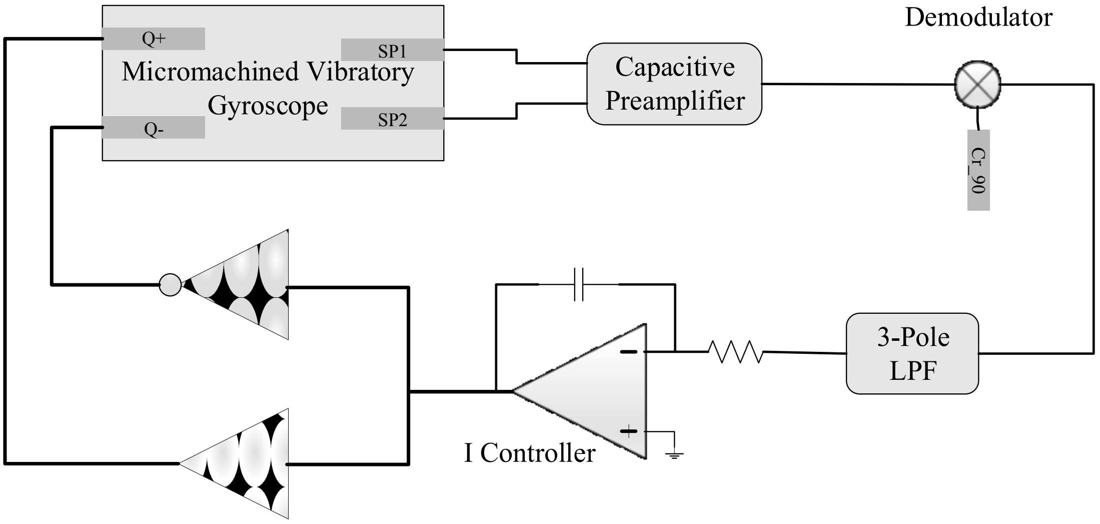

Figure 3.31: Block diagram of the closed loop quadrature controller for mismatch operation of the MEMS Gyroscope.

$$\frac{F(s)}{Vdc_Q(s)} = n.\frac{4.\mathcal{E}.Vprof\,.X.h}{{x_0}^2} \qquad 3.28$$

$$\frac{\mathrm{V(s)}}{\mathrm{F(s)}} = \frac{\mathrm{s}}{(\mathrm{m_{PM}} + \mathrm{m_S}).\,\mathrm{s}^2 + \mathrm{b.\,s} + \mathrm{k_S}} \qquad 3.29$$

$$\frac{I_{SP}(s)}{\mathrm{V}(s)} = \frac{\partial C_{SP}}{\partial x}.Vprof \qquad 3.30$$

The multiplication of the above equations with some changes gives the transconductance of the quadrature cancellation system as a voltage to current transfer function in Equation 3.31.

$$\frac{I_{SP}(s)}{Vdc_Q(s)} = n.\frac{4.\mathcal{E}.Vprof\,.X.h}{{x_0}^2}.\frac{\partial C_{SP}}{\partial x}.Vprof.\frac{s}{(m_{PM} + m_S).(s^2 + \frac{\omega_S}{Q_S}.s + {\omega_S}^2)} \qquad 3.31$$

As it can be seen from the Equation 3.31, the transfer function is second order and the control loop design for this transfer function is very complicated. In [24], the transfer function of the system modeled for the matched and mismatched cases as in Equation 3.32 and Equation 3.33 respectively. The Equation 3.32 is also modified with the method used in the drive mode modeling as an integrating process.

$$\frac{I_{SP}(s)}{Vdc_Q(s)} = n.\frac{4.\mathcal{E}.Vprof.X.h}{{x_0}^2}.\frac{\partial C_{SP}}{\partial x}.(Vprof).\frac{1}{2.(m_{PM}+m_S).s} \qquad 3.32$$

$$\frac{I_{SP}(s)}{Vdc_Q(s)}$$

$$= \frac{\partial C_{SP}}{\partial x}.n.\frac{4.\mathcal{E}.Vprof.X.h}{{x_0}^2}.Vprof\frac{\omega_S-\omega_D}{2.(m_{PM}+m_S).(s^2+\frac{\omega_S}{Q_S}.s+(\omega_S-\omega_D)^2)} \qquad 3.33$$

The another module of this loop is a low pass filter(LPF) designed as a third order low pass filter with a multi-feedback topology having the transfer function as in Equation 3.34. This type of low pass filter is chosen for its stability and easiness.

$$H_{LPF}(s) = \frac{Vout(s)}{Vin(s)} = -\frac{{\omega_c}^3}{(s+\omega_c)^3} \qquad 3.34$$

The loop requires a difference amplifier to produce an error signal for the controller, but an op amp type PI and I controllers do not require any difference amplifier due to difference properties of inputs. The transfer function of the PI and I controllers can be written as follow:

$$H_{PI}(s) = \frac{K_I(1+sK_P/K_I)}{s} \qquad 3.35$$

$$H_I(s) = \frac{K_I}{s} \qquad 3.36$$

Finally, in this control loop, the open loop transfer function is obtained and it is highly similar with the open loop transfer function of the force-feedback control loop, the only differences are the demodulation and the cancellation electrode structure explained in Chapter 2. Because of this similar transfer function, the controller design procedure will not be explained, and the controller design procedures for mode-matched and mismatched force feedback controller loop are used to design the controller parameters.

## 3.5 Mode Match Control Electronics and Controller Design for MEMS Gyroscope

The mode matching of a tuning for gyroscope highly improves the angular random walk (ARW) performance due to mechanical gain increase in the electronic noise limited systems. Figure 3.32 shows the block diagram of the gyroscope system including the mode-matching controller that matches the resonance frequencies by utilizing the phase difference relation between the residual AC quadrature and drive signals. This AC quadrature signal is produced by adding an extra AC signal to the quadrature controller output signals of Q+ and Q-. The chosen frequency of this AC perturbation signal is about 10 times of the quadrature error cancellation loop bandwidth and about 2 times of the force feedback controller loop bandwidth to decouple the perturbation signal from these loops effectively. After applying the perturbation signal to the mechanical system, this signal transferred to the sense peak electrodes according to the matching condition. The transferred signal firstly pre-amplified and demodulated with $f_{drive\_0}$ to take the signal from band-pass characteristics to low-pass characteristics. After that the demodulated signal is again demodulated with the perturbation signal to get the amplitude of the transferred perturbation signal representing the mismatch amount. This amplitude information is firstly low-pass filtered to eliminate the doubled frequency product of the demodulation and then fed to the mode-match controller input. This controller output generates a control signal ranges from -2.5V to +2.5V and then summed with initially set proof-mass voltage to tune the applied proof-mass voltage. This tuning process tunes the resonance frequency of the sense frame by changing the proof-mass voltage until the transferred perturbation signal nulled by changing the phase transfer function.

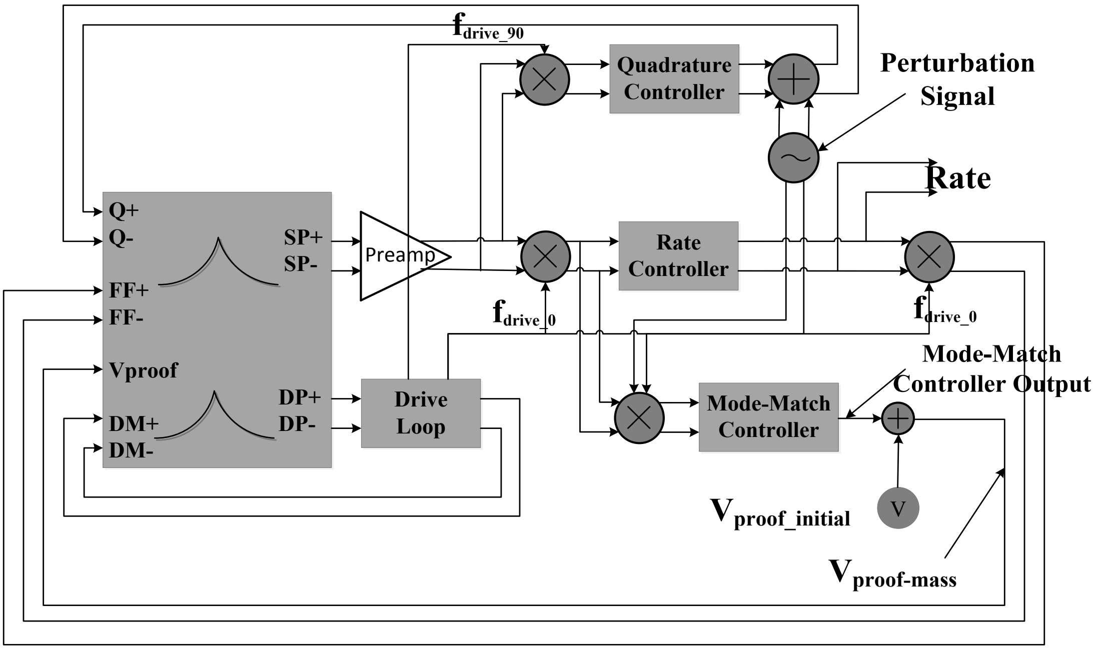

Figure 3.32: Block diagram of the proposed closed-loop controller system, including automatic mode-matching loop.

The controller in this mode-matching loop should be designed carefully, because the Q-factor of the sense-frame is very high to effectively control the mode-matching condition. Mode-matching can only be controlled by using a controller having good disturbance rejection capability. This controller performance requirement is provided by using $M_S$ constrained disturbance rejection controller design strategies developed in [10].

There are important design parameters that should be considered to ensure the reliable, robust, and stable operation while designing the control electronics and loop parameters. The generally defined parameters for a control loop are settling time, phase margin, gain margin, damping factor, overshoot and steady-state error. There are also some other design starting rules for different system. The main two control systems are set-point tracking and disturbance rejection systems. In our system, we firstly set the set point as 0 Hz frequency split and reject the disturbances in operation. So, our control design strategy should focus on disturbance rejection. Disturbance rejection systems generally have lower phase margin about 45° to damp the disturbances effectively and should not cancel any pole not to break the loop. When any pole cancelled in the mechanical system, any disturbance injected in the mechanical system is damped by only the damping of the mechanical system, because the effect of the pole is cancelled by the zero of electronics. By paying attention to the mentioned rules, open loop transfer function extraction can be started.

The model of the mode match includes applied AC quadrature signal to force, force to velocity, velocity to current, current to voltage, demodulation with in-phase signal, demodulation with applied AC signal, LPF, I controller to control $V_{proof}$. The transfer function of them can be written as in Equation 3.37, Equation 3.38, and Equation 3.39 respectively.

$$\frac{F(s)}{Vac_Q(s)} = n.\frac{4.\mathcal{E}.Vprof\,.X.h}{{x_0}^2}(s) \tag{3.37}$$

$$\frac{\mathrm{V(s)}}{\mathrm{F(s)}} = \frac{\mathrm{s}}{(\mathrm{m_{PM}} + \mathrm{m_S}).\mathrm{s}^2 + \mathrm{b.s} + \mathrm{k_S}} \tag{3.38}$$

$$\frac{I(s)}{\mathrm{V}(s)} = \frac{\partial C}{\partial x}.Vprof \tag{3.39}$$

The multiplication of the above equations with some changes gives the transconductance of the mechanical system as a voltage to current transfer function in Equation 3.40.

$$\frac{I(s)}{Vac_Q(s)} = \frac{\partial C}{\partial x}.Vprof.n.\frac{4.\mathcal{E}.Vprof\,.X.h}{{x_0}^2}.\frac{s}{(m_{PM} + m_S).s^2 + b.s + k_S} \tag{3.40}$$

The residual quadrature error force directly acts on the sense mode dynamic at the drive mode resonance frequency plus and minus frequency of applied AC quadrature signal ($\omega_q$) . Therefore, under the condition of the frequency mismatch between the resonance modes. transfer function from AC quadrature signal to current output of the sense pick electrodes modulated with in-phase drive pick signal can be defined as in Equation 3.41derived in [24].

$$\frac{I_{SP}(s)}{Vac_Q(s)} = \frac{\partial C_{SP}}{\partial x}.n.\frac{4.\varepsilon.Vprof.X.h}{x_0^2}.Vprof.\frac{1}{4}$$

$$\frac{(\omega_S-\omega_D)-\frac{\omega_D}{8.Q_s^2}}{(m_{PM}+m_S).(s^2+\frac{\omega_S}{Q_S}.s+(\omega_S-\omega_D)^2+\left(\frac{\omega_S}{2.Q_S}\right)^2)} \tag{3.41}$$

The in-phase demodulated signal in Equation 3.41 is demodulated again with the applied AC quadrature signal to detect the resonance frequency difference between drive and sense modes. Finally, the resonance frequency difference is detected and defined as in Equation 3.42. The response of the Equation 3.34 can be seen at Figure 3.33.

$$I_{SP}(s) = \frac{\partial C_{SP}}{\partial x}.n.\frac{4.\varepsilon.Vprof.X.h}{x_0^2}.Vprof.\frac{1}{4}$$

$$\left[\frac{(\omega_S-\omega_D)-\frac{\omega_D}{8.Q_s^2}}{4.(m_{PM}+m_S).((s-j.\omega_q)^2+\frac{\omega_S}{Q_S}.(s-j.\omega_q)+(\omega_S-\omega_D)^2+\left(\frac{\omega_S}{2.Q_S}\right)^2)}\right] \tag{3.42}$$

$$+\left[\frac{(\omega_S-\omega_D)-\frac{\omega_D}{8.Q_s^2}}{4.(m_{PM}+m_S).((s+j.\omega_q)^2+\frac{\omega_S}{Q_S}.(s+j.\omega_q)+(\omega_S-\omega_D)^2+\left(\frac{\omega_S}{2.Q_S}\right)^2)}\right]$$

The phase detection output with respect to $(\omega_S-\omega_D)$ can be found by applying s as 0. Then, the $(\omega_S-\omega_D)$ relation is obtained as in Equation.3.43 The graph of the Equation 3.43can be seen at Figure 3.34.

$$I_{SP}(s) = \frac{\partial C_{SP}}{\partial x}.n.\frac{4.\varepsilon.Vprof.X.h}{x_0^2}.Vprof.\frac{1}{8.(m_{PM}+m_S)}.$$

$$\left[\frac{\left((\omega_S-\omega_D)-\frac{\omega_D}{8.Q_s^2}\right)}{(-\omega_q^2+(\omega_S-\omega_D)^2+\left(\frac{\omega_S}{2.Q_S}\right)^2)}\right] \tag{3.43}$$

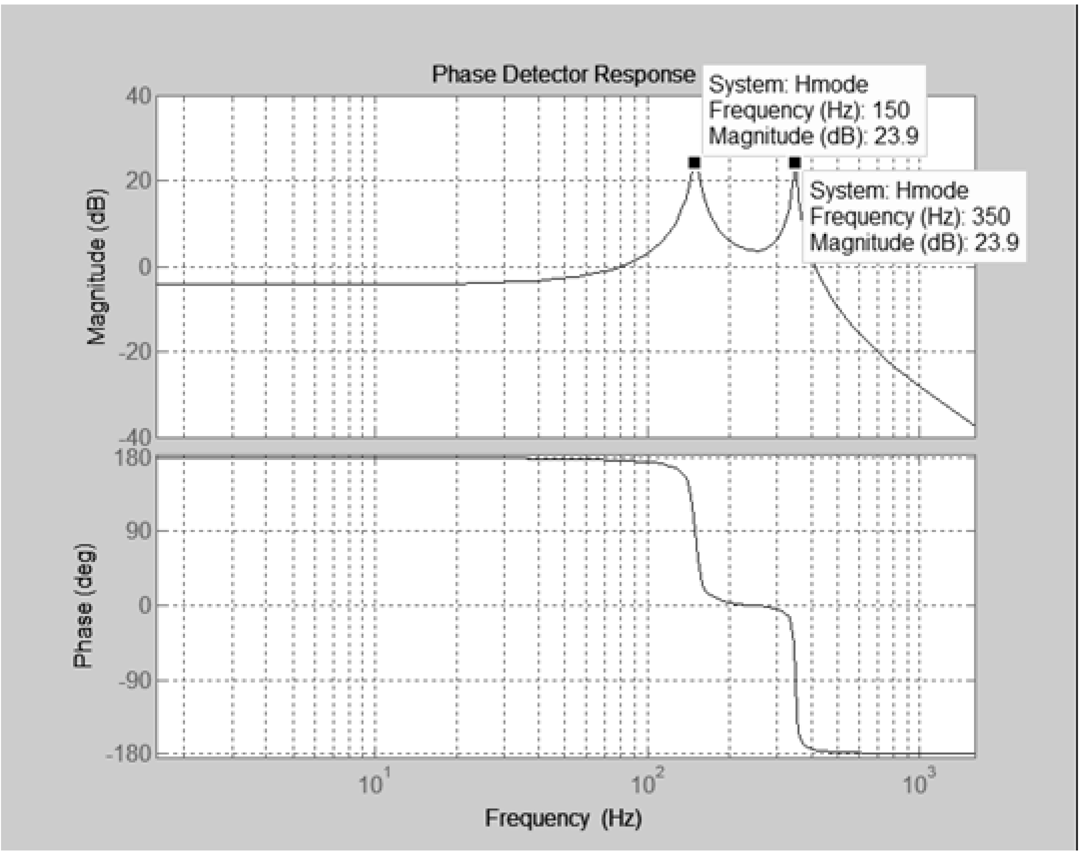

Figure 3.33: The phase detector response. The system parameters: $f_q$=250Hz, $f_S - f_D$= 100Hz, Q=1000, the peak frequencies: $f_q - f_S + f_D$=150Hz, $f_q + f_S - f_D$=350Hz.

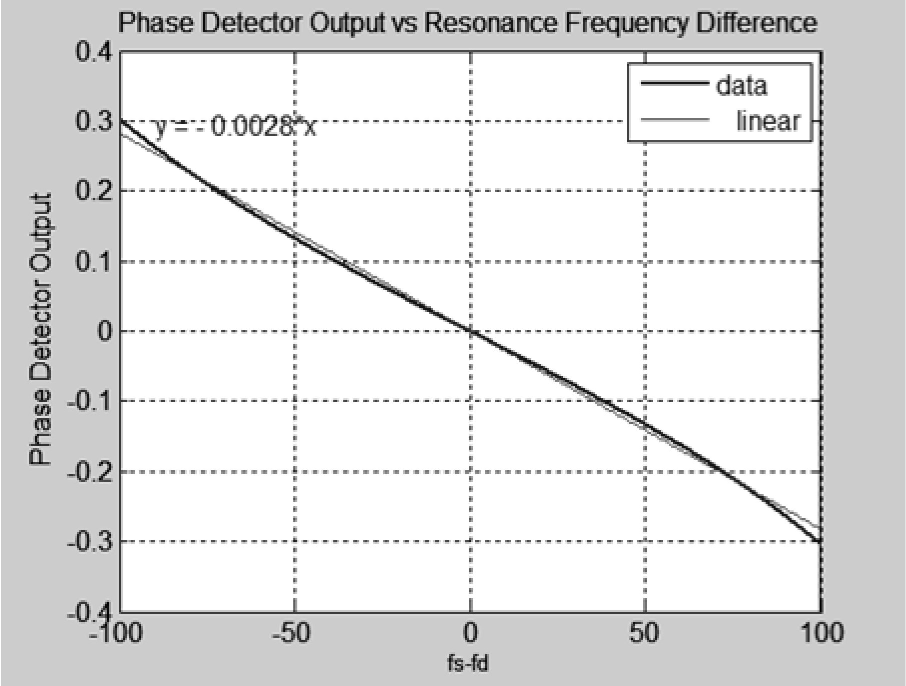

Figure 3.34: The phase detector output with respect to resonance frequency difference from -100Hz to 100Hz.

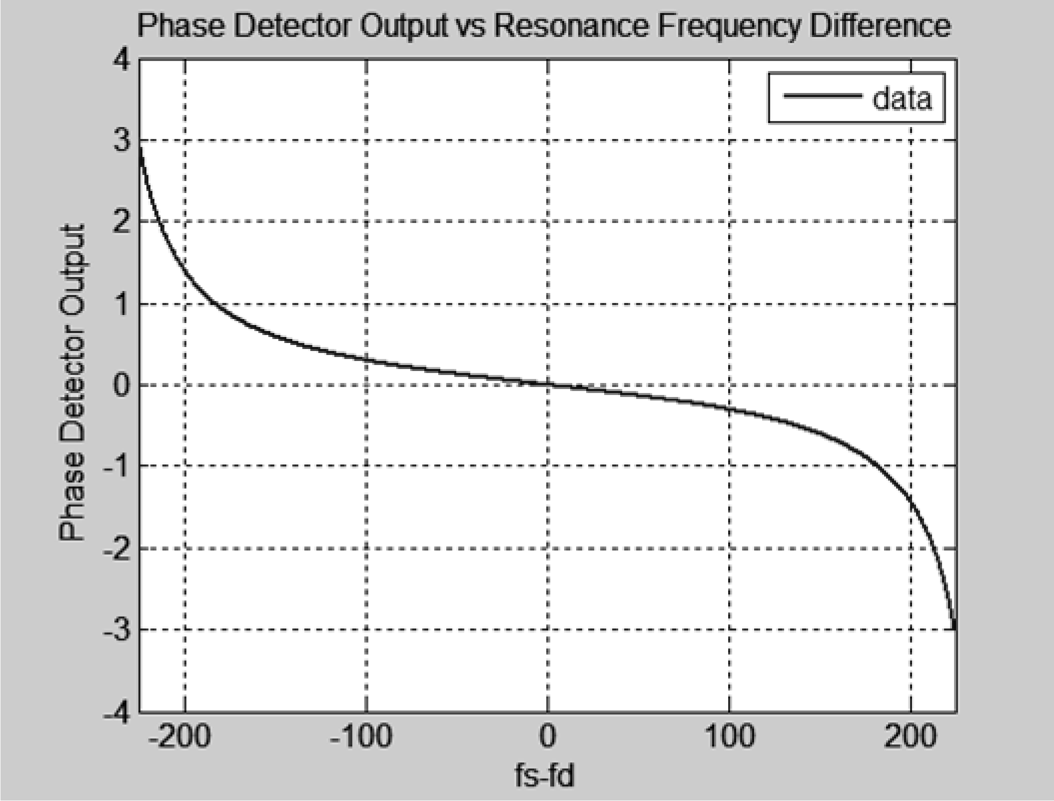

Figure 3.35: The phase detector output with respect to resonance frequency difference from -225Hz to 225Hz.

The mode-matching system design can be continued with the controller design procedures, after the open loop transfer function is obtained. The procedures should be defined while paying more attention to the parameter change of $\omega_S - \omega_D$ during mismatch to mode-match condition. When the $\omega_S - \omega_D$ changes, the peak frequencies and the gain of the transfer function change. However, this problem can be solved by choosing the worst case for the system while designing controller. For these systems, integral controller is generally stable with lower gains, because of that controller should be designed for the highest gain and resonance frequency difference. Therefore, the worst case can be defined as the highest resonance frequency difference with a highest gain, because gain increases with resonance frequency difference. However, when we choose the mode-matching system range as the half of the applied AC quadrature signal frequency, the system's gain is constant as in Figure 3.34 in contrast to the Figure 3.35 having higher range. After linearizing the gain, highest resonance frequency difference is chosen as 100Hz having a transfer function shown in Figure 3.33 having 2 peak frequencies.

The closed loop controller parameter design with the defined system parameters can be continued with the LPF and I controller parameters. In a mode-match system 1Hz bandwidth is fairly enough to match the system, and the other parameters will be designed for this design chooses. However, the closed loop bandwidth can also be increased to about 100Hz at the cost of increased feedback noise. With a 1Hz closed loop bandwidth requirement, 3-pole LPF cut of frequency and phase margin is designed as 4Hz and 60° respectively. Finally, the open loop transfer of the loop having 3-pole LPF and integral controller response and the closed loop transfer functions can be seen at Figure 3.36 and Figure 3.37 respectively.

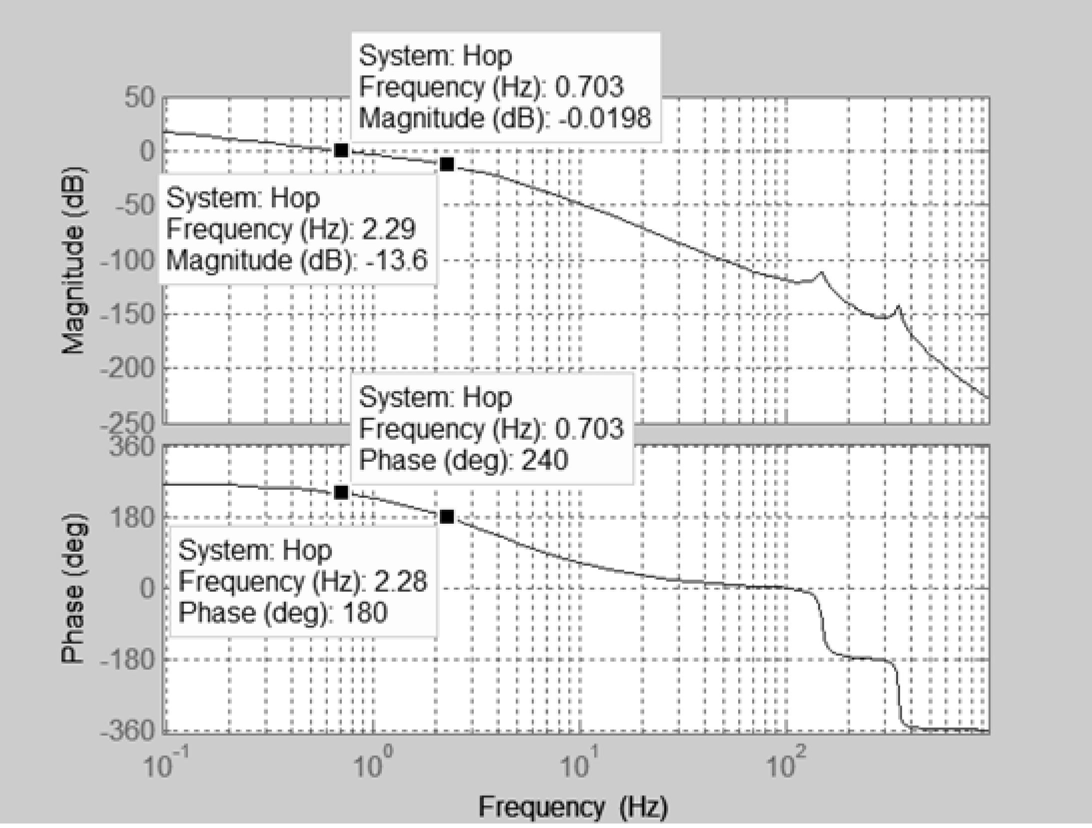

Figure 3.36: The open loop transfer function of the mode-match loop. Phase margin: 60° at 0.7Hz; gain margin:13.6dB at 2.3Hz.

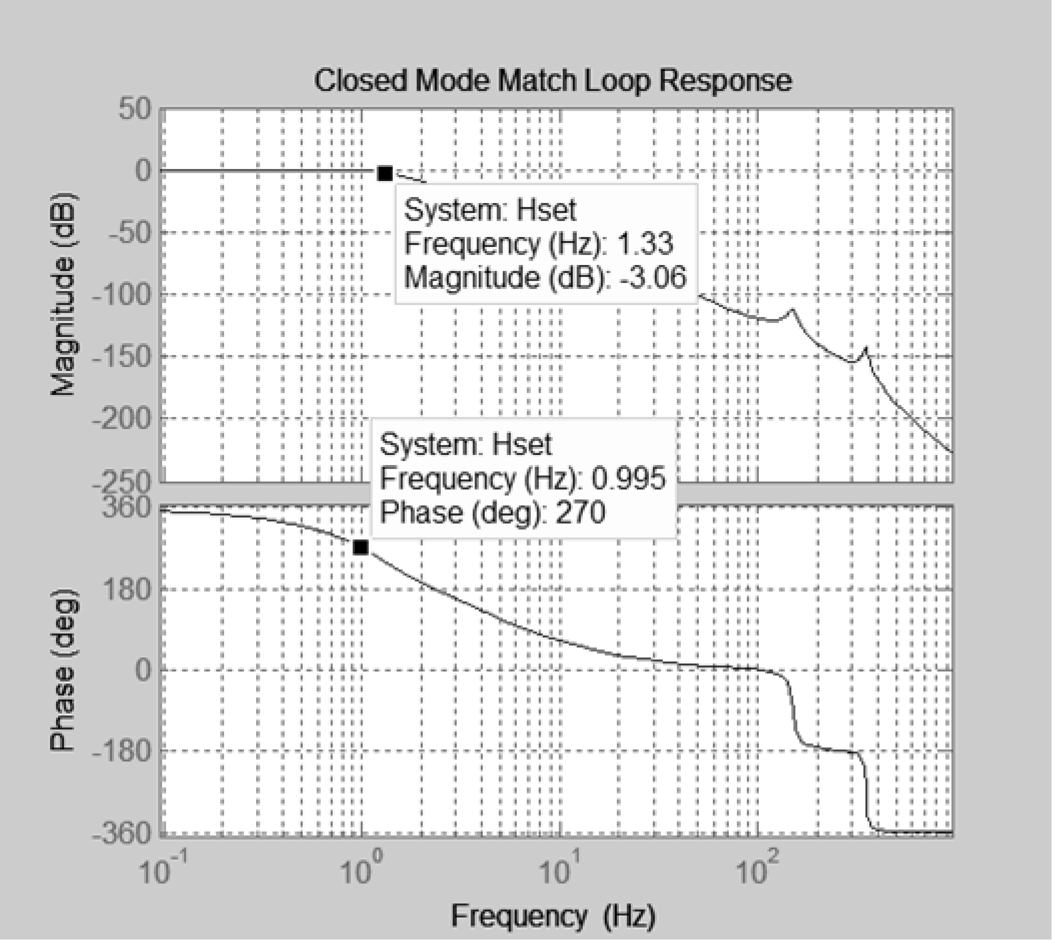

Figure 3.37: The closed loop transfer function of the mode-match loop. -3dB bandwidth:1.33Hz; 90° phase shift bandwidth:1Hz.

## 3.6 Performance Analysis

In general, practical electronic systems have error sources related to the external and internal effects such as temperature and noise.

In a MEMS gyroscope, there are three main error sources. The first one is angular random walk, related with the white noise sources of the thermo-mechanical-noise and white electronics noise. The typical unit of this error source is °/√h meaning that the output has a standard deviation of the orientation error after 1 hour. The second error source is the flicker noise caused by the flicker noises of the DC processing blocks. This noise source changes the bias and leads bias instability measured as °/hr indicating the change in bias over a specified period of time. The final main error source is the offset of the gyroscope output related to the offset voltages of electronics and quadrature signal.

In a inertial navigation systems, performance of a sensor is analyzed by using the Allan variance analysis. The Allan variance provides a means of identifying and quantifying various noise terms that exist in the data as in Figure 3.38.

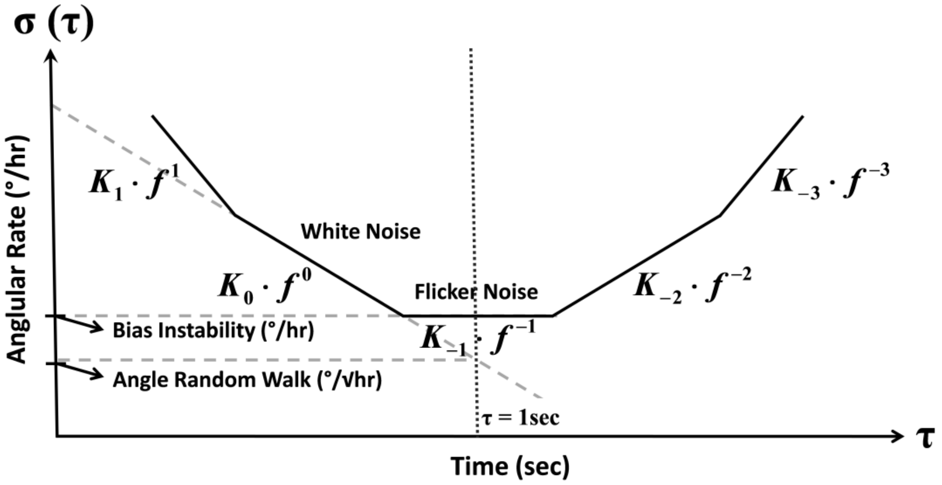

Figure 3.38: Allan variance plot.

The relations between the white noise density and the angle random walk (ARW); the Flicker noise constant and the bias instability (BI) can be expressed in the following equations:

$$\text{ARW} = \text{White Noise Density}.\sqrt{0.5} \tag{3.44}$$

$$\text{BI} = \text{Flicker Noise Density Constant}.\sqrt{2}.\sqrt{\ln{(2)}} \tag{3.45}$$

The noise calculations of the MEMS gyroscope will be done by gathering all the noise sources at the preamplifier input as a current. After that, we can easily calculate the ARW and bias instability of the gyroscope for the mismatched and mismatched case.

The first error source is the thermo-mechanical Brownian noise produced by Brownian motions of air molecules and expressed as in Equation 3.46.

$$F_B = \sqrt{4.k_B.T.b}.\frac{N}{\sqrt{Hz}} \qquad 3.46$$

This force equation can also be expressed as in Equation 3.47.

$$F_B = \sqrt{4.k_B.T.\frac{(m_{PM} + m_S).\omega_S}{Q_s}}.\frac{N}{\sqrt{Hz}} \qquad 3.47$$

Rate equivalent Brownian noise can be calculated by dividing the Brownian force to Coriolis force as in Equation 3.48

$$\Omega_{rate} = \frac{\sqrt{4.k_B.T.\frac{(m_{PM} + m_S).\omega_S}{Q_s}}}{2.m_{PM}.\Omega.\omega_D.X_D} \qquad 3.48$$

The Equation 3.48 is in the radian, but in the degree is more generally used in convention, so this equation is modified as degree based as in Equation 3.49.

$$\Omega_{rate} = \frac{180}{\pi.X_D}\frac{\sqrt{k_B.T.\frac{(m_{PM} + m_S).\omega_S}{Q_s}}}{m_{PM}.\omega_D} \qquad 3.49$$

After the calculation of the rate equivalent Brownian noise, that should be converted to current noise generated at the input of the preamplifier as in Equation 3.50.

$$I_{Brownian}(s) = \frac{\partial C_{SP}}{\partial x}.Vprof.\frac{1}{4}$$

$$\frac{(\omega_S - \omega_D) - \frac{\omega_D}{8.{Q_s}^2}}{(m_{PM} + m_S).(s^2 + \frac{\omega_S}{Q_S}.s + (\omega_S - \omega_D)^2 + \left(\frac{\omega_S}{2.Q_S}\right)^2)}.\sqrt{4.k_B.T.\frac{(m_{PM} + m_S).\omega_S}{Q_s}} \qquad 3.50$$

However, there are also two noise sources created by the electronics, these are white and flicker noises. The calculations of the will not be made in this section. The detailed calculations can be found in [20]. Finally, these error sources should be compared with current at input of the preamplifier generated by Coriolis force as in Equation 3.51 to find the rate equivalent noise performance.

$$I_{Coriolis}(s) = \frac{\partial C_{SP}}{\partial x}.Vprof.\frac{1}{4}$$

$$\frac{(\omega_S - \omega_D) - \frac{\omega_D}{8.Q_s{}^2}}{(m_{PM} + m_S).(s^2 + \frac{\omega_S}{Q_S}.s + (\omega_S - \omega_D)^2 + \left(\frac{\omega_S}{2.Q_S}\right)^2)}.(2.m_{PM}.\Omega.\omega_D.X_D) \qquad 3.51$$

At final, the noise performance of the gyroscopes implemented with the designed CMOS electronics for the mismatched MG1 and MG3 types MEMS gyroscopes and for the mode matched MG3 gyroscope will be calculated.

The first performance calculation will be done for the system implemented with CMOS and MG1 in mismatched condition. The $I_{Brownian}$ and $I_{Coriolis}$ are calculated by using Equation 3.50 and Equation 3.51 respectively. The results are summarized in

Table 3.4.

Table 3.4: The noise sources at the input of the preamplifier when the system is implemented with the CMOS and MG1 MEMS gyroscope in Mismatched condition.

| Noise Type | Current Noise Density | Values |
|---|---|---|
| Brownian Noise | $I_{Brownian}$ | 0.0105pA/√Hz |
| 1°/hr Coriolis Generated Current | $I_{Coriolis}$ | 0.0062pA/√Hz |
| White Electronics Noise | $I_{White}$ | 0.0256pA/√Hz |
| Flicker Electronics noise | $I_{1/f}$ | 0.0052 pA/√f |

Table 3.5: The performance result of the gyroscope implemented with the CMOS and MG1 MEMS gyroscope in Mismatched condition.

| Current Noise Density | Values | Rate Equivalent | Allan Deviations |
|---|---|---|---|
| $I_{Total\_White}$ | 0.0277pA/√Hz | 4.47°/hr/√Hz | ARW=3.13°/hr/√Hz |
| $I_{Total\_1/f}$ | 0.0052pA/√f | 0.84°/hr | BI=1.00/hr |

The performance results of this gyroscope can be summarized in Table 3.5 including ARW and BI. The second performance calculation will be done for the system implemented with the CMOS and MG3 in mismatched condition. The $I_{Brownian}$ and $I_{Coriolis}$ are calculated by using Equation 3.50 and Equation 3.51 respectively. The results are summarized in Table 3.6.

Table 3.6: The noise sources at the input of the preamplifier when the system is implemented with the CMOS and MG3 MEMS gyroscope in Mismatched condition.

| Noise Type | Current Noise Density | Values |
|---|---|---|
| Brownian Noise | $I_{Brownian}$ | 0.0032pA/√Hz |
| 1°/hr Coriolis Generated Current | $I_{Coriolis}$ | 0.0103pA/√Hz |
| White Electronics Noise | $I_{White}$ | 0.0262pA/√Hz |
| Flicker Electronics noise | $I_{1/f}$ | 0.0113 pA/√f |

Table 3.7: The performance result of the gyroscope implemented with the CMOS and MG3 MEMS gyroscope in Mismatched condition.

| Current Noise Density | Values | Rate Equivalent | Allan Deviations |
|---|---|---|---|
| $I_{Total\_White}$ | 0.0270pA/√Hz | 2.62°/hr/√Hz | ARW=1.84°/hr/√Hz |
| $I_{Total\_1/f}$ | 0.0113pA/√f | 1.09°/hr | BI=1.28/hr |

The performance results of this gyroscope can be summarized in Table 3.7 including ARW and BI. The final performance calculation will be done for the system implemented with the CMOS and MG3 in mode-matched condition. The $I_{Brownian}$ and $I_{Coriolis}$ are calculated by using Equation 3.52 and Equation 3.53 respectively. The results are summarized in Table 3.8.

$$I_{Brownian}(s) = \frac{\partial C_{SP}}{\partial x}.\mathrm{Vprof}.\frac{1}{4} \frac{s + \frac{\omega_S}{2.Q_s}}{(m_{PM} + m_S).(s^2 + \frac{\omega_S}{Q_S}.s + (\omega_S - \omega_D)^2 + \left(\frac{\omega_S}{2.Q_S}\right)^2)}.\sqrt{4.k_B.T.\frac{(m_{PM} + m_S).\omega_S}{Q_s}} \qquad 3.52$$

$$I_{Coriolis}(s) = \frac{\partial C_{SP}}{\partial x}.\mathrm{Vprof}.\frac{1}{4} \frac{s + \frac{\omega_S}{2.Q_s}}{(m_{PM} + m_S).(s^2 + \frac{\omega_S}{Q_S}.s + (\omega_S - \omega_D)^2 + \left(\frac{\omega_S}{2.Q_S}\right)^2)}.(2.m_{PM}.\Omega.\omega_D.X_D) \qquad 3.53$$

Table 3.8: The noise sources at the input of the preamplifier when the system is implemented with the CMOS and MG3 MEMS gyroscope in mode matched condition.

| Noise Type | Current Noise Density | Values |
|---|---|---|
| Brownian Noise | $I_{Brownian}$ | 1.7200pA/√Hz |
| 1°/hr Coriolis Generated Current | $I_{Coriolis}$ | 5.4500pA/√Hz |
| White Electronics Noise | $I_{White}$ | 0.0262pA/√Hz |
| Flicker Electronics noise | $I_{1/f}$ | 0.0113 pA/√f |

Table 3.9: The performance result of the gyroscope implemented with the CMOS and MG3 MEMS gyroscope in mode matched condition.

| Current Noise Density | Values | Rate Equivalent | Allan Deviations |
|---|---|---|---|
| $I_{Total\_White}$ | 1.7200pA/√Hz | 0.32°/hr/√Hz | ARW=0.23°/hr/√Hz |
| $I_{Total\_1/f}$ | 0.0113pA/√f | 0.002°/hr | BI=0.0024°/hr |

The performance results of this gyroscope can be summarized in Table 3.9 including ARW and BI. Finally, it is shown that, mode-matching of an electronics noise limited gyroscope system highly improves the ARW and BI performance results as expected.

# CHAPTER 4

# TEST RESULT

This chapter presents the test results of the tuning fork MEMS gyroscope. Section 4.1 explains resonance characterization for tuning fork MEMS gyroscope, and Section 4.2 describes the system level test setup and method for mismatched and mode-matched MEMS gyroscopes. Next, the tests results of drive mode controller are provided in Section 4.3. Section 4.4 demonstrates the mode-match controller test results with externally created frequency mismatch. Following, Section 4.5 presents performance test results of mode-matched and mismatched MG3 MEMS gyroscope with CMOS readout circuit. Next, performance test results of mismatched MG1 MEMS gyroscope with the CMOS readout circuit are provided in Section 4.6. Finally, Section 4.7 gives a summary of this chapter.

## 4.1 Resonance Characterization for Tuning Fork MEMS Gyroscope

The fabricated wafer level vacuum packaged MEMS gyroscopes are tested with the resonance characterization setup as shown in Figure 4.1. This setup includes some special probes controlled by probe station as in Figure 4.2 to get contact from the electrodes. The device under test is excited with a dynamic signal analyzer and the generated output current is converted to voltage with a test circuit as shown in Figure 4.3. The output voltage is fed to the dynamic signal analyzer to get the gain and phase characteristics of the MEMS gyroscope. The main purpose of this setup is to extract the resonance frequencies and the Q-factors of the drive and sense modes of the MEMS gyroscope with the obtained gain and phase characteristics. Because, obtained information is used to design the control loops and calculate the noise and bias performances.

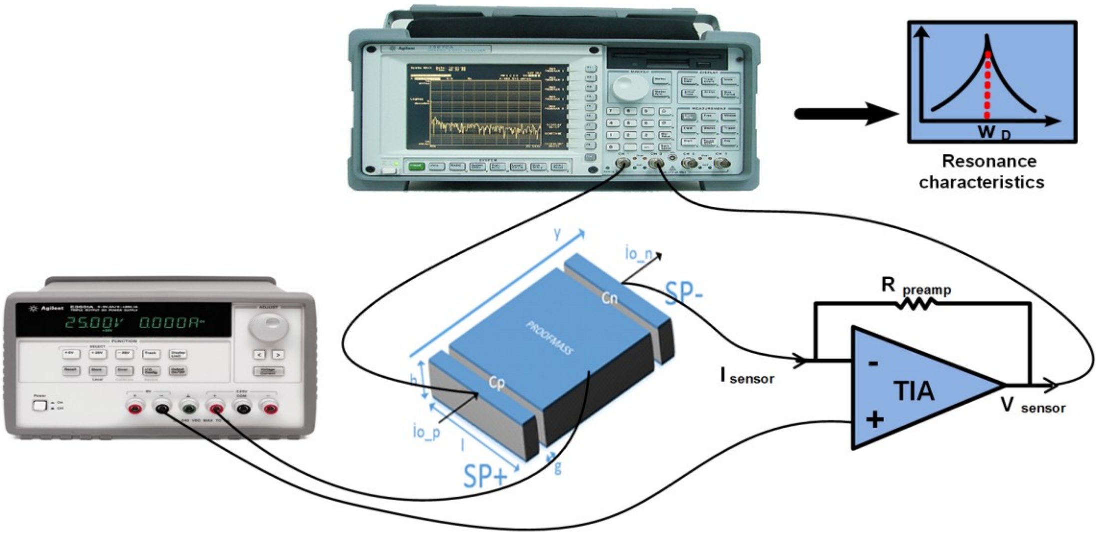

Figure 4.1: The resonance characterization setup

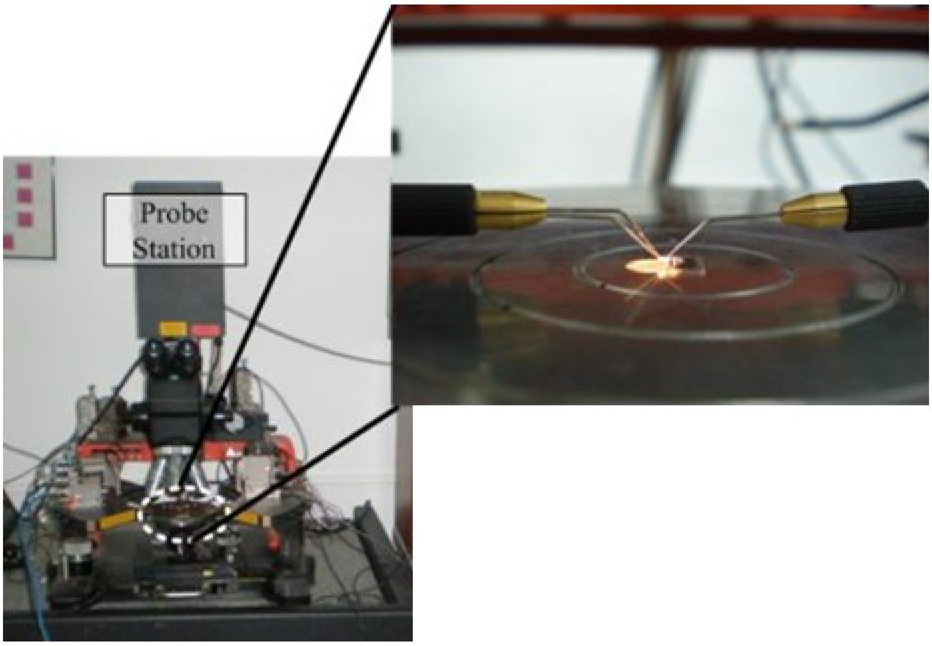

Figure 4.2: Special probes with probe station.

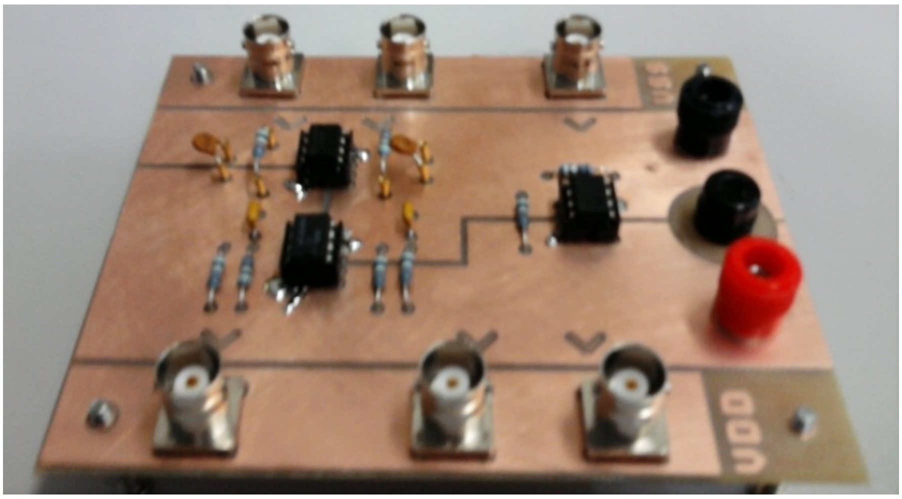

Figure 4.3: The resonance test circuit.

The resonance test of the MG1 and MG3 gyroscopes were done with the mentioned setup. The characterization results of the some MG1 and MG3 gyroscopes can be seen at Table 4.1. Moreover, the resonance characteristic of the sense mode the MG3 MEMS gyroscope (0304) can be seen at Figure 4.4.

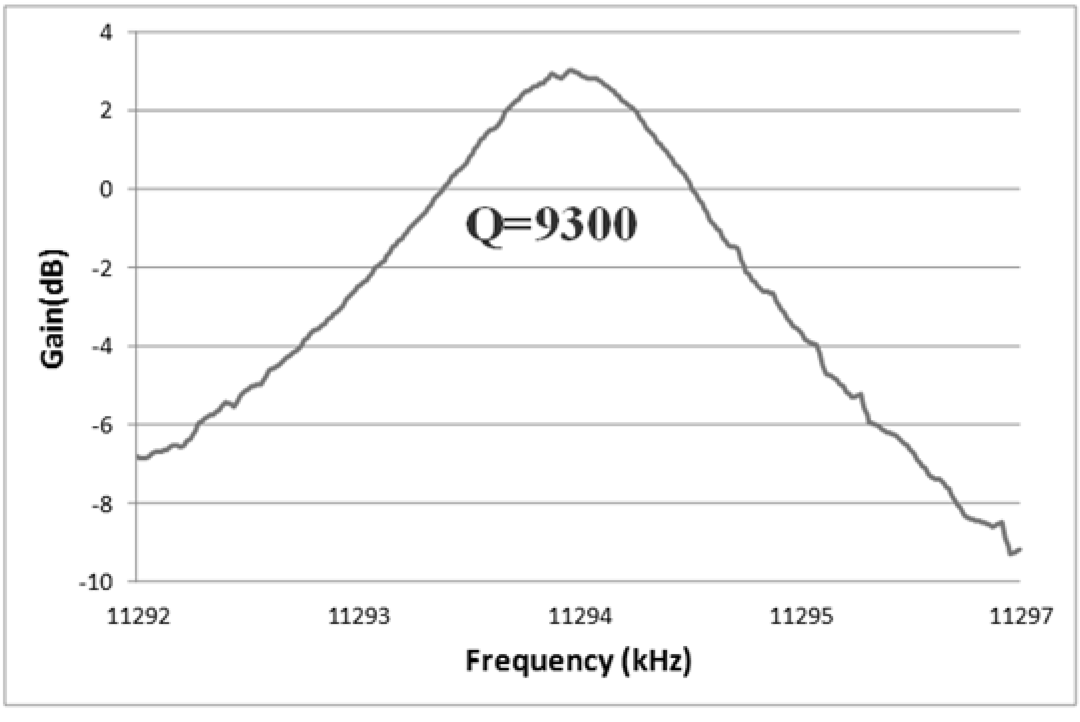

Figure 4.4: Sense mode resonance characteristics of the tested(0304) vacuum packaged gyroscope having 9350 Q-factor with 12.2V proof mass voltage.

Table 4.1: The characterization results of the MG1 and MG3 gyroscopes.

| **MODEL** | **SENSOR NO** | **DRIVE MODE** | | | **SENSE MODE** | | |
|---|---|---|---|---|---|---|---|
| | | **Freq(Hz)** | **Gain (dB)** | **Q-Factor** | **Freq (Hz)** | **Gain (dB)** | **Q-Factor** |
| MG1 | 67 | 11733 | 19.75 | 132899 | 12212 | 0.4 | 3889 |
| MG1 | 70 | 11459 | 19.46 | 128535 | 11918 | 0.9 | 4105 |
| MG1 | 71 | 11524 | 18.65 | 117091 | 11978 | -4.4 | 2248 |
| MG1 | 81 | 12014 | 20.74 | 148944 | 12423 | 1.2 | 4250 |
| MG3 | 1304 | 11589 | 6.09 | 21800 | 11587 | -8.0 | 2848 |
| MG3 | 0702 | 11120 | 13.4 | 50500 | 11192 | 1.73 | 8540 |
| MG3 | 1013 | 11142 | 8.09 | 27850 | 11081 | -0.86 | 6570 |
| MG3 | 0304 | 11251 | 3.20 | 15560 | 11273 | 2.16 | 9300 |

At the design stage of the MG3 gyroscope, the resonance mode frequencies of the drive and sense modes of the gyroscope are designed to be matched including spring softening effect of the sense pick electrodes. However, the manufacturing process has some imperfections leading a frequency difference between drive and sense mode resonance frequencies as in Table 4.1.

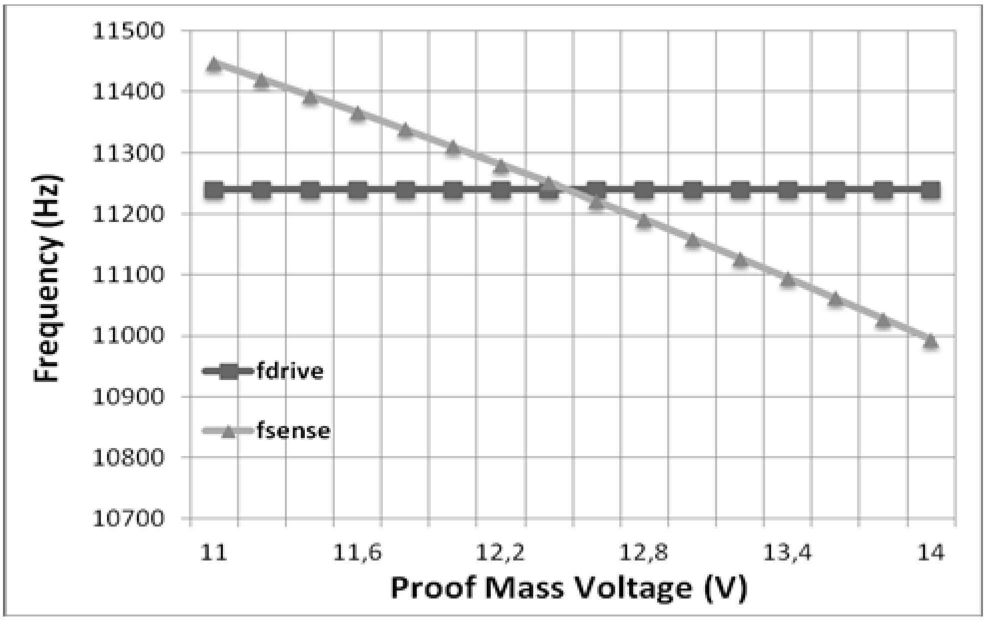

Figure 4.5: Drive and sense mode resonance frequency characteristics of the MG3 MEMS gyroscope (0304) with respect to proof mass potential.

In this thesis, the mode-matching is successfully accomplished tuning the sense mode resonance frequency with respect to the drive mode resonance frequency by changing the proof mass potential from 11V to 14V. The range of proof mass voltage decides the frequency tuning range of the mode-matching system. Figure 4.5 shows the drive and sense mode resonance frequency characteristics of the MG3 MEMS gyroscope (0340) with respect to the changing proof mass potential from 11V to 14V. The drive mode resonance frequency of the MEMS gyroscope remains constant at 11250 Hz, whereas the sense mode frequency of the gyroscope can be electronically tuned through the sense electrodes in the range from 11450Hz to 10980 Hz. The resonance mode frequencies are perfectly matched at the proof mass potential of 12.50V.

## 4.2 System Level Test Setup and Method for Mismatched and Mode-matched MEMS Gyroscopes

The testing of MEMS gyroscope starts with functional tests. At first, manufactured gyroscope system with readout circuitries' power dissipation and the oscillation at drive control loop should be tested and compared with the designed values. After verifying the functionality test, two main tests of the MEMS gyroscope are done. These are scale factor and noise tests. Extra to these tests some other repeatability and environmental test are conducted.

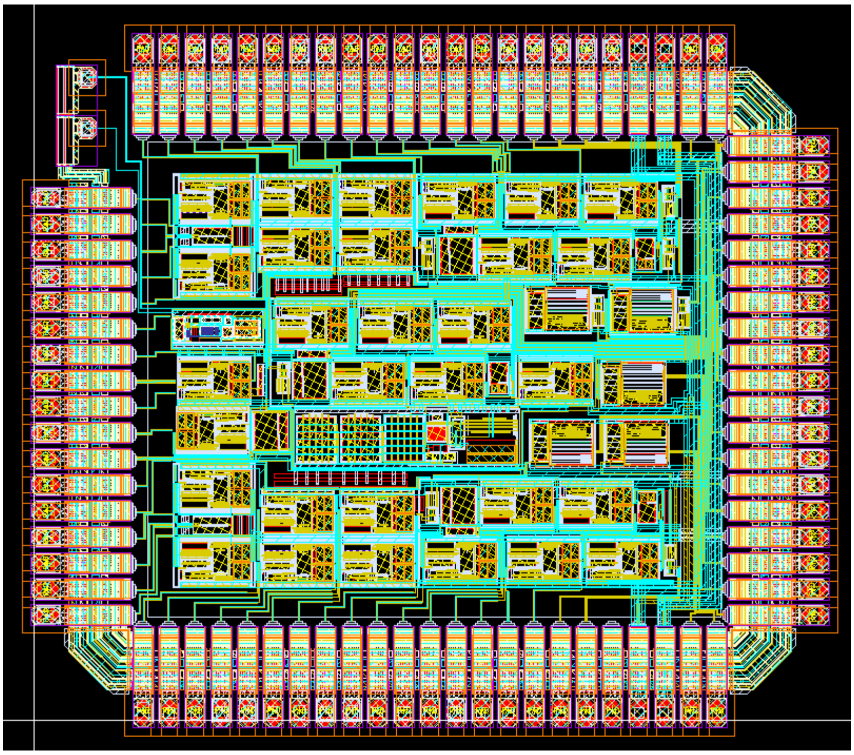

Figure 4.6: The layout of the MEMS gyroscope CMOS readout circuitry including analog signal conditioning, drive, sense, quadrature cancellation, mode-matching, and temperature sensing circuits.

The control and analog signal conditioning circuits are implemented with the CMOS electronics. This CMOS readout circuit has the drive, sense, quadrature cancellation, and mode-matching circuit in one die as shown in Figure 4.6. This CMOS readout circuit is implemented with MG3 MEMS gyroscope having capability of mode-matching as in Figure 4.7. This implementation is accomplished only within the 22mm x 22mm metal package with some passive components and has configuration option for the mode-matched and mismatched operation.

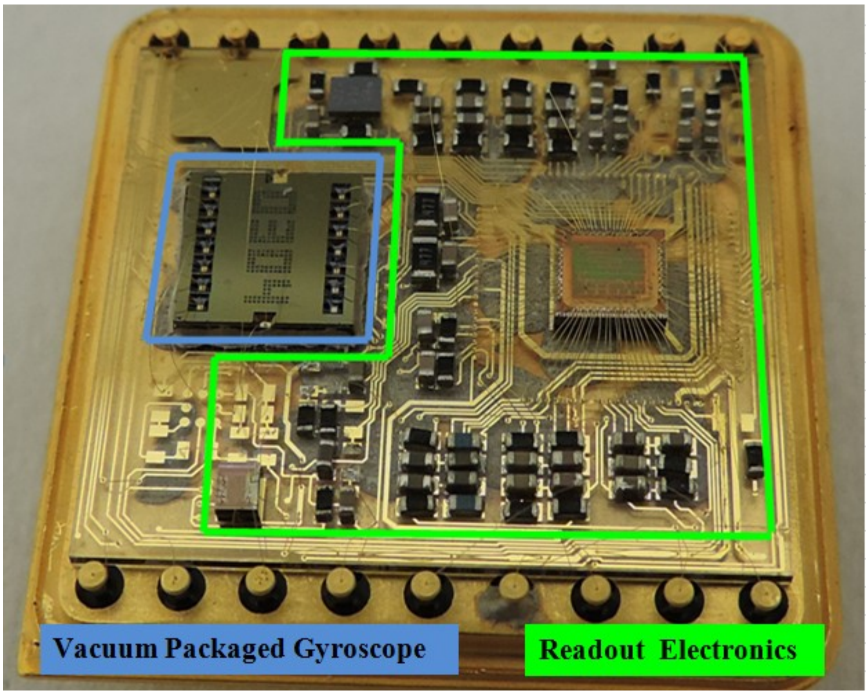

Figure 4.7: The implemented gyroscope with vacuum packaged MG3 and the CMOS readout circuit in a 22mm by 22mm metal package. This sensor has capability of two operation condition of mode-matched and mismatched.

This CMOS readout is also implemented with MG1 sensor having 2 proof masses but does not have mode-matching capability due to separate sense resonance frequencies. In this implementation, MEMS gyroscope is operated in mismatched condition and obtained very good results. Extra to these implementations, the same circuit architecture is implemented with discrete components in the same package area with the previously mentioned implementations, but in this case, circuits implemented as 2 floors as in Figure 4.8. This implementation has some difficulties related to manufacturing and repeatability issues.

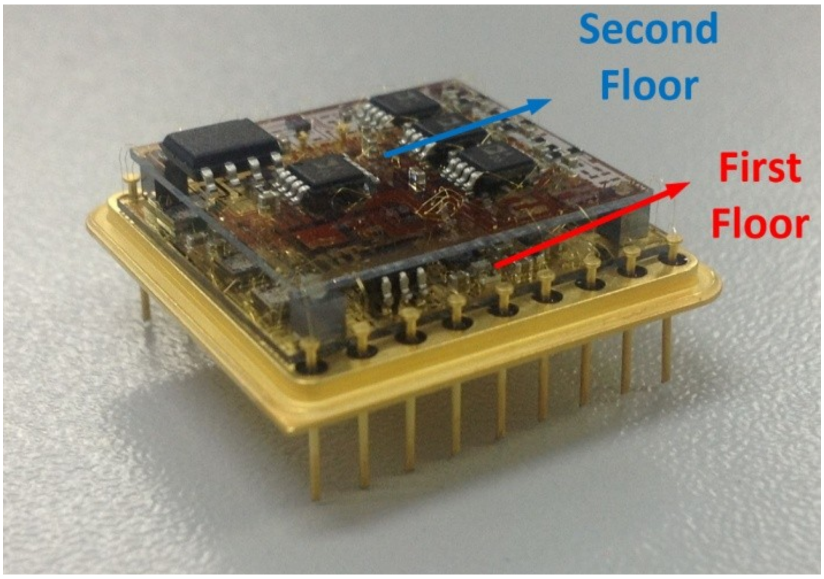

Figure 4.8: The implemented gyroscope with vacuum packaged MG1 and the discrete readout circuit in a 22mm by 22mm metal package as two floors.

Figure 4.9 shows the system test setup. Test setup is composed of a voltage supply, an oscilloscope, a rate table, and a data acquisition (DAQ) card. The supply is necessary to set the proof mass voltage and the DC supplies of the system, the required set-point voltages of the system are generated in the CMOS readout circuit. The scale factor tests are performed with the rate table to measure the linearity, responsivity, and scale factor repeatability. The rate table is controlled by a computer for different rate conditions. This computer is also used to acquire the analog rate information by using a DAQ.

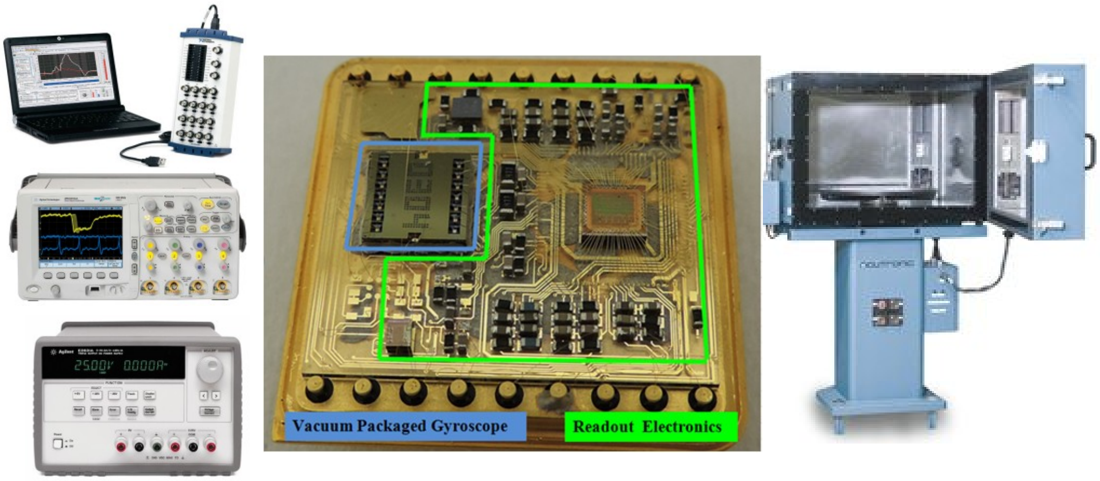

Figure 4.9: The system test setup including DAQ, oscilloscope, power supply, the gyroscope sensor as a device under test (DUT), and rate table.

## 4.3 Drive Mode Controller Test Results

The previously designed drive mode controller loops at the previous studies has been designed again to satisfy robust control over amplitude of the drive displacements without need to know exact Q-factor of the drive mode. That was done by modeling the mechanical transfer function as an integrating process due to high Q-factor. As a rule of thumb, when the desired bandwidth is higher than the 10 times of the controlled process, modeling can be done as an integrating process.

After manufacturing the MEMS gyroscope sensor with MG1 gyroscope and CMOS readout circuit, drive mode settling characteristics is tested. In this test, system is powered up, and then set point voltage of the system is changed from 0 to designed value to observe the settling characteristics of the control loop by excluding the power supply settling characteristics. The result of the test is highly consistent with the simulation results conducted on SPICE program as in Figure 4.10 and Figure 4.11.

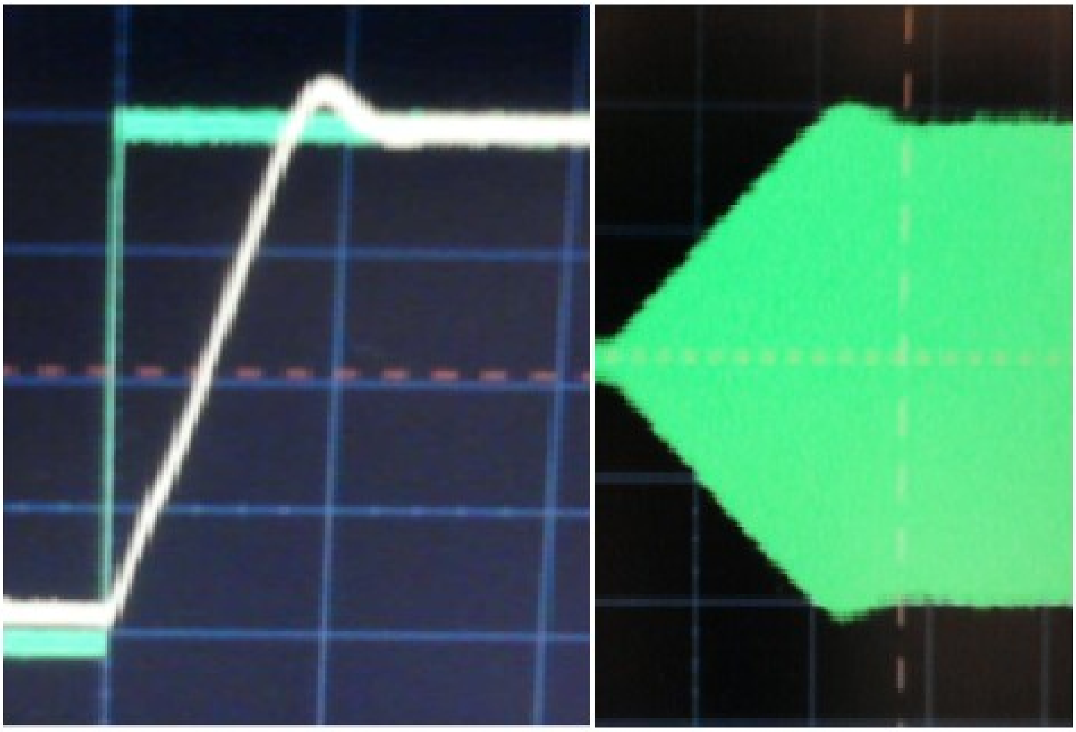

Figure 4.10: The settling characteristic test of the designed drive control loop implemented with CMOS readout circuit and MG1 gyroscope by observing the preamplifier output of the drive loop. Q_Factor:117,000, Settling in %1 error band: 125msec, Overshoot: %6.

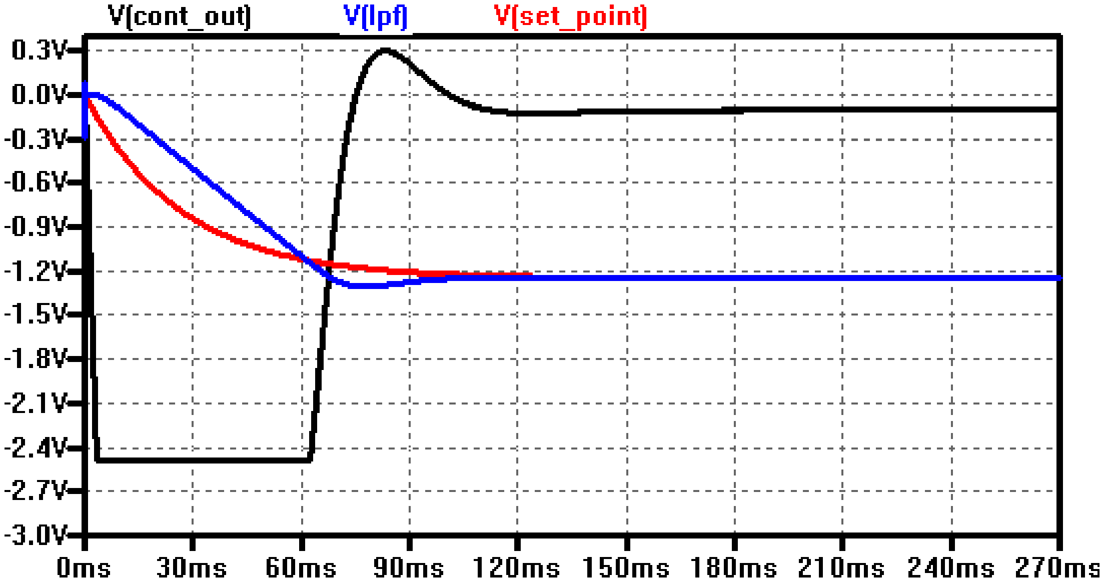

Figure 4.11: The settling characteristic of the designed drive control loop implemented in LTSpice. Q_Factor:50,000, Settling in %0.1 error band: 163msec, Settling in %1 error band: 120msec. Overshoot: %4. Black: PI controller output, Blue: Low pass filter output showing the displacement, Red: Set-point voltage applied with the set-point weighting function.

## 4.4 Mode-Match Controller Test Results

The mode-match controller mainly controls the proof mass voltage of the system to tune the resonance frequency of the sense mode by the help of softening effect of the varying gap sense pick electrodes. This can also be said differently, when the proof mass voltage is changed from the steady state value for the mode-matched case, an artificial frequency mismatch can be created as an environmental effect. Because of that the functionality tests of the mode-matching controller system are conducted by changing the initial proof mass voltage sharply. After this change in the proof mass voltage, mode-match controller effectively matches the modes by setting the applied proof mass voltage to the matched state voltage again as shown in Figure 4.12. This experiment also shows that the disturbance rejection performance of the control loop has a very low settling time about 2 sec compared to other studies in the literature [1].

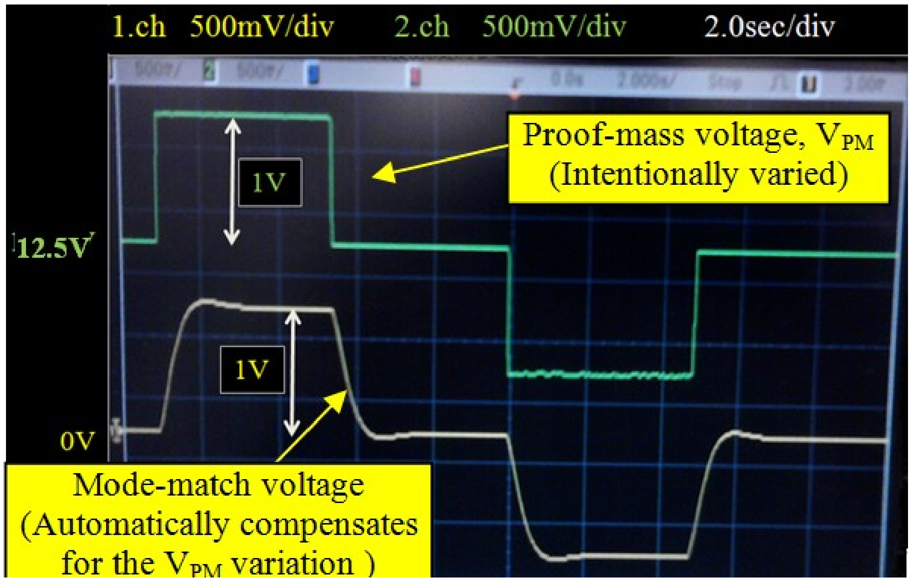

Figure 4.12: Experimental verification of the automatic mode-matching system. The tuning voltage generated by the mode-match controller continuously tracks the intentional variations in the proof mass voltage to keep the frequencies matched all the time.

## 4.5 Performance Test Result of Mode-Matched and Mismatched MG3 MEMS Gyroscope with CMOS Readout Circuit

The next step after conducting the functionality test of the manufactured MEMS gyroscope sensor is to test its performance by gathering rate information by using a DAQ when the sensor is fixed at a stationary place.

Firstly, the MEMS gyroscope is configured to operate in the mismatched condition. In this operation, sense resonance frequency separated from the drive resonance frequency about 330Hz. After that, rate output is acquired and then analyzed by using Allan Variance analysis. The performance results can be seen at Figure 4.13. The results are similar with the calculated values, but bias instability is a bit higher than the calculated value due to some other secondary effects.

After testing the mismatched operation of the MEMS gyroscope sensor, the system is configure to operate in the mode-matched condition to test the performance of the mode-matched MEMS gyroscope. The drive displacements were identical with the mismatched mode providing identical scale factors. This test is also used to verify the operation of the mode-match loop by showing the performance increase nearly reaching down to the thermo-mechanical noise limit. The rate information of the mode-matched gyroscope is acquired with the same performance test setup and performance result is obtained as in Figure 4.14 with Allan Variance analysis after data acquisition. The ARW result of the mode-matched system is similar with calculated value and nearly reaches down to the Brownian noise of the MEMS MG3 gyroscope.

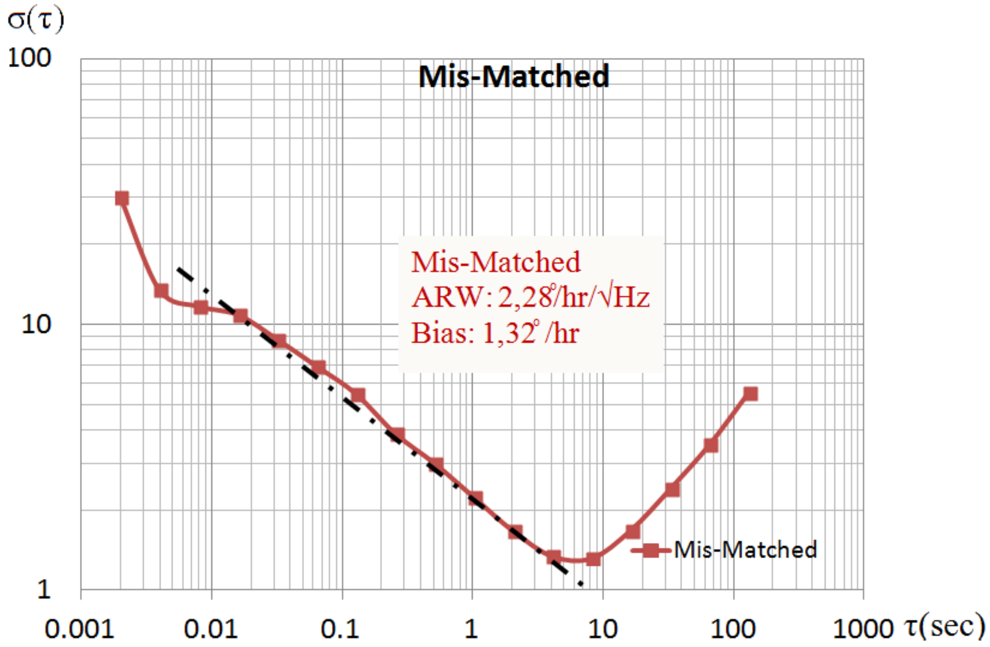

Figure 4.13: The Allan Variance results of the MEMS gyroscope for mismatched (Δf~330Hz) operation conditions. ARW: 2.28°/hr/√Hz, Bias instability: 1.32°/hr.

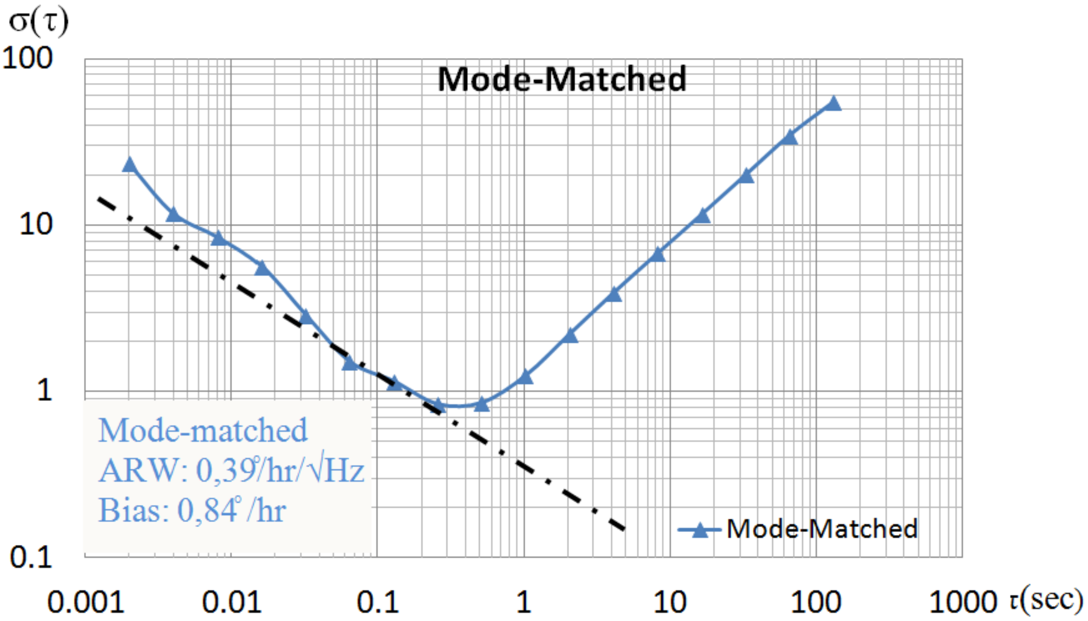

Figure 4.14: The Allan Variance results of the MEMS gyroscope for mode-matched operation conditions. ARW: 0.39°/hr/√Hz, Bias instability: 0.84°/hr.

Indeed, the performance results are showed that the bias instability and ARW performances are improved by factors of 1.5 and 6 as in Figure 4.15, respectively, with automatic mode-matching electronics, reaching down to 0.84°/hr and 0.0065°/√hr, respectively. The measured ARW performance of the mode-matched gyroscope is almost identical to the theoretically-calculated Brownian noise limit of the gyroscope (0.004°/√hr). The improvement in the ARW performance proves that the developed mode-matching system improves the signal to electronic noise ratio of the gyroscope by increasing the amplitude of the sense pick signal with the higher mechanical gain. These results show that the performance of the gyroscope is now truly limited by the Brownian noise of the mechanical sensor.

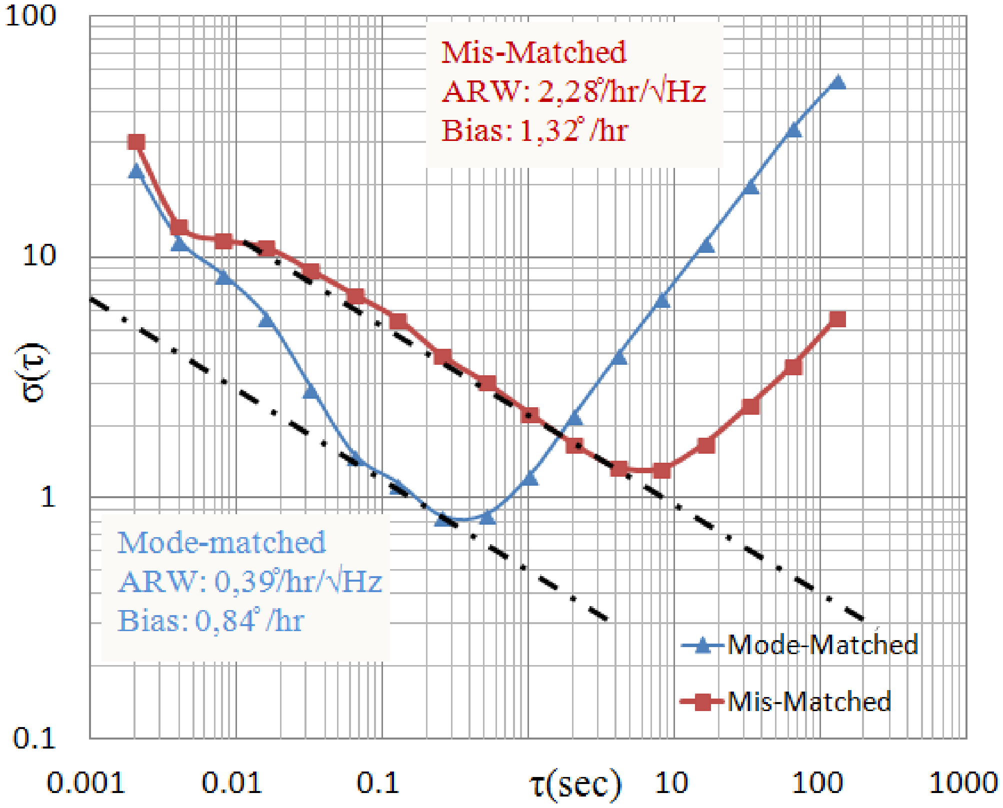

Figure 4.15: The Allan Variance results of the MEMS gyroscope for mode-matched and mismatched (Δf~330Hz) operation conditions. The automatic mode-matched system reaches to an ARW almost 6 times lower than the mismatched system (2.3 (°/hr)/√Hz versus 0.4 (°/hr)/√Hz).

## 4.6 Performance Test Result of Mismatched MG1 MEMS Gyroscope with CMOS Readout Circuit

After verifying the functionality of the MEMS MG1 gyroscope implemented with the CMOS readout circuit configured to operate in the mismatched condition. In this operation, sense resonance frequency separated from the drive resonance frequency about 330Hz. During the test the sensor is kept stationary and rate information is acquired with a DAQ, and then the test data is analyzed. The performance analysis is done by using Allan Variance analysis method. The results of the tested 3 different MEMS gyroscope sensors can be seen at Figure 4.16, Figure 4.17, and Figure 4.18. Similar results are obtained from three different MEMS gyroscopes which are subjected to the same testing procedure.

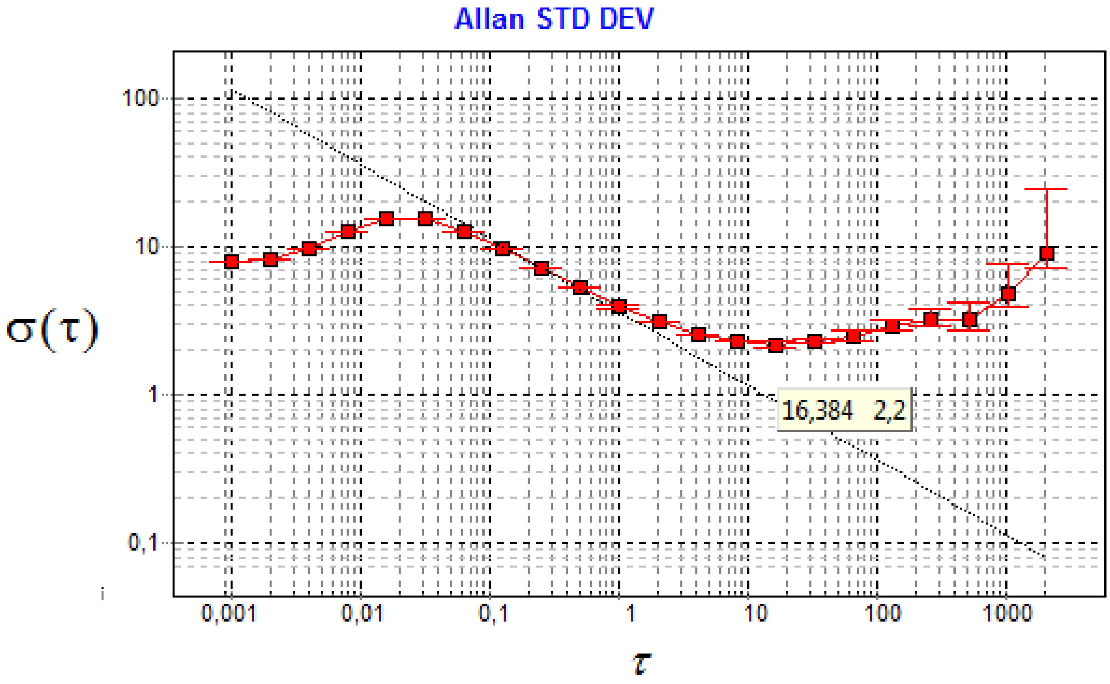

Figure 4.16: The Allan Variance result of the gyroscope implemented with MG1 gyroscope and the CMOS readout IC. The bias stability only increases to 5.0°/hr at 1000s. Bias stability=2.2°/hr, ARW=3.6°/hr/√Hz.

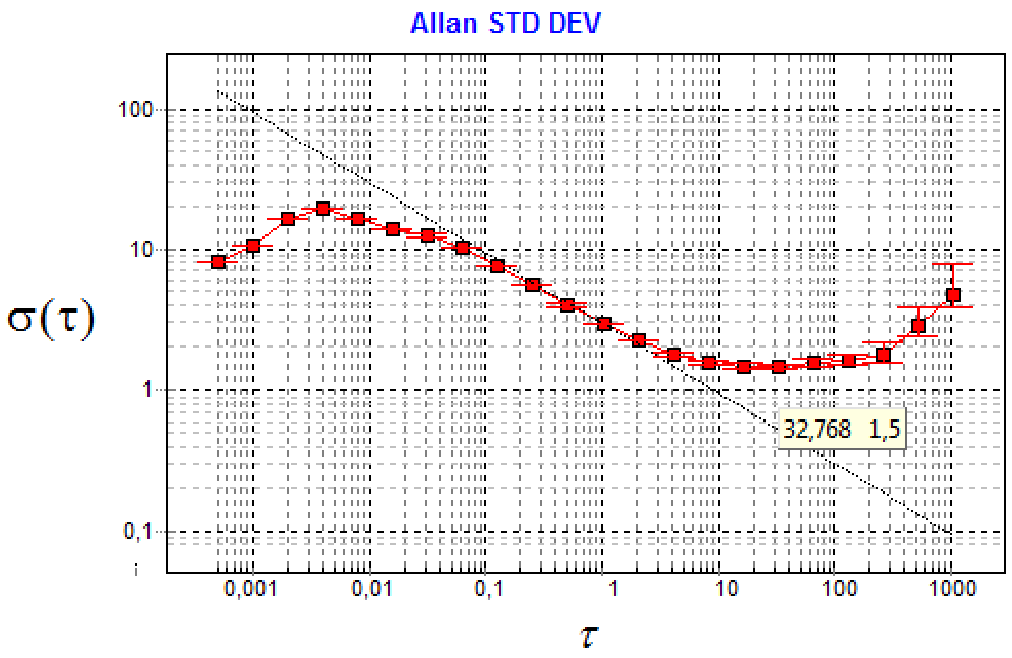

Figure 4.17: The Allan Variance result of the gyroscope implemented with MG1 gyroscope and the CMOS readout IC. The bias stability only increases to 4.8°/hr at 1000s. Bias stability=1.5°/hr, ARW=3.0°/hr/√Hz.

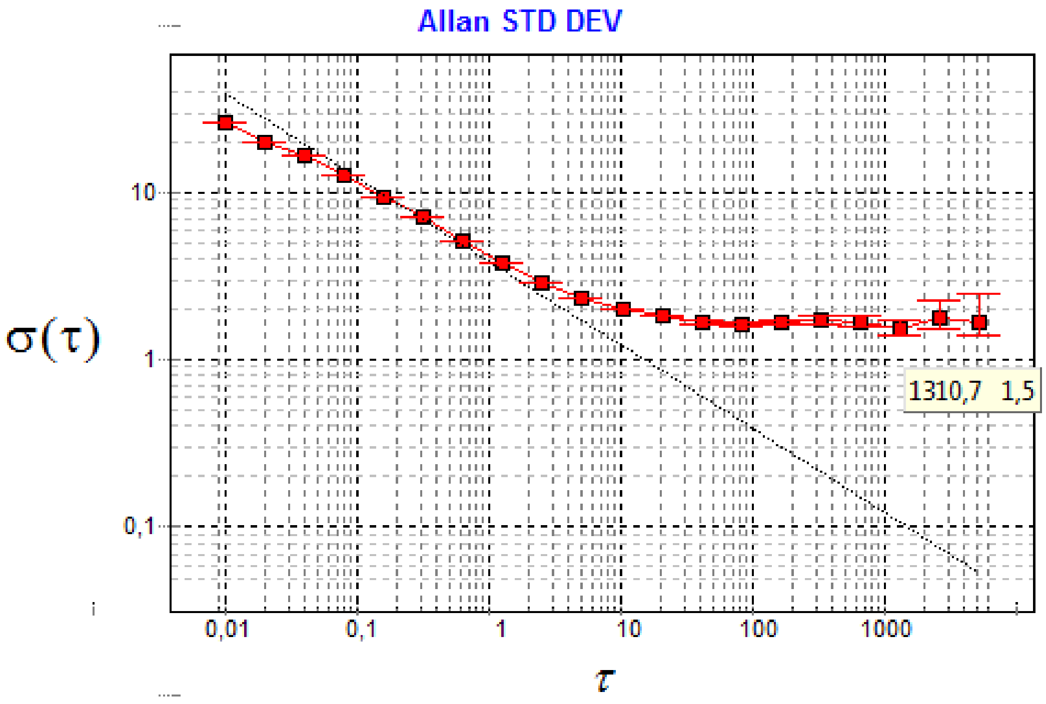

Figure 4.18: The Allen Variance result of the gyroscope implemented with MG1 gyroscope and the CMOS readout IC. The bias stability only increases to 1.5°/hr at 1000s. Bias stability=1.5°/hr, ARW=3.8°/hr/√Hz.

Linearity and range are also significant performance parameters. The linearity and the range is related with the op-amps and MEMS structure's linearity. Figure 4.19 shows the linearity test plot for the gyroscope implemented with MG1 and the CMOS readout circuit for 8µm drive displacement. During the linearity test, rate is applied at rates -300°/s, -250°/s, -200°/s, -150°/s, -100°/s, -50°/s, -40°/s, -30°/s, -20°/s, -10°/s, 0°/s, 10°/s, 20°/s, 30°/s, 40°/s, 50°/s, 100°/s, 150°/s, 200°/s, 250°/s, 300°/s. The actual linearity is defined as the maximum deviation from the fitted line divided by the whole range. By using this linearity definition, 3 tests are conducted on the MEMs gyroscope and then linearity, and scale factor repeatability results are obtained as in Table 4.2. These linearity and the repeatability results are obtained from the raw data, these results can be improved with calibration methods at the inertial measurement unit implementation level.

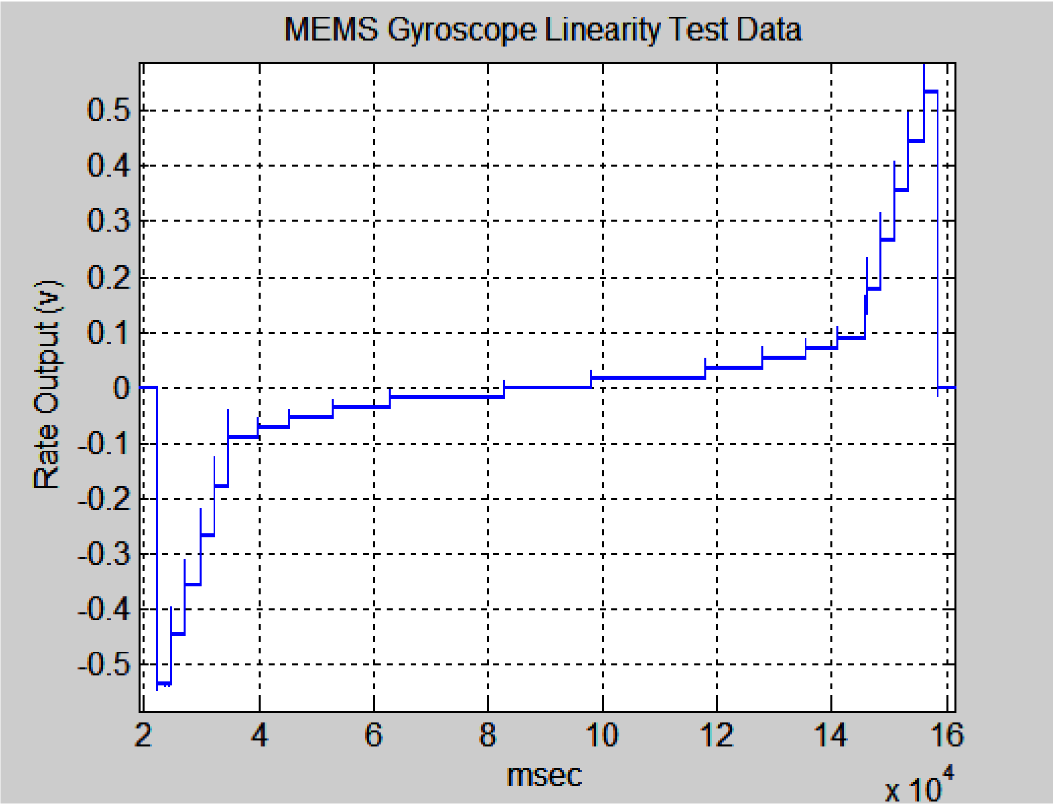

Figure 4.19: The linearity test data of the MEMS gyroscope by applying the mentioned rates step by step with different time intervals to obtain same SNR for all rate levels.

Table 4.2: The linearity and repeatability test results obtained with 3 tests.

| | TEST 1 | TEST 2 | TEST 3 | Repeatability (ppm) |
|---|---|---|---|---|
| Scale Factor (mV/deg/s) | 1.66005 | 1.66079 | 1.66102 | 305 |
| Linearity (ppm) | 470 | 452 | 456 | 12 |

Extra to these performance tests, for a MEMS gyroscope, bias repeatability is so important. The bias repeatability tests are done by acquiring the rate data when the MEMS gyroscope stationary and stabilized its own temperature by waiting 15 minutes. After that, the means of the 3 tests are used to determine the bias repeatability of the sensor as in Table 4.3. The test results are very good compared to state of the art MEMS gyroscope sensors at tactical grade level. By using this gyroscope with this repeatability, almost navigation level performances can be obtained.

Table 4.3: The bias repeatability test results obtained with 3 tests.

| | TEST 1 | TEST 2 | TEST 3 | Repeatability |
|---|---|---|---|---|
| Scale Factor (mV/deg/s) | 1.66005 | 1.66079 | 1.66102 | 305 ppm |
| Bias (mV) | 0.05294 | 0.05318 | 0.05101 | 2.6 deg/hr |

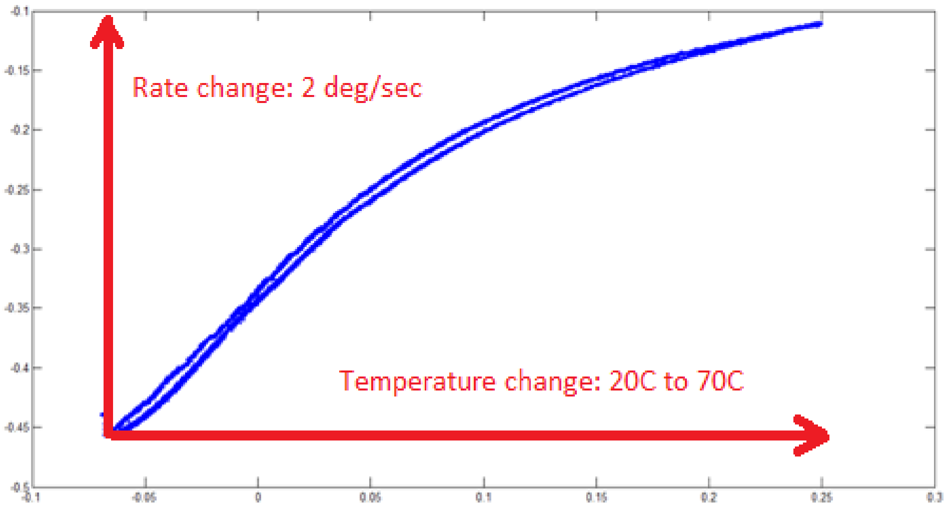

Figure 4.20: The temperature test (rate vs. temperature sensor out) result of the gyroscope readout circuit with MG1 gyroscope. Temperature is swept from 20°C to 70°C and 70°C to 20°C.

As a final performance test, the MEMS gyroscope sensor is heated from 20°C to 70°C to see the effects of temperature on the bias of the sensor as in Figure 4.20. The Figure 4.20 clearly shows that, temperature highly affects the performance of the sensor's bias. The calibration methods can also improve the sensor's bias performance further at the inertial measurement unit level. This test also shows that system does not have hysteresis.

## 4.7 Summary

This chapter presents the performance results of tuning fork MEMS gyroscopes with mode-matched and mismatched operation. The experimental verification of the mode-matching controller loop is done with an externally created frequency mismatch. The test results are obtained from a fully closed loop systems. It is shown that closed loop drive amplitude control, force feedback, quadrature cancellation, and mode-match system operate as expected.

The complete CMOS readout electronics having all four control loops and preamplifiers are properly tested and it is seen that the performance of the CMOS as good as compared to previously studied readout electronics implemented with discrete components and CMOS. The long term stability of this CMOS readout is also better than the previous studies. The integration time of more than 5000sec is obtained with a 1.5°/hr, that performance highly competitive with commercial products in the tactical grade applications.

Extra to bias and ARW performance results, bias repeatability and scale factor repeatability tests are conducted and obtained very good repeatability results of 2.5°/hr and 300ppm respectively without calibration. It is concluded that, the CMOS readout circuit proves its high performance with mode-matched and mismatched operation of tuning fork MEMS gyroscopes.

# CHAPTER 5

# CONCLUSION AND FUTURE WORK

This work presents a comprehensive study on the robust controller design and its implementation in a CMOS technology. In this study, issues related to the mode-matching of a fully decoupled micro-machined vibratory gyroscope are also studied. The drive mode, sense mode, quadrature cancellation, and mode-matching closed-loop systems and their robust controller design procedures are discussed in details, and they are optimized for robustness to the system variations and bandwidth. Accomplishments and results of this research can be listed as follows:

1. The detailed system level analysis has been carried out for the drive mode, sense mode, and quadrature cancellation system. Firstly, the mathematical models of the tuning fork gyroscope is implemented in SPICE environment including almost all linear and nonlinear transfer functions to simulate the MEMS with readout electronics simultaneously. The created model has provided so many benefits during the design of closed loop controllers because model is almost same with real system.

2. After modeling the tuning fork MEMS gyroscope, drive mode closed loop controller is designed. In this design, drive mode transfer function is modeled as an integrating system due to high Q and very low bandwidth compared to closed loop bandwidth of the drive loop. This modeling has provided Q independent controller design procedure. The controller can control the system with Q-factor more than 10,000. The drive mode controller is designed by using pole placement method without cancelling any zero in the transfer functions. At the previous studies focused on pole-zero cancellation method but this method has some drawbacks due lack of controllability condition. Because a necessary and sufficient condition for controllability is that no single pole of the system is cancelled by a zero in all of the elements of the transfer-function. If such cancellation occurs, the system cannot be

controlled in the direction of the cancelled mode. This means that, if any disturbance occurs in the drive displacement, disturbance damped only by the damping of the drive mode. The designed controller cannot react any disturbance and only perform in the set-point tracking side.

3. The sense mode controller design is done for the mismatched and mode-matched conditions. Because transfer function of the sense mode changes from second order high-Q factor system to first order very low bandwidth system. For the mismatch condition, the controller is designed to control second order system. The first optimization is done to decrease the sense and drive resonance frequency difference for a 100Hz bandwidth system while considering the stability issue. When the difference decreased, noise and bias performances theoretically increase, but at some level system became unstable. Extra to this optimization system is designed to be robust to the variations of the transfer function of the sense mode. Because sense mode gain change with temperature and sensor to sensor. Sense mode controller is designed to have 100Hz bandwidth with only 330Hz frequency difference. After that, a different controller is designed for the mode-matched MEMS gyroscope. The transfer function of the sense mode at the mode-matched condition is highly similar with the drive mode with lower Q factor. Because of that, the controller is designed with the design procedure with drive controller design procedure. In this procedure, Q factor should be higher to model the transfer function as an integrating system. However, the Q factor of the sense mode is lower than the Q factor of the drive mode, but this is not a problem, because closed loop bandwidth is also higher and again open loop bandwidth is very low compared to closed loop bandwidth. Finally, the closed loop sense controller provided 100Hz bandwidth having robustness to the Q factor variations.

4. The closed loop quadrature controller design is done for mismatched and mode- matched MEMS gyroscope. The designs for both conditions are engineered by using the same procedure for the closed sense mode controller. Because the transfer functions are same, the only difference is their gains. So, the controllers are designed, but the controller for mode-match condition is designed having lower bandwidth than the sense mode controller in order to implement mode-match controller effectively.

5. A closed-loop controller system developed for in-run automatic matching of the drive and sense mode resonance frequencies of a MEMS gyroscope with a high quality factor (Q). This is achieved by injecting a perturbation signal to the quadrature cancellation loop, while keeping it decoupled from the angular rate control loop. The new controller is implemented in a CMOS ASIC together with the other sensor control loops, and it is verified to maintain matched-mode state under changing environmental conditions. The proposed system is experimentally verified to reduce the angle random walk (ARW) of the gyroscope by a factor of 6, reaching down to the thermo-mechanical noise limit of 0.4 (°/hr)/Hz$^{1/2}$. The improvement in the ARW performance proves that the developed mode-matching system improves the signal to electronic noise ratio of the gyroscope by increasing the amplitude of the sense pick signal with the higher mechanical gain. These results show that the performance of the gyroscope is now truly limited by the Brownian noise of the mechanical sensor.

6. The CMOS implementations of the proposed robust controller designs and mode matching system of a fully decoupled micro-machined vibratory gyroscope electronics have been carried out. These are the first MEMS gyroscope sensor system implemented with the functional ASIC chip and vacuum packaged MEMS gyroscope in a 22mm by 22mm metal package developed at METU. This work provides an almost product level high performance MEMS gyroscope has capability of mass production. The performance results are applicable for the tactical grade applications. Moreover, performance results of the mode-matched MEMS gyroscope are also promising for the navigation grade application.

Major achievement of this thesis is the development of robust and effective design procedures for the analog controllers of the MEMS gyroscopes. The analog controllers and other all electronics are implemented in a CMOS technology. Functionality of these chips is verified. The chip and the MEMS gyroscope are implemented in one small metal package, and the performance tests for the mode-matched and mismatched cases are conducted. For the mode-matched case, sub-degree per-hour gyroscope performance is achieved without sacrificing linearity and other performance metrics by using the proposed mode-matching system. To achieve further improvement, some of the future topics are listed below:

1. Today's trends are the digital systems due to their configurability and promising higher performance. Moreover, the digital implementation can be implemented without using any external passive components. This will make the mass manufacturing highly applicable. It requires a careful circuit and system level designs, but that is required for a product level implementation.

2. A new gyroscope can be designed to increase the long term drift problem of the mode-matched gyroscope. Because, the used gyroscope is a single mass tuning fork gyroscope and has so much anchor loss leading Q factor change abruptly.

3. A new trend in the gyroscope development is the development of rate integrating MEMS gyroscope. As a future development, these systems can be improved with some different methods to achieve navigation grade levels due to their higher long term drift performances.

4. The control loops can be implemented by using sigma delta converter architectures. However, the implementation can be done with a microcontroller by using the converted modulated low bandwidth signal. This design relaxes the ADC requirements, and provides configurability in the controller parameters.

# REFERENCES

[1] N. Yazdi, "Micromachined inertial sensors," *Proceedings of the IEEE,* vol. 86, no. 8, pp. 1640-1659, 1998.

[2] I. Prikhodko, "Sub-degree-per-hour silicon MEMS rate sensor with 1 million Q-factor," *Proceedings of TRANSDUCERS,* pp. 2809-2812, 2011.

[3] T. Remtema, "Active frequency tuning for micro resonators by localized thermal stressing effects," *Sensors and Actuators A: Physical,* pp. 326-332, 2001.

[4] B. Gallacher, J. Hedley and e. al., "Electrostatic correction of structural imperfections present in a microring gyroscope," *Journal of Microelectromechanical Systems,* vol. 14, no. 2, pp. 221-234, 2005.

[5] M. A. Abdelmoneum and M. M. Demirci, "Location-dependent frequency tuning of vibrating micromechanical resonators via laser trimming," *Proceedings of IEEE Frequency Control Symposium and Exposition,* pp. 272-279, 2004.

[6] A. Sharma, "1° hr bias drift electronically matched tuning fork microgyroscope," *Proceedings of IEEE MEMS 2008,* pp. 6-9, 2008.

[7] R. Antonello, "Automatic Mode Matching in MEMS Vibrating Gyroscopes Using Extremum-Seeking Control," *IEEE Transactions on Industrial Electronics,* pp. 3880-3891, 2009.

[8] C. D. Ezekwe and B. E. Boser, "A Mode-Matching Closed-Loop Vibratory Gyroscope Readout Interface With a 0.004 √Hz Noise Floor Over a 50 Hz Band," *IEEE Journal of Solid-State Circuits,* vol. 43, no. 12, pp. 3039-3048,

2008.

[9] H. Wu, "System Architecture for Mode- Matching a MEMS Gyroscope," *M. of Eng. Thesis, MIT,* 2009.

[10] T. Hägglund and J. Åström, "Revisiting The Ziegler-Nichols Tuning Rules For Pi Control," *Asian Journal of Control,* vol. 4, pp. 364-380, 2002.

[11] R. I. Shakoor and S. A. Bazaz, "Electrothermally Actuated Resonant Rate Gyroscope Fabricated Using the MetalMUMPs," *Journal of Microelectronics,* vol. 42, no. 4, pp. 585-593, 2011.

[12] K. Foust and C. Puig, "Standardized Sensor Performance Parameter Definitions," Intel Corp., 2013.

[13] "IEEE Standard for Inertial Sensors Terminology," *IEEE Std 528-2001,* 2001.

[14] P. Greiff and B. Boxenhorn, "Silicon Monolithic Micromechanical Gyroscope," in *6th International Conference of Solid-State Sensors and Actuators*, San Francisco, CA, 1991.

[15] D. Xia, C. Yu and L. Kong, "The Development of Micromachined Gyroscope Structure and Circuitry Technology," *Sensors,* pp. 1394-1473, 2014.

[16] D. Lapadatu and B. Blixhavn, "SAR500 - A High-Precision High-Stability Butterfly Gyroscope with North Seeking Capability," in *Position Location and Navigation Symposium (PLANS 2010)*, IndianWells, CA, 2010.

[17] B. R. Johnson and E. Cabuz, "Development of a MEMS Gyroscope for Northfinding Applications," in *Position Location and Navigation Symposium (PLANS 2010)*, 2010.

[18] B. Chaumet and B. Leverrier, "A New Silicon Tuning Fork Gyroscope for Aerospace Applications," in *Symposium Gyro Technology*, Karlsruhe, Germany, 2009.

[19] S. E. Alper, "MEMS Gyroscopes for Tactical-Grade Inertial Measurement

Applications," in *Dissertation for the Degree of Doctor of Philosophy*, Middle East Technical University, 2005.

[20] E. Tatar, "Quadrature Error Compensation and Its Effects on the Performance of Fully Decoupled MEMS Gyroscope," in *M.S. Thesis*, Middle East Techical University, 2010.

[21] M. M. Torunbalci, S. E. Alper and T. Akin, "Wafer Level Hermetic Sealing of MEMS Devices with Vertical Feedthroughs using Anodic Bonding," *Sensors and Actuators A,* no. 224, pp. 169-176, 2015.

[22] M. M. Torunbalci, "Development of New, Simple, and Robust Wafer Level Hermetic Packaging Methods for MEMS Sensors," in *Ph.D. thesis*, METU, 2015.

[23] H. D. Gavcar, "Compensation Methods for Quasi-Static Acceleration Sensitivity of MEMS Gyroscopes," in *M.S. Thesis*, Middle East Technical University, 2014.

[24] B. Eminoglu, "Control Electronics for MEMS Gyroscope and Its Implementation in a CMOS Technology," in *M.S. Thesis*, METU, 2011.

[25] wikipedia, 11 2014. [Online]. Available: https://en.wikipedia.org/wiki/Fictitious_force.

[26] F. Yesil, "An Automatic Mode Matching System for a High Q-Factor MEMS Gyroscope Using a Decoupled Perturbation Signal," in *IEEE Transducers*, Anchorage, 2015.

[27] A. Bhat, "Stabilize Your Transimpedance Amplifier," Maxim Integrated, 5 2015. [Online]. Available: http://www.maximintegrated.com/en/app-notes/index.mvp/id/5129.

[28] D. Rowell, "Controllability, Observability and the Transfer Function," MIT, Massachsetts, 2004.